2017

# Harnessing Spatial Intensity Fluctuations for Optical Imaging and Sensing

Milad Akhlaghi Bouzan
*University of Central Florida*

# HARNESSING SPATIAL INTENSITY FLUCTUATIONS FOR OPTICAL IMAGING AND SENSING

by

MILAD AKHLAGHI BOUZAN

B. Sc. University of Tehran, 2011
M.Sc. University of Tehran, 2013
M.Sc. University of Central Florida, 2015

A dissertation submitted in partial fulfillment of the requirements

for the degree of Doctor of Philosophy

in the College of Optics and Photonics

at the University of Central Florida

Orlando, Florida

Fall Term

2017

Major Professor: Aristide Dogariu

# ABSTRACT

Properties of light such as amplitude and phase, temporal and spatial coherence, polarization, etc. are abundantly used for sensing and imaging. Regardless of the passive or active nature of the sensing method, optical intensity fluctuations are always present! While these fluctuations are usually regarded as noise, there are situations where one can harness the intensity fluctuations to enhance certain attributes of the sensing procedure. In this thesis, we developed different sensing methodologies that use statistical properties of optical fluctuations for gauging specific information. We examine this concept in the context of three different aspects of computational optical imaging and sensing. First, we study imposing specific statistical properties to the probing field to image or characterize certain properties of an object through a statistical analysis of the spatially integrated scattered intensity. This offers unique capabilities for imaging and sensing techniques operating in highly perturbed environments and low-light conditions. Next, we examine optical sensing in the presence of strong perturbations that preclude any controllable field modification. We demonstrate that inherent properties of diffused coherent fields and fluctuations of integrated intensity can be used to track objects hidden behind obscurants. Finally, we address situations where, due to coherent noise, image accuracy is severely degraded by intensity fluctuations. By taking advantage of the spatial coherence properties of optical fields, we show that this limitation can be effectively mitigated and that a significant improvement in the signal-to-noise ratio can be achieved even in one single-shot measurement. The findings included in this dissertation illustrate different circumstances where optical fluctuations can affect the efficacy of computational optical imaging and sensing. A broad range of applications, including biomedical imaging and remote sensing, could benefit from the new approaches to suppress, enhance, and exploit optical fluctuations, which are described in this dissertation.

# ACKNOWLEDGMENTS

It is my greatest pleasure to recognize those who have supported me. I am grateful to my PhD advisor, Dr. Aristide Dogariu, who made this entire endeavor possible with his inspiring dedication and intuition, and making this a great learning opportunity. I specially thank him for guiding and advising me throughout the years.

I would like to thank my committee for their constructive remarks and for sharing their expertise and knowledge in the field of optical and computational science. I am highly grateful to Dr. Lucia Cilenti for her constant support, kindness, and hours of enjoyable discussion we had. I am grateful to Dr. Antonis S. Zervos and his Lab members for providing biological samples for my research studies.

I am thankful to my wonderful and friendly colleagues at CREOL specially Photonics Diagnostic of Random Media group members. I would also like to thank my professors specially Dr. Pieter G. Kik for the time and energy that he spent on his course. I am grateful to CREOL staffs for constantly being available with their generous supports and advices.

I was tremendously fortunate to have had many wonderful teachers and professors through the years. There are too many to list here, but I would like to specially thank my middle school calculus teacher Mr. Aadeli, my undergraduate supervisor Dr. Jalil Rashed-Mohassel, my undergraduate thesis advisor Dr. Mojtaba Dehmollaian and my master studies thesis advisor Dr. Mohmoud Shahabadi who are the ones who always stand out in my mind.

Finally, I would like to thank my wonderful family and friends for always being supportive and encouraging.

# TABLE OF CONTENTS

# LIST OF FIGURES

# CHAPTER ONE: INTRODUCTION

Light is considered to be one of the most popular probes for investigating nature because of its non-invasiveness character and the availability of the natural light detectors such the human eye. Characterization techniques using light are found in a wide range of applications in different domains and, in general, they can be regarded as a system comprising different elements, each with its own characteristic and physical properties. A generic optical system has five main components: the source of light, the process of light-matter interactions, the optical relay systems, the detection of light, and, finally, the processing unit.

Ideal elements are noise free, a situation that never encountered in practice where a measurement process comes with an uncertainty to which each element of the optical system has its own contribution. For instance, the practical light sources, both the coherent and the incoherent ones, have inherent random fluctuations. Moreover, the outcome of light matter interaction is usually statistical in nature, which adds to the ambiguity of the entire process [1, 2]. Furthermore, realistic optical relay systems, or optical information transformation processes, are not perfect and their limited size in conjunction with diffraction, and non-ideal light scattering properties can add even more uncertainty. For instance, the propagation of information through atmosphere can be severely affected by unwanted fluctuations [3]. Besides that, the detection of light is limited by noise, e.g. shot noise [4], due to the inherent fluctuations . Lastly, processing the detected information, if it is required, can be another source of ambiguity, especially when statistical processing is necessary [5].

Since in many cases, depending on the experiment and the required outcome, the sources of uncertainty can be neglected, optical systems have been treated deterministically for a long time. However, when optical fluctuations follow specific statistical laws, they could be considered as

probes for investigating different properties of light-matter interaction. In the last century, the use of the optical fluctuations has been demonstrated in many different circumstances, including optical imaging and sensing scenarios [6-10].

As already mentioned, depending on the situation, optical field fluctuations can be considered as either noise or signal. In the latter case, by taking advantage of the statistical properties of the fluctuations, certain attributes of the optical system may be enhanced, as we will see in the next chapters. Moreover, in some cases, statistical properties can be manipulated to separate the signal from noise efficiently.

It is worth mentioning that, in practical cases, if the optical signals and the noise are separable with respect to a specific physical property, e.g. space, frequency, state of the polarization, etc., one can take advantage of it to eliminate the noise. Unfortunately, this separation is not always possible. However, in most practical cases, unwanted noisy fluctuations are statistically independent from the signal. Consequently, a statistical analysis of the outcome of the measurement could be a convenient approach to separate signals from noise

**Imposing optical fluctuations:** Having an unknown target of interest in an optical characterization scenario, one can impose specific statistical properties to the optical probe by introducing additional randomness in order to enhance a certain attribute of the procedure. For instance, a speckle field could be exploited for illumination while imaging dynamic scenes [11]. In chapter two, we will show that, using a stochastically structured field, one can compress the active correlation imaging procedure in highly perturbed conditions. Nevertheless, using a stochastic probe with certain imposed statistics is not limited only to the optical imaging. For example, using the nonlinear phenomenon known as stochastic resonance, one can enhance the signal to noise ratio in an optical system, by actually adding more noise [8]. In chapter two, we

will discuss another example where imposing randomness to an optical system makes it possible to operate in very low signal to noise ratio conditions. We will show that by imposing the optical fluctuations with controlled statistical properties, one can separate the signal from the noise efficiently, through enhancing meaningful fluctuations. Besides, we will show that imposing additional randomness to the sensing procedure allows compressing the procedure time, and, as a result, reduces the required exposure energy. We will show that using compressive sensing strategies one can reduce required cumulative probe field energy density for stochastic characterization of the objects, regardless of the sparsity level of the target.

**Exploiting optical fluctuations:** Enhancing fluctuations is a powerful approach for optical imaging and sensing. However, imposing fluctuations by controlling the structure and the statistical properties of an optical probe is not always possible. For instance, the presence of a strong source of perturbation between the probe field source and the target of interest impedes any control on the spatial and the angular distribution of the light without prior knowledge and feedback [12]. Consequently, imposing fluctuations with controlled statistical properties may not be possible. However, as we will show in chapter three, one can exploit the intrinsic properties of the fluctuations, generated through available source of perturbation in the process, to acquire information about the target of the interest. More specifically, we will see that statistical dynamics of the noisy-like temporally fluctuating optical field intensity can be used efficiently for sensing the dynamics of an obscured target.

**Reducing optical fluctuations:** Even though the optical fluctuations can play a role as a useful optical probe, in some cases they can be quite troublesome. When the unwanted fluctuations are much stronger than the signal, but one can still have access to the light source, different approaches can be applied to overcome the noise [13-15]. On the other hand, having access only to the

detection side makes the task way more difficult. This problem becomes even more complicated when the available noise not only masks the information but also changes its content through coherent interaction, i.e. interference. This problem usually occurs when one has to use a coherent beam of light for imaging or sensing purposes [16, 17]. In chapter four we will show that exploiting the inherent properties of the desired optical field and the optical noise, one can computationally reduce the unwanted spatial fluctuations through a statistical analysis of the corrupted field.

Light can be used for characterizing objects in various phenomena and many different approaches are developed to achieve different tasks and, in all cases, light intensity fluctuates. The present study covers different practical aspects of dealing with fluctuating optical signals in the context of computational optical imaging and sensing, where depending on the specific task, fluctuations can be imposed, exploited, and reduced, in conjunction with an appropriate statistical analysis of the measured optical signal. In the following chapters, we demonstrate different approaches. We will then conclude and propose future developments.

# CHAPTER TWO: IMPOSING RANDOMNESS IN LIGHT-MATTER INTERACTION FOR OPTICAL IMAGING AND SENSING

## Fluctuations Based Optical Measurement

Fluctuations of the optical field intensity constitute a powerful probe of light-matter interactions in different circumstances. For instance, speckle imaging has shown remarkable performance in imaging dynamic scenes [11, 18] using temporal fluctuations of the speckle field. Super-resolution optical fluctuation imaging (SOFI) [19, 20] is another example of exploiting fluctuations in the light field for optical imaging, in which statistical independence of the optical fluctuation sources provide possibility to enhance the spatial resolution.

Fluctuations based methods are not limited only to the optical imaging. Various sensing tasks are also achieved through exploiting light fluctuations. As a prominent example, one can mention fluorescence correlation spectroscopy (FCS) in which temporal fluctuations of the optical signal provide information about the dynamic of the targeted objects after analyzing the rate and the amplitude of these intensity fluctuations [7, 21-23]. Of course, fluctuations based sensing is not limited to FCS. An entire range of fluctuations based methods are based on the well-known non-linear phenomenon of stochastic resonance. This is a powerful technique with applications in different domains such as thermal fluctuations in the earth's climate change [24], enhancing human brain perception [25], modulating ring laser [26], improving optical signal to noise ratio [27], etc.

In this chapter, we will discuss three problems in the field of optical imaging and sensing. We will show that by imposing random fluctuations by exploiting a stochastic optical probe for information acquisition, certain attributes of the imaging and sensing procedure could be enhanced. In the following, we will first discuss Correlation Imaging using random illumination, method that provides the possibility to image an object with high compression ratio in low signal-to-noise ratio regime [28-30]. Then we will introduce Stochastic Optical Sensing, which provides means for

measuring statistical parameters of a target by enhancing fluctuations of the optical field intensity [31-34]. Finally, we exploit compressive sensing and introduce compressive Stochastic Optical Sensing that offers capabilities for operating in time-lapse characterization under low light intensity and cumulative illumination energy density, regardless of the sparsity of the target of interest [35-37].

## Correlation Imaging Using Random Illumination

Over the last decade, technological advances have opened new avenues for computational light microscopy. Some attempts rely on sequentially illuminating a sample with a number of periodic patterns having different spatial frequencies [38-40]. Others use different types of random illumination [41, 42]. In all these attempts, the resulting spatially-resolved intensities, $I(\boldsymbol{x})$ are measured for each state of illumination and then the image is reconstructed by subsequent computations [43-46]. Alternative approaches are based on integrating the entire intensity output and then compute the final image [47-51].

### Correlation Imaging

Correlation imaging (CI) relies on replicas of the illumination field to act as reference used in computations. This reference can be either a physical reference field [41] or an electronic synthetic copy of the illumination [47]. The object field is usually created using a spatial light modulator and the result of its interaction with the target is integrated and detected [50, 52-54]. Let us consider the practically important case of reflection mode imaging where light with the spatial profile of intensity $I(\boldsymbol{\rho}; t)$ impinges at time $t$ on a target with linear reflectivity $T(\boldsymbol{x})$. These are most common circumstances for biological microscopy. In CI, the reflected light intensity is integrated and collected by a detector with area $\sigma$, which provides the signal

$$i(t_m) = \left\langle \int_\sigma I(\boldsymbol{\rho}; t_m) T(\boldsymbol{\rho}) d\boldsymbol{\rho} + \int_\sigma N(\boldsymbol{\rho}; t_m) d\boldsymbol{\rho} \right\rangle_\tau \quad (1)$$

The recorded intensity in Eq. (1) corresponds to the $m^{\text{th}}$ illumination frame and it is integrated over the total duration $\tau$ of that specific frame. This intensity is detected with a signal-to-noise-ratio SNR= $\left\langle \int_\sigma I(\boldsymbol{\rho}; t) T(\boldsymbol{\rho}) d\boldsymbol{\rho} \right\rangle_{\boldsymbol{\tau}} / \left\langle \int N(\boldsymbol{\rho}; t) d\boldsymbol{\rho} \right\rangle_\tau$. The spatial distribution of the reflectivity, i.e. the "image" $\mathcal{T}(\boldsymbol{x})$, is then reconstructed by cross correlating the ensemble of the recorded intensities with the corresponding known distributions of illumination

$$\mathcal{T}(\boldsymbol{\rho}; M) = M^{-1} \sum_{i=1}^{M} (i(t_i) - \langle i(t) \rangle_M) I(\boldsymbol{x}; t_i), \quad (2)$$

where $M$ is the total number of illumination frames and $\langle \dots \rangle_M$ denotes the average over the entire process [54]. This approach does not require any prior knowledge; however, having *a priori* information available, one can exploit it in a nonlinear image reconstruction procedure, as it is discussed in Appendix A. The error in recovering the image using only $m \leq M$ illumination patterns is defined as $e_m(\boldsymbol{x}) = T(\boldsymbol{\rho}) - \mathcal{T}(\boldsymbol{\rho}; m)$. The incremental change of this error, $e_{m+1}(\boldsymbol{\rho}) - e_m(\boldsymbol{\rho})$ can be estimated to be

$$\Delta e_{m,tot} = -\iint T(\boldsymbol{\rho}') \psi(\boldsymbol{\rho}'; t_m) \psi(\boldsymbol{\rho}; t_m) d\boldsymbol{\rho}' d\boldsymbol{\rho} + \mathcal{N}(t_m) \quad (3)$$

where $\psi(\boldsymbol{\rho}; t_m) = I(\boldsymbol{\rho}; t_m) - \langle I(\boldsymbol{\rho}; t_m) \rangle_M$ describes the relative fluctuations in the illumination patterns, and $\mathcal{N}(t_m) = \iint I(\boldsymbol{\rho}; t_m) \langle N(\boldsymbol{\rho}'; t_m) \rangle_\tau d\boldsymbol{\rho} d\boldsymbol{\rho}'$ accounts for the additive noise. An analysis of image formation in the general context of correlation imaging can be found in [47, 55]. It is important to emphasize that the image reconstruction is subject only to fluctuations of the recorded intensity and not to its absolute value. Thus, the intensity fluctuations and, therefore, the quality of image reconstruction is affected by the spatial distribution of illumination as can be inferred from Eq. (3).

## Probe Field Spatial Structure

Previous works investigated different types of illumination for both active (illuminating the target with spatially modulated light) [42] and passive procedures (sampling the return from the target before detection) [56, 57] illumination system. In general, the active imaging procedures can be categorized as using random or patterned illumination. In the first case, the illumination is spatially incoherent, i.e. $\psi_r(\boldsymbol{\rho}; t_m) * \psi_r(-\boldsymbol{\rho}; t_m) = \sigma_S^2 \delta(\boldsymbol{\rho})$ for all the random realizations in different frames. A patterned illumination, on the other hand, is characterized by an autocorrelation function $\psi_p(\boldsymbol{\rho}; t_m) * \psi_p(-\boldsymbol{\rho}; t_m) = C_m(\boldsymbol{\rho}; t_m)$ which may vary from frame to frame. Of course, random illumination is simple and completely unbiased to any specific target but one cannot control the information provided at each frame. However, when illumination follows patterns that correspond to an orthogonal basis, the cross-talk between different frames can be minimized [51]. In the following, we will compare these two types of illumination.

Changing the nature of illumination affects the image reconstruction, but as it can be seen form Eq. (2), the image formation also depends on the total number of available frames. A larger $M$ results in a more precise and less noisy reconstruction. Therefore, for given field of view, one of the main efficiency criteria is the number of independent measurements $m$ (frames) necessary to provide a desired number $N$ of pixels in the computed image. This constitutes the compression ratio $N/m$ of the CI procedure. Very high compression can be obtained using proper illumination.

As seen in Eq. (1), variations in the illumination profile $I(\boldsymbol{\rho}; t)$ translate into fluctuations of the recorded intensity, $i(t) - \langle i(t) \rangle_M$, which affect the image reconstruction and the associated errors according to Eqs. (2) and (3). In Here, we will consider only the case of binomial distributions of intensities, which are either randomly distributed or structured in specific patterns. As apparent from Eq. (2), this type of illumination determines the highest level of fluctuations and therefore

can provide the highest compression ratios. The binary patterned illumination will be based on Hadamard patterns which constitute the complete orthogonal set commonly used in target independent CI [51, 58], because of its superior performance over dictionary based approaches [59].

## Demonstrations

To compare these two types of illumination, the quality of reconstruction is quantified with Pearson's correlation coefficient

$$\rho = \frac{\int \left(\mathcal{T}(\boldsymbol{\rho};M)-\int \mathcal{T}(\boldsymbol{\rho'};M)d\boldsymbol{\rho'}\right)\left(T(\boldsymbol{\rho})-\int T(\boldsymbol{\rho''})\mathrm{d}\boldsymbol{\rho''}\right)d\boldsymbol{\rho}}{\sqrt{\int \left(\mathcal{T}(\boldsymbol{\rho_1};M)-\int \mathcal{T}(\boldsymbol{\rho'};M)d\boldsymbol{\rho'}\right)^2 d\boldsymbol{\rho_1}\int \left(T(\boldsymbol{\rho_2})-\int T(\boldsymbol{\rho''})d\boldsymbol{\rho''}\right)^2 d\boldsymbol{\rho_2}}} \quad (4)$$

between the reconstructed $\mathcal{T}(\boldsymbol{\rho};M)$ and original $T(\boldsymbol{\rho})$ image. This factor is unbiased to any property of the target.

In ideal conditions, when the number of noiseless measurements is at the Nyquist sampling rate (without any compression), random illumination in conjuncture with linear cross-correlation image reconstruction cannot surpass any deterministic procedure. The situation changes however in the practical situations where imaging is performed in noisy conditions and, moreover, high compression ratios are desired. In this case, a random illumination approach permits decreasing the illumination coverage, while maintaining the overall intensity constant. This enhances the level of fluctuations in the signal and, according to Eq. (3), improve the CI's performance.

To evaluate the influence of the spatial light distribution over the target, we conducted numerical experiments of image reconstruction with different compression ratios. To mimic typical experiment conditions, the illumination distributions were blurred by a Gaussian spatial filter that eliminates the spatial variations smaller than the imposed resolution. The images were reconstructed via the linear cross-correlation between the fluctuations of the noisy integrated

intensity fluctuation and the ideal distribution of illumination. The result was then filtered to provide the same resolution as in the illumination. In the calculations, the random dots have a spatial fill factor of 5% and the Hadamard patterns were selected at random from the complete set. To compare and quantify the quality of image reconstruction we used the Pearson's correlation coefficient $\rho$ calculated at different compression ratios.

In Figure 1, we present the reconstruction of two different elements from the USAF 1951 standard chart, which were simulated as targets with unity reflectivity placed on a glass substrate with 0.04 reflectivity. The reconstruction was performed at a resolution of 32x32 pixels and corresponds to imaging conditions characterized by SNR=15dB. We also evaluated the corresponding Pearson's correlation coefficients for different levels of compression. Surprisingly, in the simulated noisy conditions, the orthogonal set of illumination patterns does not always have a better performance.

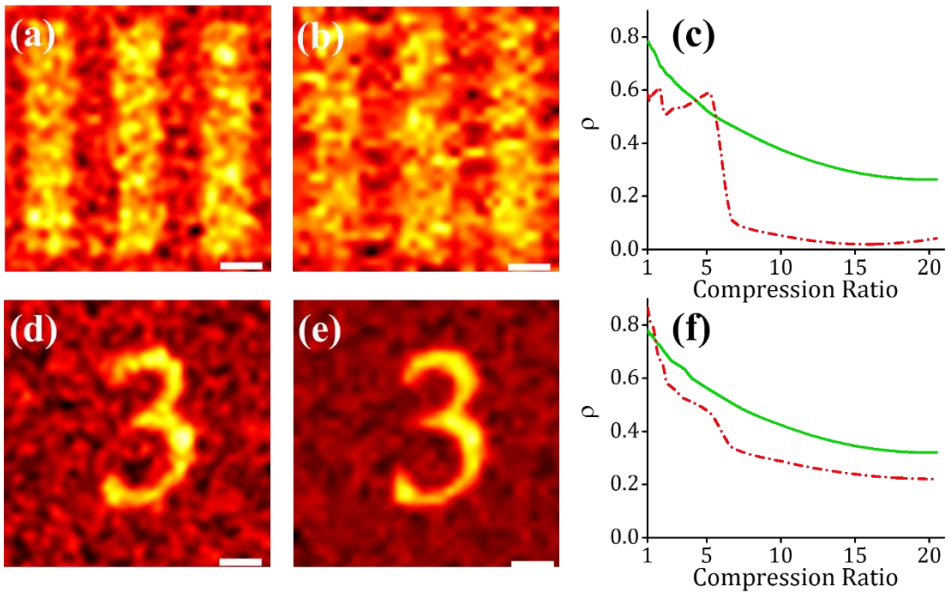


Figure 1 Simulated reconstructed images using illumination based on random dots (a,d) and a complete set of Hadamard patterns (b,e). Scale bar shows 5 effective pixels. (c,f) Pearson's correlation coefficients for different compression ratios (see text) for (-.-) Hadamard and (-) random illumination.

The explanation lies in the structural difference between these two targets. Due to its quasi periodic nature, the image of the three bars in Figure 1(a) is more compressible in the Hadamard

domain. As shown in Figure 1(c), both correlation coefficients saturate at some level below unity because of the noise influence, and this level is higher in the case of the random illumination. In the second case, however, the deterministic Hadamard patterns performs better for low compression ratio closer to unity. This happens because the Hadamard set samples the target uniformly in the spatial frequency domain. The spatial frequency representation of the first target covers only a limited domain and, therefore, the Hadamard set samples primarily the noise. As a result, in spite of the sharp increase in $\rho$ at lower levels of compression, adding more samples does not help the reconstruction. The random dot illumination on the other hand, samples the target uniformly in space and adding more samples always reduce the reconstruction error.

There is also another aspect that makes a random illumination appealing. When the illumination level is kept constant, the redistribution of light within fewer areas is beneficial in low SNR regimes; higher local intensities make the signal distinguishable from the noise. As result, the entire procedure becomes more robust to changes in the noisy environment especially for unbiased (target independent) compressive imaging.

In many applications, especially in biomedical optical imaging, the spatial resolution is critical. Ideally, when measurement time tends to infinity, the noise can be averaged out to some extent. Practically though, fast highly compressive techniques are desirable to track of dynamic target without compromising resolution. We tested the efficacy of random illumination in CI procedure at even higher resolutions. The results corresponding to different levels of compression in recovering 256×256 pixels images are summarized in Figure 2.

As can be seen, when the illumination is based on Hadamard patterns, one cannot reconstruct at all in these conditions. However, the procedure based on random illumination recovers the main object features even at compression ratios as high as 16:1. We also note that, although this target

does not have quasi-periodic nature, the attempt based on Hadamard patterns, shows some periodicity at high compression ratios which is not present in the case of random illumination. This periodicity originates in the superposition of a limited number of Hadamard patterns with randomly selected specific spatial frequency components. This restricted coverage of the spatial frequency domain is also the reason why the Hadamard based approach cannot reconstruct the smooth curvature of the target.

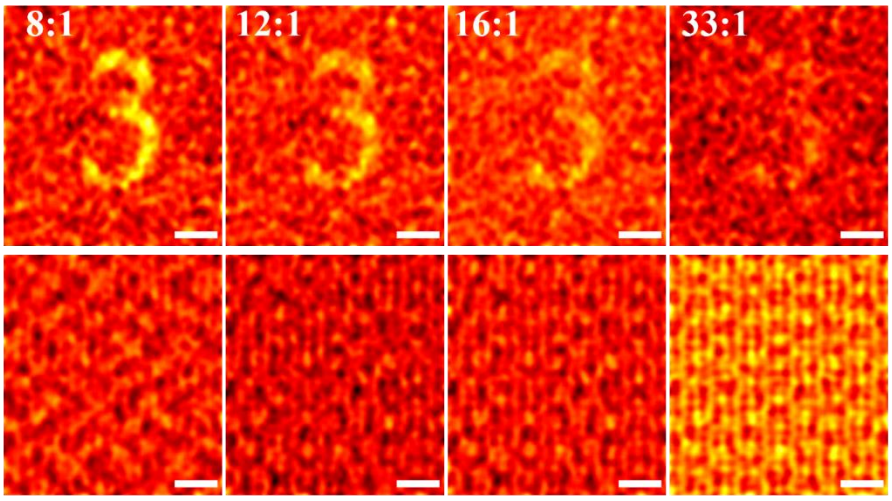


Figure 2 Simulated reconstructions with 256×256 pixels resolution for different compression ratios using random dot (top row) Hadamard (bottom row) illumination. The scale bar indicates 50 effective pixels.

The two types of illumination were also tested experimentally. For this purpose, a CI reflection microscope was implemented using a digital micro-mirror device (0.7" XGA VIS, TI DLP Discovery D4100 kit) to spatially modulate light generated by a CW laser with $\lambda$=532nm. The total reflection from the target is recorded with a PMT (Hamamatsu H6180-01) and the CI procedure is conducted as described before. For a better assessment, the experiments were conducted in the same conditions as in the numerical demonstration.

An example of image reconstruction at SNR≈12 is presented in Figure 3. From the evolution of Person's correlation coefficients, it is evident that the patterned illumination does not have a

superior performance necessarily. In fact, even without any compression the reconstruction is severely limited by the experimental noise.

The experimental demonstration summarized in Figure 3, confirms that, in noisy conditions and at low compression ratio, random illumination can have a better outcome as also suggested by the numerical simulations. It is true that the Hadamard illumination may benefit from the patterns' orthogonality but the propagation-induced spatial distortions can significantly diminish this advantage. Pattern distortion increases the cross-talk between different illumination frames which decreases the overall performance of this methods. However, randomly distributed illumination dots with low spatial coverage can be, in average, sufficiently separated such that the spatial aberrations do not modify significantly the cross-correlation between different frames.

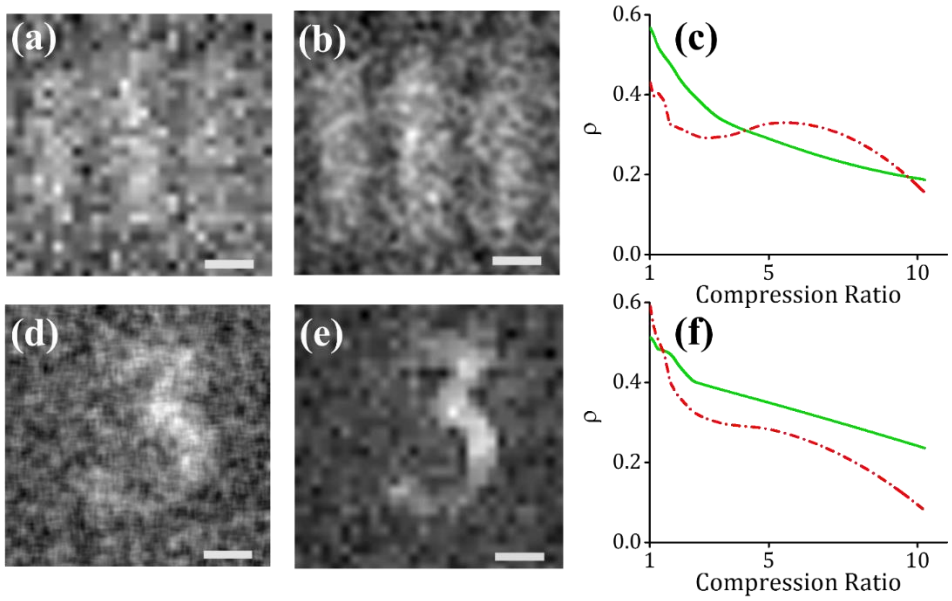


Figure 3 Experimental reconstruction of images using illumination based on random dots (a,d) and a complete set of Hadamard patterns (b,e). The scale bar represents 5 effective pixels. (c,f) Pearson's Correlation coefficients for reconstruction unde different compression ratios for (-.-) Hadamard and (-) random illumination.

Finally, we considered an experimental target reconstruction at SNR ≈ 10 for with an increased resolution of 256×256 effective pixels. The results are summarized in Figure 4 and, as can be clearly seen, the procedure based on random illumination is again superior at very high

compression ratios. These results also demonstrate that an image with 256×256 pixels, can be captured at a rate of about 10Hz with off-the-shelf spatial light modulators and in rather noisy conditions, which should be appealing for biomedical imaging applications.

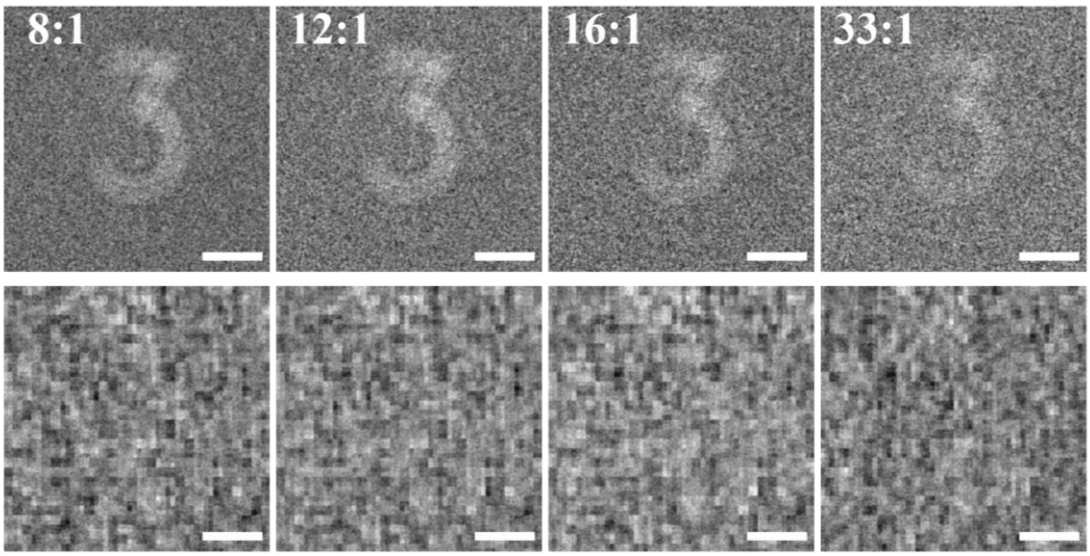


Figure 4 Reconstructed image for different compression ratio (top) random dot (bottom) Hadamard illumination. Scale bar corresponds to 50 effective pixels.

## Conclusion

Our numerical and experimental demonstrations indicate that correlation imaging using spatially random illumination patterns is a practical procedure that operates quite well at very high compression ratio and at noise levels compatible to realistic imaging situations. For this type of illumination, we demonstrated that increasing the number of illumination frames in compressive CI always improves the results. This, however, is not always the case for deterministic, patterned illumination. Of course, nonlinear optimization methods can be applied in image reconstruction process or post processing to improve the outcome for all types of the illumination, including the random illumination discussed here. Nevertheless, this comes at the expense of increased computational costs. We would also like to emphasize that in our demonstrations we did not use

any *priori* information about the targets and that the image reconstruction was solely based on simple linear cross-correlations.

Recovering high-resolution images of unknown targets in harsh experimental conditions, at high enough refresh rate, and using simple reconstruction procedure opens avenues for high-resolution video rate imaging over large fields of view. The ability to form high-contrast images in these conditions suggests that this approach may be of interest especially for biological imaging applications. Successful implementation of CI microscopy can therefore open new possibilities for real-time, in-vivo, and non-invasive examination of biological processes at cellular levels.

## Stochastic Optical Sensing

### Introduction

Measuring properties of random systems is ubiquitous. Their characterization can be approached in different ways but, in many situations, the only meaningful depiction is in statistical terms. For instance, in active sensing, information is recovered through a stochastic analysis of the system's output in response to controlled external stimuli. Examples include the characterization of structural dynamics [60] or individual scattering objects [61, 62] to mention just a few. Nevertheless, the external stimuli can be themselves stochastic like in the case of events of molecular origin [63].

In all these examples, the information about the targeted system is contained in the fluctuations of measured signals. Therefore, an efficient information retrieval requires augmenting such fluctuations, which is reminiscent of stochastic resonance [64]. We note that the traditional stochastic resonance approach relies on (i) some sort of system nonlinearity and (ii) an increase of the interaction energy through external control of the level of additional noise.

An effective enhancement of signal fluctuations can be generated not only by selecting a specific type of physical interaction but also by appropriate manipulations of the probing stimulus. Thus, it can be argued that using stochastic probing, one may be able to enhance the signal variability. This kind of approach may also extend certain practical attributes of the sensing process such as robustness against noisy and unpredictable environments.

## Fluctuation Based Sensing

In the rest of this chapter, we introduce a non-imaging statistical method for measuring characteristic length of scattering potentials. We will show that statistical features of a scattering medium can be recovered efficiently by simply controlling the statistical realizations $\xi$ of a stochastic probe $I(\boldsymbol{x};\xi)$ that interrogates the targeted system $T(\boldsymbol{x})$ via a multi-dimensional interaction in the domain $\{\boldsymbol{x}\}$. Briefly, we will show that changes in statistical parameters of a non-stationary probe $I(\boldsymbol{x};\xi)$ lead to abrupt modifications in the signals' statistics, which can be related to the target properties. Even though this approach is reminiscent of stochastic resonance, it does not come at the expense of increasing the energy of interaction with the targeted system and, furthermore, it does not require the presence of any nonlinearity. Moreover, because the non-stationary stochastic probe and the different possible sources of noise are statistically independent, I will demonstrate that this sensing methodology is robust against various external perturbations.

In practice, attaining a reliable signal encoded in $\boldsymbol{\rho}$ is often problematic because of, among other things, the limited bandwidth of a detection system and the presence of perturbations in both transferring the stimulus (perturbation in) and recovering the response from the target (perturbation out). In these circumstances, a preferable quantity to measure is the average (integrated) signal response

$$i(\xi) = A^{-1} \int_A \left[ \left( I(\boldsymbol{\rho};\xi) + n(\boldsymbol{\rho};\xi) \right) P(\boldsymbol{\rho};\xi) T(\boldsymbol{\rho}) + R(\boldsymbol{\rho};\xi) \right] d\boldsymbol{\rho}, \quad (5)$$

where $P(\boldsymbol{\rho};\xi)$, $R(\boldsymbol{\rho};\xi)$ and $n(\boldsymbol{\rho};\xi)$ denote all possible sources of perturbations in the sensing process. Notably, this measure cancels out the distortions in the return path as long as this information channel is lossless. It is also important to realize that the integration in Eq. (5) modifies the way in which the information is represented by projecting it from the $\boldsymbol{\rho}-$ into the $\xi$ $-$domain. This decreases the dimensionality of the problem and permits recovering stochastic information about $T(\boldsymbol{\rho})$.

Without loss of generality, we will consider an optical situation in which the intensity statistics of a two-dimensional illumination field is manipulated to recover information regarding a random scattering target $T(\boldsymbol{\rho}; l_T)$ characterized by the correlation length $l_T$. In this case, the interaction is described in the two-dimensional Cartesian domain $\boldsymbol{\rho}$ and $\xi$ represents a simple one-dimensional realization index. The general setting for this optical situation is illustrated in Figure 5. We note that the concept is not limited to back scattered light; a similar operation in forward scattering or any other direction can be described by simply folding the setup around the plane $\boldsymbol{\Omega}$.

A generic description of the targeted medium can be advanced using the concept of the scattering potential $\mathcal{P}(\boldsymbol{\rho}) = -k^2 \left[ n^2(\boldsymbol{\rho}) - n_0^2(\boldsymbol{\rho}) \right]$ where $k$ is the wave number, based on 1st Born approximation. This approach is commonly used in reconstructing distributions of refractive index variations $n^2(\boldsymbol{\rho})$ [65]. In this case, the averaged response $i(\xi)$ in Eq. (5), is, in fact, the average intensity of scattered light from the targeted scattering potential that fluctuates when the configuration $\xi$ of the excitation changes. The proposed stochastic sensing method relies on processing these fluctuations and not the magnitude of the integrated scattered signal itself.

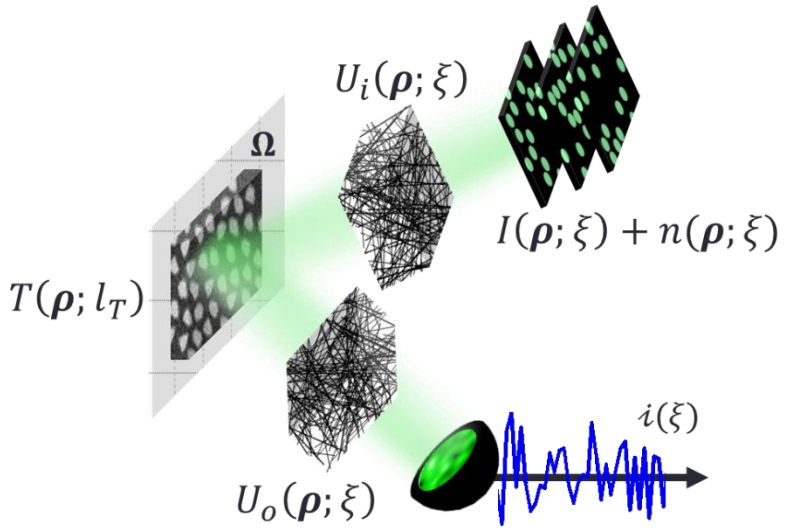


Figure 5 Schematic of sensing procedure with controlled stochastic illumination $S(\boldsymbol{\rho},\xi)$ affected by inherent source noise $n(\boldsymbol{\rho};\xi)$, and perturbations $U_i(\boldsymbol{\rho},\xi)$ and $U_o(\boldsymbol{\rho},\xi)$ in the illumination and recording paths, respectively. The measured signal is the averaged intensity $I(\xi)$.

It should be noted that, rigorously, the intensity distribution across a detector placed at an axial distance $\zeta$ from the target is $\mathcal{E}_S(\boldsymbol{\rho},\zeta)\mathcal{E}_S^*(\boldsymbol{\rho},\zeta)$, where $\mathcal{E}_S(\boldsymbol{\rho},\zeta)=\int \mathcal{P}(\boldsymbol{\rho}')\mathcal{E}_i(\boldsymbol{\rho}',0)\mathcal{G}(\boldsymbol{\rho}-\boldsymbol{\rho}',\zeta)d\boldsymbol{\rho}'$ is scattered field due to the stochastic illumination $\mathcal{E}_i(\boldsymbol{\rho},0)$. In this general scattering problem, the scattering potential is characterized by a complex field scattering coefficient $\mathcal{P}(\boldsymbol{\rho})$ ($|\mathcal{P}(\boldsymbol{\rho})|^2 = T(\boldsymbol{\rho})$) while the field propagation to the detector plane is described by the corresponding Green's function $\mathcal{G}(\boldsymbol{\rho},\zeta)$. However, one can show that the average scattered intensity can still be modeled with Eq. (5) for any $\zeta$, as long as propagation of scattered light is lossless, or if the loss is the same for all the realizations $\xi$. The interested reader is referred to Appendix B for more details.

In the following proof-of-concept demonstration, we consider only static scattering potentials but this is not a conceptual limitation. Temporal fluctuations and their evolution can be recovered using dynamic illumination with appropriate temporal characteristics. We also note that if all the realizations $\xi$ of the stimulus $I(\boldsymbol{\rho};\xi)$ would be known, one could, in principle, invert Eq. (5) to recover an "image" of static target $T(\boldsymbol{\rho};l_V)$ using variants of so-called "ghost imaging" techniques [9, 47, 66]. The problem at hand, however, is different as it refers to stochastic illumination in

noisy ambient conditions. In this situation the question is: can any information about $V(\boldsymbol{\rho}; l_V)$ still be recovered?

In the following, we will first outline how the statistical moments characterizing the scattering potential and the spatial and dynamic properties of the illumination relate to the fluctuations of the recorded intensity. Then, we will exemplify how this stochastic sensing formulation can be used in different practical applications. We will demonstrate the method's robustness against perturbations in both the structure of illumination and intensity detection.

## Stochastic Optical Sensing

The stochastic Fredholm integral equation, Eq. (5), relates the unknown scattering potential $T(\boldsymbol{\rho}; l_V)$ to four random processes $I(\boldsymbol{\rho}; \xi)$, $n(\boldsymbol{\rho}; \xi)$, $P(\boldsymbol{\rho}; \xi)$, and $R(\boldsymbol{\rho}; \xi)$. These processes are considered statistically stationary spatially and statistically independent of each other, which is a reasonable practical assumption. For each realization $\xi$, these processes are characterized by probability distributions and corresponding statistical moments with respect to variable $\boldsymbol{\rho}$. Upon averaging over an ensemble of all realizations $\xi$, these functions can be treated as constants in the further analysis.

We will now examine the impact of different type of fluctuating illumination intensity. First, we will discuss the case of a δ-correlated distribution defined by $\langle I(\boldsymbol{\rho}; \xi) I(\boldsymbol{\rho} + \boldsymbol{\rho_0}; \xi) \rangle_{\boldsymbol{\rho}} = \widetilde{m}_I^{(2)} \delta(\boldsymbol{\rho_0})$ with $\widetilde{m}_I^{(k)} = \left\langle (\tilde{I}(\boldsymbol{\rho}, \xi))^{\,k} \right\rangle_{\xi}$ in terms of $\tilde{I}(\boldsymbol{\rho}, \xi) = I(\boldsymbol{\rho}, \xi) - \langle I(\boldsymbol{\rho}, \xi) \rangle_{\xi}$. In this case, one can use the statistical properties of the distribution $\sigma(\boldsymbol{\rho}; \xi) = \big(I(\boldsymbol{\rho}; \xi) + n(\boldsymbol{\rho}; \xi)\big) P(\boldsymbol{\rho}; \xi)$ effectively impinging on the scattering potential to evaluate recursively the moments

$$M_T^{(k)} = \frac{\widetilde{m}_i^{(k)}}{\widetilde{m}_\sigma^{(k)}} - \sum_{n=0}^{\frac{k-2}{2}} \frac{k!\, \widetilde{m}_R^{(k-2n)}}{(k-2n)!(2n)!} \frac{\widetilde{m}_\sigma^{(2n)}}{\widetilde{m}_\sigma^{(k)}} M_T^{(2n)} \tag{6}$$

defining the spatial distribution of the scattering potential. The details of the derivation are included in the Appendix B. Of course, the reconstruction of higher-order moments must be considered in the context of overall procedural noise [67-70], which is not out concern in here. In practical cases when the first two moments are sufficient, it can be shown that the Fano factors $F_T = M_T^{(2)}/M_T^{(1)}$ and $F_i = \tilde{m}_i^{(2)}/m_i^{(1)}$ describing the scattering potential and the detected intensity, respectively, are related by

$$F_T = F_i \frac{m_\sigma^{(1)} m_i^{(1)}}{\tilde{m}_\sigma^{(2)}\left(m_i^{(1)} - m_R^{(1)}\right)} - \frac{\tilde{m}_R^{(2)} m_\sigma^{(1)}}{\tilde{m}_\sigma^{(2)}\left(m_i^{(1)} - m_R^{(1)}\right)}. \tag{7}$$

In Eq. (7), the Fano factor measures how significant the fluctuations are with respect to their average. This measure will be used throughout this section.

In the practical case when the correlation length $l_S$ of the illumination field is finite, then this length scale can be manipulated to infer information about the spatial properties of the scattering potential. The illumination can be thought as the convolution $I(\boldsymbol{\rho}; \xi, l_S) = e(\boldsymbol{\rho}; l_S) * C(\boldsymbol{\rho}; \xi)$ of a positively defined elementary unit $e(\boldsymbol{\rho}; l_S)$ with a spatially δ-correlated stochastic process $C(\boldsymbol{\rho}; \xi)$. In these conditions, we show in the Appendix B that

$$\tilde{m}_i^{(2)}(l_S) = \iint \langle \psi(\boldsymbol{\rho}; \xi, l_S, l_T)\psi(\boldsymbol{\rho}'; \xi, l_S, l_T)\rangle_\xi d\boldsymbol{\rho} d\boldsymbol{\rho}' + \tilde{m}_R^{(2)} \tag{8}$$

where the function $\psi(\boldsymbol{\rho}; \xi, l_s, l_T) = \tilde{\sigma}(\boldsymbol{\rho}; \xi, l_S) T(\boldsymbol{\rho}; l_T)$ denotes the intensity fluctuations of the scattered light without any perturbation $R(\boldsymbol{\rho}, \xi)$. As it is clear from Eq. (8) and in contrast to the previous case of δ-correlated illumination, finding the statistical characteristics of scattering potential involves a nonlinear inversion. This is a typical ill-posed problem that can be solved only in certain conditions and appealing to *a priori* information [70, 71].

However, information about the two-point correlation of the scattering potential can still be accessed without *a priori* knowledge by simply examining the fluctuations of the recorded

intensity over different realizations $\xi$ of the illumination intensity. In this case, the fluctuations of the integrated intensity become

$$\tilde{\imath}(\xi; l_S, l_T) = \int \begin{matrix} \tilde{I}(\boldsymbol{\rho}; \xi, l_S) P(\boldsymbol{\rho}; \xi) T(\boldsymbol{\rho}; l_T) d\boldsymbol{\rho} + \int m_I^{(1)} \tilde{P}(\boldsymbol{\rho}; \xi) T(\boldsymbol{\rho}; l_T) d\boldsymbol{\rho} + \\ \int n(\boldsymbol{\rho}; \xi) P(\boldsymbol{\rho}; \xi) T(\boldsymbol{\rho}; l_T) d\boldsymbol{\rho} + \int \tilde{R}(\boldsymbol{\rho}; \xi) d\boldsymbol{\rho} \end{matrix}, \quad (9)$$

which consists of four zero-mean statistically independent contributions. As a result, the second moment of the intensity fluctuations is simply the sum of the second moments of these four contributions. If the perturbations $\tilde{P}(\boldsymbol{\rho}; \xi)$ and $\tilde{R}(\boldsymbol{\rho}; \xi)$ are statistically stationary, the second moments of the last three terms are constant during the measurement. Thus, the overall level of the recorded intensity fluctuations is regulated by the value of the first integral in Eq. (9), which can be adjusted by varying $l_S$. In terms of spatial fluctuations $\tilde{e}(\boldsymbol{\rho}; l_S)$ of the elementary illumination unit, the first integral can be written as

$$\int \tilde{I}(\boldsymbol{\rho}; \xi, l_S) P(\boldsymbol{\rho}; \xi) T(\boldsymbol{\rho}; l_T) d\boldsymbol{\rho} = \int C(\boldsymbol{\rho}; \xi) \left( \tilde{e}\ (\boldsymbol{\rho}; l_S) * P(\boldsymbol{\rho}; \xi) T(\boldsymbol{\rho}; l_T) \right) d\boldsymbol{\rho} \quad (10)$$

This means that the value of this integral is determined by randomly sampling the convolution between $\tilde{e}(\boldsymbol{\rho}; l_S)$ and a perturbed projection of the scattering potential. When the characteristic lengths of this perturbed projection is much larger than $l_T$, it can be shown that the maximum of the intensity fluctuations in the first term in Eq. (9) is proportional to $\int \tilde{e}(\boldsymbol{\rho}; l_S) \tilde{e}(\boldsymbol{\rho}; l_T) d\boldsymbol{\rho}$. The contrast of these fluctuations depend on $l_S$ and, for a given average detected intensity, can be quantified by a corresponding Fano factor as shown before.

The procedure described above suggests a direct way to infer $l_T$ from the values of the Fano factor of recorded intensity as a function of $l_S$. When changing $l_S$, it is evident based on Cauchy–Schwarz inequality, that this Fano factor attains its maximum when $l_S = l_T$. The interested reader is referred to Appendix B for more details.

Same conclusion can be reached by analyzing this sensing process in the spatial frequency domain. It is clear that the dominant frequency components of the spectral distributions (Fourier transform of corresponding autocorrelation function) of the illumination intensity and the scattering potential will overlap when $l_T = l_S$. The similar extent of spectral distributions enhances the magnitude of the intensity fluctuations [72]. Of course, one could have used a deterministic illumination to reconstruct the characteristic length of the targeted potential. However, as follows from Eq. (9), a statistical analysis makes our method more robust to perturbations. Moreover, using random illumination may also lead to faster measurements.

We also note that this procedure is not limited to a single statistical process. A superposition of uncorrelated scattering potentials with different characteristic length scales can be represented, for instance, by a non-monotonic autocorrelation function leading to a Fano spectrum having multiple maxima. The repeatability of this technique is rather high because, as mentioned before, four terms in Eq. (9) are statistically independent. As a result, the variations in the Fano spectrum are independent from the considered perturbations. The repeatability is demonstrated in the Appendix B for different targeted potentials in noisy environments.

## Concept Demonstration

In the following we present a proof-of-concept demonstration in which we will incorporate two main requirements for a generic sensing procedure. First, when changing $l_s$, the total incident irradiance may change. Because in some circumstances the scattering potential could depend on the irradiance level, we impose that $m_I^{(1)}$ remains constant throughout the procedure. Second, sometimes there is simply no *a priori* information about the targeted potential and, therefore, an effective sensing method must sample it uniformly and isotropically.

**Uniscale Scattering Potential**

In the first example, we simulate a scattering potential based on a random array of circular disks with $l_T = \Delta$ and a volume fraction of 15%. Figure 6 (a) shows the normalized Fano spectrum of the intensity fluctuations corresponding to illumination patterns with varying $l_S$. The elementary unit used here is spatially isotropic. It is evident that the maximum in the Fano spectrum corresponds to the situation where $l_S = l_T$. This matching condition can be used to describe the targeted potential and the illumination, is rigorously demonstrated in the Appendix B.

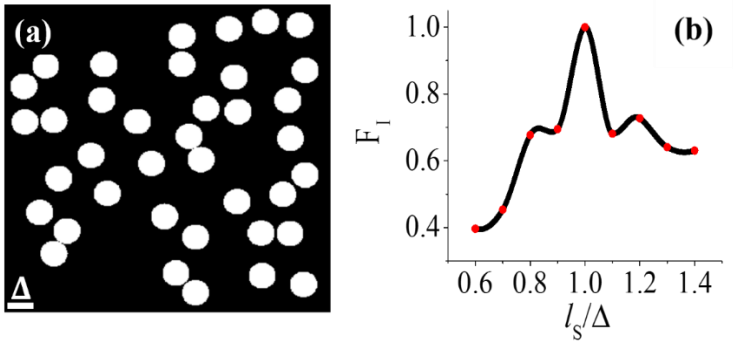


Figure 6 (a) Numerical calculations of the Fano spectrum corresponding to a random target consisting of circular disks with $l_T = \Delta$. (b) Fano spectrum measured in scattering from a reflective target characterized by two length scales of 8μm and 10μm. The maximum of Fano spectrum is normalized to unity.

**Multiscale Scattering Potentials**

In the first example, we considered a random system with only one length scale. The effectiveness of this stochastic sensing technique as outlined in Eq. (9) was also studied in more complex situations where the scattering potential has two characteristic lengths. For example, in Figure 7 we present the normalized $F_I$ spectrum corresponding to a scattering target consisting of two rectangular areas with width 2Δ, which are separated by a distance of 3Δ. To mimic natural perturbations, the illumination was purposely corrupted by additive noise: $I(\boldsymbol{\rho};\xi) + n(\boldsymbol{\rho};\xi)$. In addition, the scattered light was also distorted by additive and multiplicative white noise to effectively create detection conditions with an SNR of 2.5dB. As can be seen in Figure 7(b), even

in these highly perturbed conditions, the characteristic features of the target can be effectively recovered. This is the benefit of relying on statistical parameters, which makes the information distinguishable from the influence of any stationary perturbations.

In Figure 7(c) and (d) we present the results of an experiment where a reflective target consisting of 2μm wide strips and $10\mu m$ center to center distance was sequentially illuminated with 200 random realizations for each $l_S$ (in this case $\xi$ represents time). The illumination was generated using a liquid crystal spatial light modulator with pitch size of 15μm and 512×512 pixels. The backscattered light was integrated in a single photodetector with peak quantum efficiency of 0.38. The measurements were conducted in noisy conditions characterized by SNR=1.8dB and more details of the experimental setup detail are included in the Appendix B. As evident, both scale lengths characterizing this target are clearly identified in the experimental Fano spectrum.

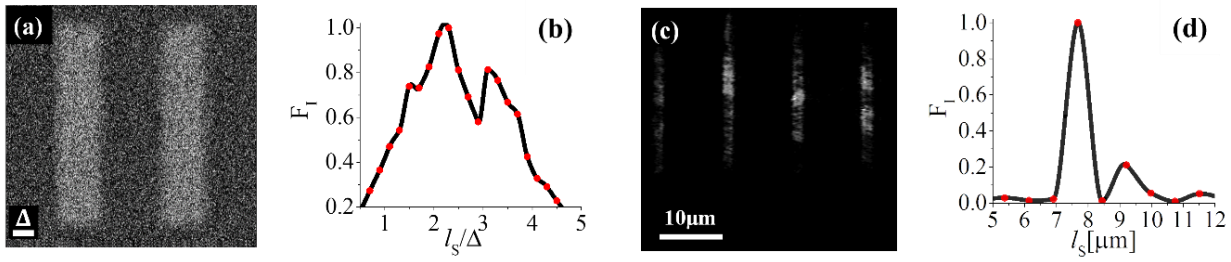


Figure 7 (a) Simulated reflective target perturbed by illumination noise and (b) the corresponding normalized Fano spectrum. The measurement conditions are similar to those in Figure 6. (c) Targeted standard microscopy chart under noisy illumination and (d) the corresponding normalized Fano spectrum.

In these examples, the correlation function characterizing the targeted potential is non-monotonic. For observing higher-order peaks in the Fano spectrum, the $l_s$ range of variation must be large enough to cover the spatial domain of interest. As a result, the level of variations in the first term of Eq. (9) is reduced, which determines the decrease in the overall level of fluctuations, as can be seen in the results summarized in Figure 7(b) and (d).

**Disturbed Illumination**

So far we have shown that perturbations that can be modeled as statistically stationary fluctuations do not degrade the performance of this stochastic sensing procedure. However, perturbations in the illumination path that can disturb the illumination structure may affect the results. In other words, the performance may be influenced by introducing uncertainties in the value of $l_S$, our only tuning parameter. This case is illustrated in Figure 8, were the size of the elementary function $e(\boldsymbol{\rho}; l_S)$ changes randomly according to a Gaussian distribution with a standard deviations of $\Delta/3$.

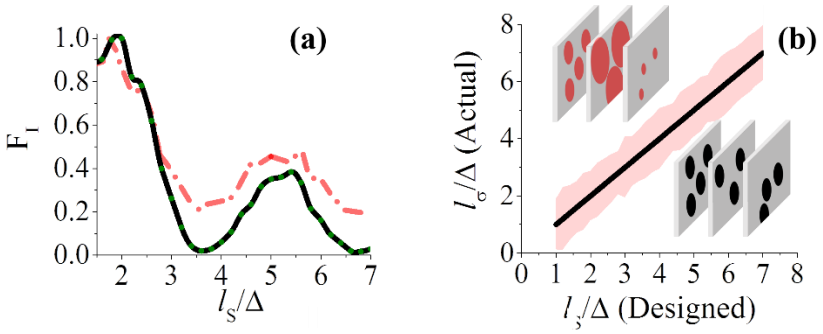


Figure 8 (a) Normalized Fano spectrum for an unperturbed condition (-) and for the case of $l_S$ distributed Gaussianly with a variance of $\Delta/3$ (-.-). (b) Correlation length $l_\sigma$ of the effective illumination (red shadow) as function of the correlation length $l_S$ of the unperturbed illumination (black solid line).

As suggested in the inset of Figure 8(b), this is a dramatic variation for the value of $l_S$. The Fano spectra corresponding to a scattering potential consisting of two rectangular objects characterized by length scales of $2\Delta$ and $5\Delta$ demonstrate that, even though the maxima broaden because of the uncertainty in $l_S$ , the characteristic length scales can still be clearly identified.

**Non-Sparse Scattering Potentials**

The examples illustrated so far prove the efficacy of this stochastic sensing procedure. They were, however, conducted on rather sparse scattering potentials. In the following we will

demonstrate that this is not a conceptual limitation. We will now model a target consisting of densely packed and randomly shaped objects characterized by a bimodal distribution of their scattering coefficients. To insure realistic measurement conditions, we include additional noise with SNR=2dB, added to both the scattering potential and the illumination pattern.

We consider potentials with different spatial symmetries, as shown in Figure 9(a) and (b). Note that, in the asymmetric case of Figure 9(b), some of the objects are more elongated and, due to the asymmetry in the density-density correlation function, they generate two additional characteristic length scales. As shown in Figure 9(c), this asymmetry is reflected in the Fano spectrum of the recorded intensity. The inset shows the ratio between the two spectra, $F_{i,Asym.}/F_{i,Sym}$, and, as can be seen, for larger values of $l_S$ associated with larger linear dimensions of the asymmetric objects, the difference between them increases because of an increased contribution of larger size objects. The auto-correlation functions of these two targets, are compared in Figure 40 in the Appendix B where additional discussion is provided.

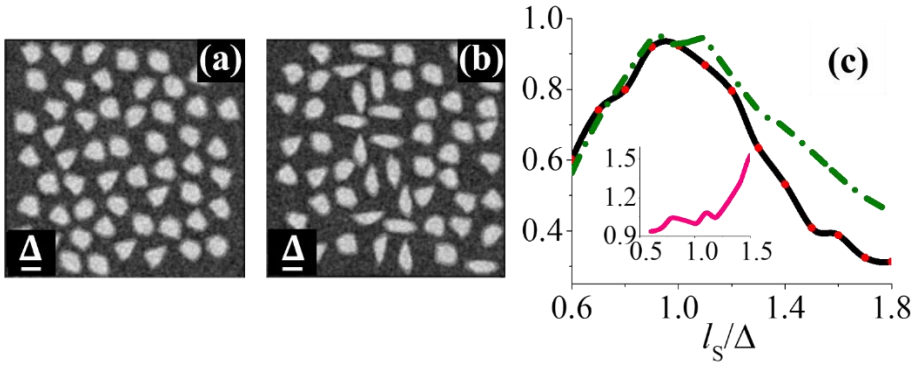


Figure 9 Simulated reflective targets consisting of randomly shaped objects having, on average, symmetric (a) and asymmetric (b) correlation functions. (c) Normalized Fano spectra corresponding to the symmetric (continuous line) and asymmetric (dashed line) targets, respectively. The inset shows the ratio of the two spectra as a function of correlation length $l_S$ the illumination pattern.

Clearly, only an averaged characterization is meaningful for the asymmetry of the targets illustrated in Figure 9. When the overall asymmetry increases, the corresponding Fano spectrum tends to develop maxima corresponding to the additional scales defined by the asymmetry and, as

a result, the spectrum displays a longer tail. As clearly seen in the inset, this departure from the symmetric signature evolves nonlinearly because of the way the variation of the first term in Eq. (9) reduces when the characteristic scale $l_S$ increases under conditions of constant total reflectivity.

**Weak Scattering Targets**

Up to this point we have shown that the stochastic optical sensing operates efficiently in harshly perturbed conditions and for different levels of target sparsity. Also important for a sensing method is its ability to recover information from the targets with different strengths of their scattering potential. To examine this property experimentally, we examined two different targets with very different back-scattering reflectivities. First we examined the high-contrast element 5 of the group 5 in the positive standard USAF 1951 chart with $l_T = 9.8\mu m$. This is close to case already shown in Figure 7(c-d). As a second example, we used a significantly less reflective target, a H2c9 cell placed in an aqueous medium (DMEH+10%FPS+1x p/s). The cell has an almost symmetric shape with a characteristic diameter of $\Delta \approx 10\mu m$, similar to the length scale characterizing the USAF chart. Similar illumination conditions were used and typical results of these two experiments are illustrated Figure 10. We note that during the 0.25 second illumination, the intensity of light used for cells characterization was eight orders of magnitudes smaller than the sunlight intensity. As clearly seen, the stochastic sensing technique works quite well even in the case of such low contrast targets. Moreover, repeatability of the procedure is rather high and the interested reader can find an ample discussion in the Appendix B.

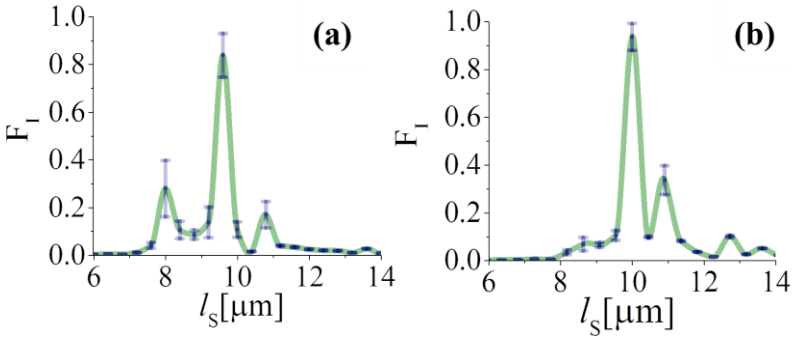


Figure 10 The average over 100 Fano spectra corresponding to (a) element 5 of group 5 of USAF 1951 positive resolution chart, and (b) a live H2c9 cell placed in aqueous medium.

## Conclusion

In conclusion, fluctuations are usually considered artifacts. In this section we proposed and demonstrated a stochastic sensing technique that relies on enhancing the fluctuations measured in a scattering experiment under structured illumination. Using the dispersion of the integrated scattered intensities fluctuations, we showed that characteristic lengths of the interaction potential can be consistently recovered. We have also demonstrated the efficiency of this method in extremely perturbed conditions, either in illumination or detection. In addition, we proved that this method is efficient in large range of the practical conditions. We successfully characterized targets with both very low and very high scattering coefficients.

Our stochastic sensing procedure can be regarded as a type of 'noise spectroscopy' where abrupt changes in the nonstationary properties of a signal are controlled by adjusting the stochastic properties of the excitation field. Varying the correlation length of the illumination can be exploited to recover structural information about the interaction potentials.

We also present a model, which essentially relies on the fact that, even for a Gaussian distribution of a random scattering potential, the scattered intensity is not necessarily Gaussian. By tailoring the illumination, one can therefore enforce non-Gaussian scattering processes leading to

measurable departures from the central limit theorem [73-76]. Being non-universal, these deviations are measurable signatures of specific properties of the scattering potential.

Finally, our experiments demonstrate that, in addition to being robust, the stochastic sensing approach is capable of providing spatial measurements with low error in highly noisy conditions (SNR below 2dB). This sensing method is not limited to the optical situations illustrated here and it should be appealing for a range of biomedical applications [77], material sciences [78, 79] and atmospheric characterization [80, 81]. Although the examples presented here addressed static scattering potentials, a similar stochastic sensing approach can be extended to characterizing dynamic phenomena [79, 82].

## Computational Compressive Stochastic Optical Sensing

### Introduction

Measuring properties of complex objects is a challenging task that can be achieved by various approaches. Even though the" signal" from a complex random object could be acquired and interpreted in different ways, in many cases the target can be meaningfully characterized only through statistical means [60, 61, 63]. Statistical parameters could be acquired directly or indirectly. For instance, one approach would be to "see" the object, i.e. record its image, and then process the observation to attain the desired statistical parameters indirectly [83-87]. Although seeing the object may appear useful, it is not always necessary [33, 61, 88]. Another possible strategy is to analyze the fluctuations of light scattered in response to an active probing field. Depending on the measurement goal, such fluctuations can provide different types of information. For example, enhanced fluctuations have been exploited for sensing individual events in biological systems [63]. Similar methods were applied not only for random dynamic targets [60], but also for static and deterministic ones [61, 62]. In Ref [33], for instance, fluctuations were intentionally

induced in the probing field to enhance certain characteristics of the sensing process such as robustness against unpredictable environments.

In light matter interactions where the physical interaction does not depend on the intensity of the probe field, securing practical signal-to-noise levels in imaging methods typically require higher field energy. However, if the information provided by the fluctuations is sufficient to characterize the target, the scattered field can be integrated, which can decrease significantly the illumination intensity. In this way, one can acquire information without over exposing the target, which is of paramount importance when working with biological targets.

A complex object or process may not be truly random in its nature, but, due to lack of knowledge, it can be modeled as a random entity. For instance, the structure and the activities of a live cell could be considered as a stochastic process although it may follow certain rules. Such processes can be examined by different means, however, most of the time the invasiveness raises serious issues. Characterizing properties of biological objects while maintain their viability imposes specific constraints which will be discussed in the following.

Living biological entities usually studied through time-lapse measurements [89-92]. However, as it was shown experimentally, light can affect the natural evolution of live cells [93-97]. Traditionally, it is well accepted that the usual exposure of up to approximately $10 nW/\mu m^2$ in a typical white light microscope is not harmful to live cells [98, 99]. This is usually asserted by end-point observations of cellular activities after the experiment. However, end-point observations are not always sufficient and, one can never be sure that the right thing was measured. There are several situations in which the light exposure was found to be harmful, for instance, to gametes or embryos [100]. For example, it was observed that the rabbit ova experiences retarded cleavage rates after about 12 hours of exposure to visible light with irradiance of just $5 pW/\mu m^2$ [101]. In

another study, it was experimentally documented that exposure times as low as 30 minutes at an irradiance levels of about 0.1 $nW/\mu m^2$ in the visible range can block the development of hamster embryos to the 2-cell stage. Additionally, it was observed that 3 hours of continuous exposure to visible light with an irradiance of approximately 0.01 $nW/\mu m^2$ can produce toxic effects, measured by the induction of reactive oxygen species and HSP70 stress indicator proteins [102]. Furthermore, female and male reproductive cells are known to be sensitive to an increase of reactive oxygen species as a result of visible light exposure. Impairment of the reproductive potential was observed both in *in-vivo* and *in-vitro* studies [103].

As can be seen, all these effects were mostly observed for light intensities comparable with those used in typical white light microscopes. One can conclude that experiments at higher intensity levels where effects such DNA damage [104] and phototoxicity [97] can be easily identified, experiments conducted at medium range intensities may also affect biological targets, especially in time lapse measurements. In these conditions, in addition to direct photobiological effects, heat can be generated locally due to small levels of absorption over extended periods. This thermal unbalance can affect the growth rate and the metabolism of the cells without having a visible impact on their shape and specific activity [105]. Consequently, light exposure can affect the cells during the observation and can lead to erroneous measurement data even though the biological targets can still be "healthy" at the end of the experiment.

Aside from the level of light irradiance, characterizing properties of biological objects requires specific measurement conditions. For instance, in natural condition, a cell is not isolated and it interacts with other cells in its neighborhood [106, 107]. Besides exposed light energy and complexity of the system, non-invasive optical characterization methods may have to overcome another natural constraint, i.e. random light scattering, which may render imaging impossible.

Consequently, a suitable characterization method, should 1) provide the capability to study an isolated target as well as entire populations of the objects, 2) is able to operate in low light scenarios, 3) should be able to work in presence of perturbations, and last but not the least, 4) has to keep exposed light energy as low as possible.

In the last section, we have introduced Stochastic Optical Sensing (SOS), and we have shown that this method is capable of characterizing an unknown object statistical properties without imaging it [33]. In the following, we will first discuss SOS in the context of the aforementioned requirements and constraints. Afterward we introduce the new concept of compressive Stochastic Optical Sensing (cSOS) with which one can measure statistical parameters of the objects using compressive sensing. As a result, in biological sensing scenarios, exposed light energy can be decreased even more which can be of certain interest in time-lapse studies. We will show that as opposed to the usual case of compressive measurement of deterministic parameters, statistical parameters of a targeted potential could also be measured directly using compressive sensing approaches. We will discuss pros and cons of this method, and at the end, we will provide experimental proof of concept demonstrations.

## Stochastic Optical Sensing

Stochastic Optical Sensing (SOS) has been developed as a noninvasive method to characterize a scattering potential. This method utilizes an active probing field and it has been demonstrated experimentally both in low light scenarios and in highly perturbed conditions [33, 108, 109]. By proper manipulation of the illuminating field, SOS provides means to enhance the variations of the detected signal and to recover specific features of the targeted medium.

Let us explain SOS in a more rigorous manner. Technically, SOS gauges the characteristic length scale(s) $d$ of a scattering potential $\mathcal{P}(\boldsymbol{\rho}', t; d) = k^2(n^2(\boldsymbol{\rho}, t; d) - 1)/4\pi$ with scattering strength

of $T(\boldsymbol{\rho};d)=\langle\mathcal{P}^{*}(\boldsymbol{\rho},t;d)\mathcal{P}(\boldsymbol{\rho},t;d)\rangle$, where $\boldsymbol{r}$ is the transversal coordinate in the interaction plane and $n(\boldsymbol{\rho})$ and $k$ are refractive index distribution and the wavenumber at wavelength $\lambda$, respectively. To do so, SOS exploits the properties of a stochastic probing field $\mathcal{E}(\boldsymbol{\rho},t;l)$ characterized by an intensity distribution $I(\boldsymbol{\rho},t;l)=\langle\mathcal{E}^{*}(\boldsymbol{\rho},t;l)\mathcal{E}(\boldsymbol{\rho},t;l)\rangle$ with the correlation length $l$. The scattered field is considered to be statistically stationary, at least in the wide sense, and it is fully characterized by its cross correlation function

$$\Gamma(\boldsymbol{\rho},\boldsymbol{\rho}',\zeta,t,\tau)=\langle\mathcal{E}_{\mathrm{S}}^{*}(\boldsymbol{\rho},\zeta,t;l,d)\mathcal{E}_{\mathrm{S}}(\boldsymbol{\rho}',\zeta,t+\tau;l,d)\rangle_{\alpha}, \tag{11}$$

where $\mathcal{E}_{S}(\boldsymbol{\rho},\zeta,t)$ represents the scattered field at a distance ζ from the interaction plane and $\langle\cdot\rangle_{\alpha}$ denotes the average taken over different scattered field realizations. The corresponding intensity distribution of the scattered field, $I_{\mathrm{S}}(\boldsymbol{\rho},\zeta,t;l;d)=\Gamma(\boldsymbol{\rho},\boldsymbol{\rho},\zeta,t,0)$, is

$$I_{\mathrm{S}}\,(\boldsymbol{\rho},\zeta,t;l,d)=\langle\mathcal{E}_{\mathrm{S}}^{*}(\boldsymbol{\rho},\zeta,t;l,d)\mathcal{E}_{\mathrm{S}}(\boldsymbol{\rho},\zeta,t;l,d)\rangle_{\alpha}, \tag{12}$$

where $\mathcal{E}_{s}(\boldsymbol{\rho},\zeta,t;l,d)=\int\mathcal{E}(\boldsymbol{\rho}',\mathrm{t};l)\mathcal{P}(\boldsymbol{\rho}',t;\mathrm{d})\mathcal{G}(\boldsymbol{\rho},\boldsymbol{\rho}',\zeta)d\boldsymbol{\rho}'$ and $\mathcal{G}(\boldsymbol{\rho},\boldsymbol{\rho}',\zeta)$ is the Green's function for the scattering problem. Stochastic Optical Sensing exploits the statistical properties of the integrated scattered intensity $\mathcal{i}(t,\zeta;l,d)=\int I_{s}\,(\boldsymbol{\rho},\zeta,t;l,d)d\boldsymbol{\rho}$ to acquire information about the targeted scattering potential. Using the asymptotic approximation of the Green's function in the linear regime, $\mathcal{G}(\boldsymbol{\rho},\boldsymbol{\rho}',\zeta)=\mathcal{G}(\boldsymbol{\rho}-\boldsymbol{\rho}',\zeta)\approx e^{i\boldsymbol{k}\cdot\boldsymbol{\rho}'}e^{ik|\rho-\boldsymbol{\rho}'|}/\zeta$, where $k=|\boldsymbol{k}|$, the integrated intensity becomes

$$\mathcal{i}(t,\zeta;l,d)\propto\zeta^{-2}\int_{\mathrm{A}}T(\boldsymbol{\rho},t;d)I(\boldsymbol{\rho},t;l)d\boldsymbol{\rho}, \tag{13}$$

where A denotes the area of interaction [33, 109]. In this approximation, the distance $\zeta$ is a constant scaling factor for the intensity and, it will be omitted from now on to simplify the equations. Figure 11 illustrates the concept in which an effective source with intensity $I(\boldsymbol{\rho},t;l)$ illuminates the targeted potential while the scattered light is collected by an integrating detector.

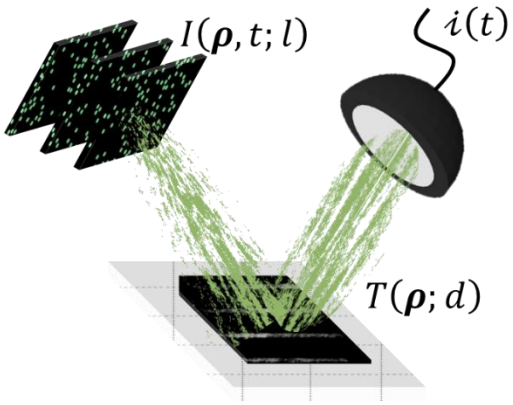


Figure 11 Schematic operation of Stochastic Optical Sensing. The light source creates a random intensity distribution I(ρ,t;l) with a spatial correlation length l which illuminates the targeted potential with characteristic length scale(s) d.

The variance of the integrated intensity depends not only on the properties of the scattering potential but also on the correlation length $l$ of the illumination field, which can be varied during the measurement [33, 110]. This procedure provides means to i) detect the presence of the object and ii) to characterize the scattering potential length scale(s). It can be shown that the variance of the integrated intensity [33]

$$\sigma_i^2(l) = \langle (i(t) - \langle i(t) \rangle_t)^2 \rangle_t \propto \int C_I(\Delta\boldsymbol{\rho}; l) C_T(\Delta\boldsymbol{\rho}; d) d\Delta\boldsymbol{\rho}, \tag{14}$$

depends on the autocorrelation function of the illumination intensity $C_I(\Delta\boldsymbol{\rho})$ and the autocorrelation function of the targeted potential scattering strength $C_T(\Delta\boldsymbol{\rho})$. According to the Cauchy–Schwarz inequality, $\sigma_i^2$ attains its maximum value when $C_I(\Delta\boldsymbol{\rho})$ and $C_T(\Delta\boldsymbol{\rho})$ have comparable spatial extents, or, in other words when $l \approx d$. The procedure to determine $d$ is as follows. For a given correlation length $l$ of the illumination intensity, an ensemble of realizations of the structured light is generated and then the corresponding variance of the integrated scattered light intensity $\sigma_i^2(l)$ is evaluated. The procedure is repeated for different correlation length $l$ and an entire spectrum of $\sigma_i^2(l)$ is constructed. The local maxima of this variance spectrum, identifies the length scale(s) $d$ of the targeted potential. This procedure can be implemented using both

randomly structured light [33] or stochastic distributions of coherent light, i.e. speckle patterns [108, 109].

It is worth mentioning that SOS can be used to characterize both sparse and dense targets. Furthermore, because the scattered light is integrated with a bucket photodetector, SOS is capable of operating in low light conditions, at intensity levels far below the usual white light microscopes [33]. Moreover, as natural experimental perturbations are statistically independent from the purposely enhanced fluctuations, they may affect the magnitude of the variance spectrum but will have limited influence on the location of its maxima [33, 108]. There is, nevertheless, an inherent shortcoming: the increase of the overall duration of exposure due to the sequential nature of the measurement. Although this may not be an issue for most measurements, it could become a problem in time-lapse studies of biological media where the noninvasiveness aspect is critical. Reducing the duration of the entire measurement procedure is therefore of interest and in the following section we will introduce the compressive SOS (cSOS) as a flexible approach for achieving this task.

## Compressive Stochastic Optical Sensing

As discussed earlier, in SOS each illumination pattern consists of features with a given correlation length $l$. Consequently, to acquire the variance spectrum associated with the scattering potential, one has to sweep over a range of length scales. In this respect, one could regard SOS as a scanning method similar to traditional confocal imaging for example. Generating the required ensemble of illumination realizations together with this sweeping through different types of illumination takes time.

To decrease the overall exposure time, we will take advantage of the well-known concept of compressive sensing [111-114]. Even though this concept can be applied in very different

circumstances relying on either deterministic or random sampling functions, in optical applications, to the best of our knowledge, compressive sensing has been exploited only for characterizing deterministic properties of an object, such as an image. Here we demonstrate a compressive approach using non-stationary random sampling functions to evaluate the characteristic lengths of a scattering medium, without imaging it. The main idea is that although the variance spectrum $\sigma_i^2(l)$ has a random and non-monotonic structure, the spectrum is a smooth and bounded function because of the limited spatial frequency content of any realistic target. Consequently, the variance spectrum $\sigma_i^2(l)$ should be recoverable by sparse sampling under certain smoothness constraints.

Now let us explain in more details the implementation of compressive Stochastic Optical Sensing (cSOS). For this purpose, we will use sampling functions consisting of random dots similar to the sparse sampling functions used in [28]. To sample simultaneously multiple points across the variance spectrum, we create multiple ensembles of illumination patterns, each with its own statistically stationary distribution. However, as opposed to SOS, in each ensemble, individual realizations contain features with multiple lengths scales. Figure 12 depicts schematically the conceptual difference between SOS and cSOS in an example for a number $N_l$ = 6 of length scales. In this figure, each color represents an ensemble of realizations of illumination patterns with stationary statistical properties. In conventional SOS, each ensemble is characterized by only one length scale $l_i$ but in cSOS every ensemble is associated with a set of length scales $S_i = \{l_{i1}, l_{i2}, \dots, l_{iM}\}$ consisting of $M$ randomly selected length scales. In this case, each length scale is present in $R \geq 1$ ensemble(s). This effectively increases the number of realizations associated with each length scale $l$. Consequently, the number of distinct ensembles of the illumination patterns reduces to $N_s = RN_l/M$. For instance, in the example illustrated in Figure 12, $M = 4$ and $R = 2$

and, as a result, $N_s = 3$ different ensembles are required to sample the variance spectrum. The ratio of $\rho = N_l/N_s$ defines compression ratio achieved in cSOS; it represents the factor by which the measurement time has been decreased.

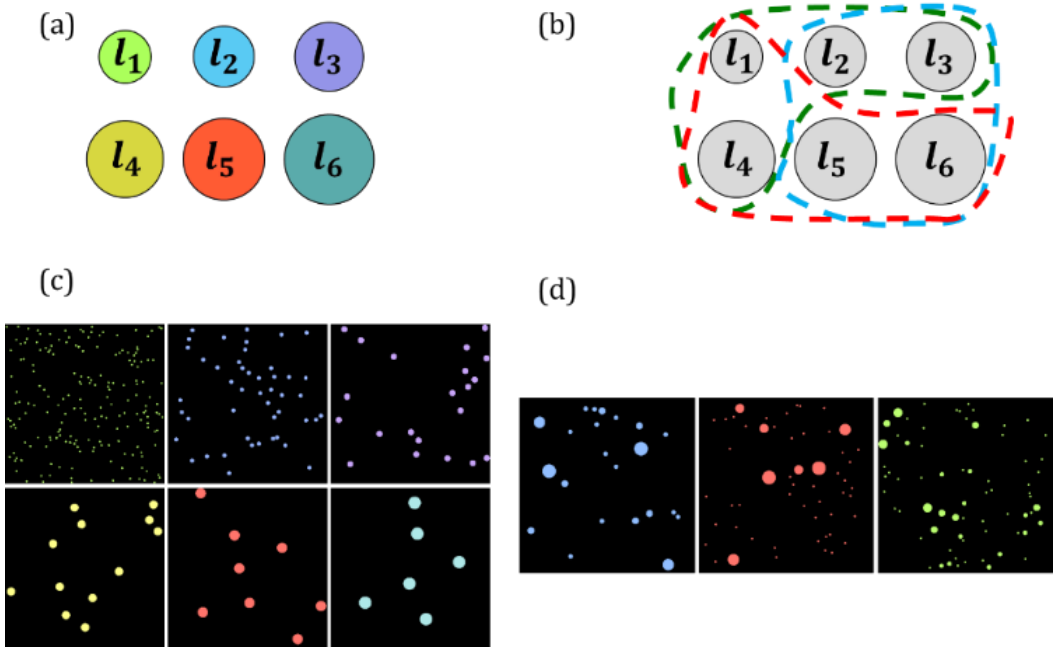


Figure 12 Generic illustration of the cSOS concept: distinct ensembles of illumination patterns indicated by different colors are assigned differently for (a) SOS and (b) cSOS. Each illumination ensemble is characterized by one specific length scale in SOS (c) and by features with multiple length scales in cSOS (d). In this particular example, the duration of the measurement is reduced by a factor $\rho = 2$.

Practically, this random sampling can be implemented by structuring the illumination intensity to include patterns with features of different length scales, for instance circular dots with different diameters as illustrated in Figure 12(d). In this case, each illumination pattern can be decomposed as linear superposition of $M$ secondary patterns $I = \sum_{m=1}^{M} I(\boldsymbol{\rho}, t; l_m)$, each characterized by a specific correlation length $l_m$. Consequently, the corresponding autocorrelation of the illumination intensity can be decomposed as

$$C_I(\Delta\boldsymbol{\rho}; S) = \sum_{m=1}^{\mathrm{M}} \sum_{n=1}^{\mathrm{M}} \langle I(\boldsymbol{\rho}, t; l_n) I(\boldsymbol{\rho} + \Delta\boldsymbol{\rho}, t; l_m) \rangle_t \qquad (15)$$
$$= \sum_{m=1}^{\mathrm{M}} C_I(\Delta\boldsymbol{\rho}; l_m) + \sum_{\mathrm{m}=1}^{\mathrm{M}} \sum_{\substack{n=1 \\ n \neq m}}^{\mathrm{M}} C_{I,eq}\left(\Delta\boldsymbol{\rho}; l_{eq} = \sqrt{l_n l_m}\right)$$

Where $S$ indicate set of length scales, $C_I(\Delta\boldsymbol{\rho}; l_m)$ denotes autocorrelation function of the secondary pattern with correlation length $l_m$ and $C_{I,eq}\left(\Delta\boldsymbol{\rho}; \sqrt{l_n l_m}\right)$ is cross correlation function between two secondary patterns with correlation lengths of $l_n$ and $l_m$, respectively.

Since in our example we have used circular features, the cross-correlation terms can be approximated with the autocorrelation function of an equivalent secondary pattern with a corresponding length scale $l_{eq}$. For circular features in a diffraction limited system for which $\min(l_m, l_n) \gg \lambda/2$, this equivalent length scale can be easily estimated using the first two terms of the Taylor expansion of the Bessel function, i.e. $J_1(x) \approx x(1/2 - x^2/16)$, to be the geometrical mean of the corresponding length scales, i.e. $l_{eq} = \sqrt{l_m l_n}$. As such, the autocorrelation function $C_I(\Delta\boldsymbol{\rho}; S)$ of the illumination patterns becomes simply a linear combination of the autocorrelation functions $C_I(\Delta\boldsymbol{\rho}; l_m)$ of the secondary patterns. Using Eq. (15) in Eq. (14), one can show that the measured variances $\sigma_i^2(S)$ are linear combinations of the components $\sigma_i^2(l)$ of the variance spectrum

$$A(S, l)\sigma_i^2(l) = \sigma_i^2(S), \tag{16}$$

where $A(S, l) \in \mathbb{R}^{N_s \times N_l}$ is a sparse transformation matrix. Each row of $A(S, l)$ represent an ensemble of realizations and contain at most $M(M-1)/2$ non-zero elements. In conventional SOS where each illumination ensemble encodes a single length scale, this transformation matrix is the identity matrix. In cSOS however, $A$ is a rectangular random matrix whose structure depends on the configuration of the different sets S of illumination length scales.

Equation (16) can be solved by minimizing the energy function

$$\epsilon(\sigma_i^2(l)) = \|A(S, l)\sigma_i^2(l) - \sigma_i^2(S)\|_2 + \phi(\sigma_i^2(l)), \tag{17}$$

for $\sigma_i^2(l) \geq 0$, where $\phi(\sigma_i^2(l))$ is a non-negative regularization function. Regardless of the specific targeted potential, the spectrum will be bounded and smooth because any realistic target has limited spatial bandwidth. This knowledge is exploited in the regularization function of Eq. (17) as we describe in detail in Appendix C. In the following sections, we discuss experimental implementation, results and considerations of cSOS.

## Experimental Demonstration

Stochastic Optical Sensing can be operated in different geometries, in transmission, in reflection, or at an arbitrary illumination angle. However, the reflection modality is preferred for biological studies, in particular in in-vivo experiments. This brings in an additional challenge related to the weak reflection contrast in most targets of interest. In the following, we will demonstrate the cSOS operation in reflection using targets with different scattering properties. We will also demonstrate the cSOS' capabilities in the context of time-lapse measurements.

A typical cSOS procedure is illustrated in Figure 13. An ensemble of realizations associated with each set of length scales illuminates the target and a detector integrates the scattered light intensity. Repeating the same procedure for $N_S$ sets, produces the time series of detected intensities shown in the left panel of Figure 13. For clarity, the time series associated with different ensembles are shown in different colors. Then, the variances of the corresponding time series $\sigma_i^2(S)$ are calculated to obtain the variance spectrum shown in middle panel. Finally, the measured variance spectrum $\sigma_i^2(S)$ is used in Eq. (17) to recover the variance spectrum $\sigma_i^2(l)$ that characterizes the target.

### Static Target

In the experiment, we used the setup illustrated schematically in Figure 14 where a beam of a doubled frequency Nd:YAG laser at wavelength λ=532nm was expanded using an afocal

system and then structured using a digital micromirror device (DMD) (DLI4130 0.7" XGA). The structured intensity at the plane of the DMD was then imaged on the target using a 4F imaging system consisting of a spherical lens (f = 45cm) and an objective lens (40X, NA=0.45). The back scattered light was then collected through the same objective and detected by a bucked photodetector.

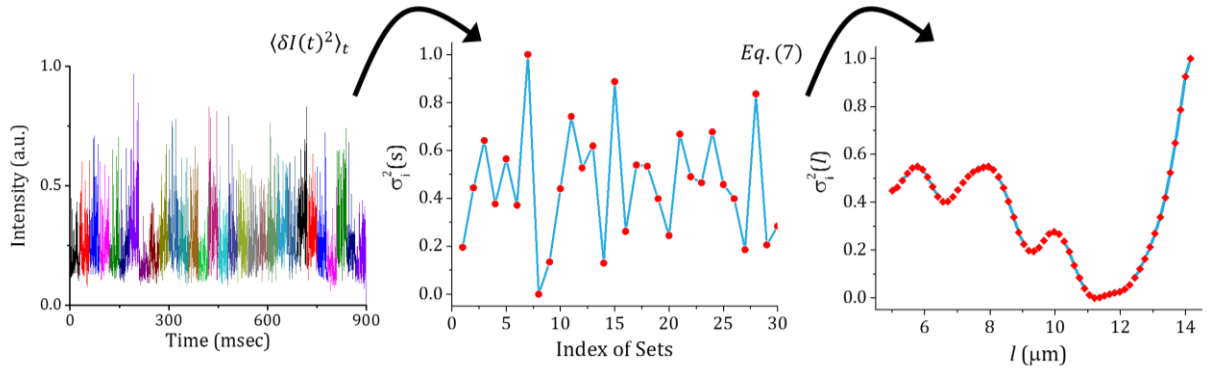


Figure 13 The experimental procedure of cSOS. From left to right, intensity times series associated with different ensembles of illumination patters are first recorded. The variance of measured intensity fluctuations are calculated and variance spectrum is obtained by repeating the first step for ensemble of illumination patterns associated with different sets of length scales. Lastly, the measured variance spectrum is used in Eq. (17) to recover the variance spectrum $\sigma_i^2(l)$ corresponding to the targeted scattering potential.

In Figure 14(b-e) we show the normalized variance spectra acquired for two different targets. In these experiments, each set $S$ consists of $M = 4$ randomly selected lengths scale and each length scale is supported by two randomly selected sets, i.e. $R = 2$. Consequently, the total exposure time reduces by a factor of $\rho = 2$, The fill factor of each pattern is also set at 2%. We used a large area photodetector (New Focus 2031) to collect the backscattered light intensity and, due to the available detector bandwidth, SLM was operated at 2kHz frame rate.

The first target shown in Figure 14(b) consists of two metallic strips with thickness of 400nm and width of 3-4μm spaced at about 17μm. The strips are deposited on the back of a coverslip No. 1.5 with a thickness of about 170μm. Although this target is highly reflective, because of its sparsity

the corresponding variance spectrum, shown in Figure 14(c), does not have very sharp peaks. In other words, in each realization of the illumination patterns, the interaction between the probe field and the metallic targets will have relatively low contribution to the total recorded intensity. Having a large contribution of unwanted fluctuations as result of background reflection, leads to the low visibility of the peaks in the spectrum [33]. This effect is observable in the spectra acquired in both SOS and cSOS modalities.

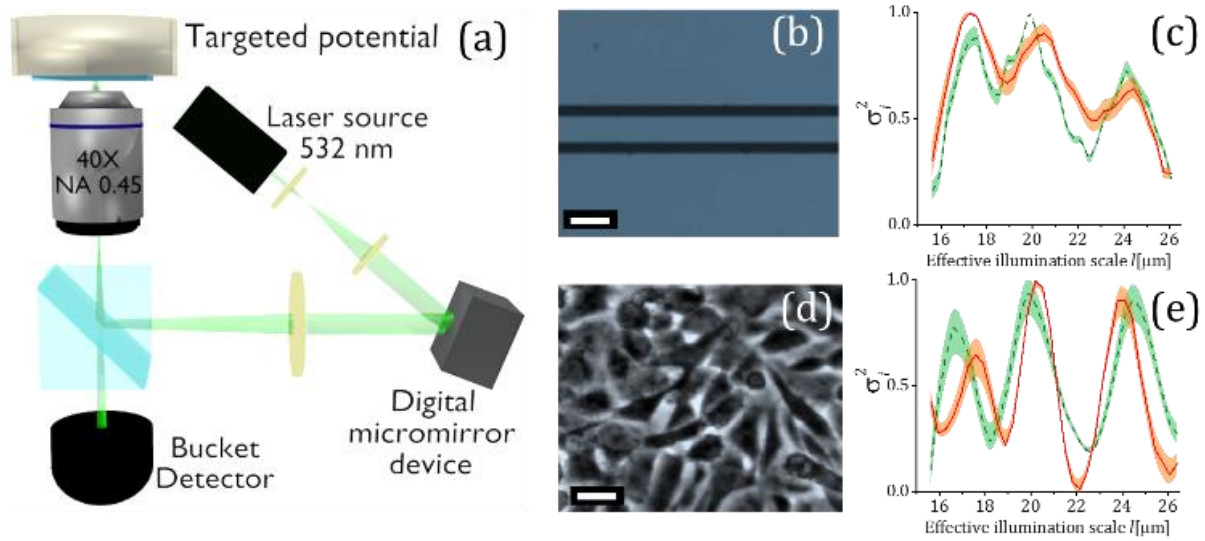


Figure 14 (a) Schematic of the optical setup. (b) Target consisting of metallic strips on glass substrate and (c) the corresponding variance spectrum. (d) Dense cell culture and (e) the corresponding variance spectrum. The dashed green curves and the green shaded area denoted the mean and the standard deviation of the variance spectrum measured using conventional SOS while the solid red and the orange shaded area represent the corresponding ones acquired using cSOS. The scale bar in (b, d) is $20\mu m$.

At the other extreme, we have used a target consisting of densely packed objects that scatter light weakly. Figure 14(d) shows an example of such a target which is a dense culture CHO (Chinese hamster ovary) cells in their appropriate laboratory scale media (10%FBS, 1% Pen/Strep containing DMEM). We have examined the part of the sample characterized by multiple characteristic lengths somewhat similar to the ones used in the last example. As opposed to the previous example, each cell alters the scattered field weakly. However, the collective contribution of the population results in significant variations of the integrated intensity. In other words, when

the illumination length scale is comparable with the characteristic lengths of the targeted potential, the weakly scattered light from different objects will be integrated coherently, which causes significant enhancement of the intensity fluctuations.

**Dynamic Target - A Time-Lapse Study**

The results presented in Figure 14 demonstrate the capability of both SOS and cSOS to characterize different length scales of the targeted potential at different level of the sparsity and the scattering strength of the target. In the following, we will apply cSOS in the context of a different type of application. As an example, we use culture of CHO cells with a vacant area in the middle of the culture and we characterize the lengths and time scales characterizing the live cells activity. This is similar to the geometry usually used in wound healing and cell migration experiments [84, 115, 116]. Figure 15 illustrates this geometry.

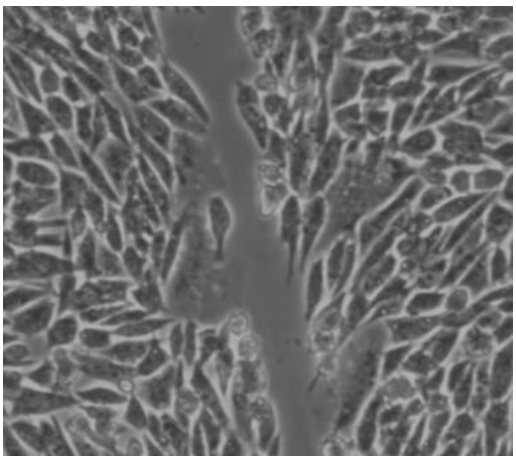

Figure 15 Wound healing geometry in a culture of CHO cells. In time, cells start to fill the gap uniformly by changing their shape and moving towards the gap.

The CHO cells were cultured in 10% FBS + 1% Pen/Strep containing DMEM in a glass bottom petri dish (MatTek P35G-0.170-14-C) with cover slip No. 1.5 on the bottom. The target was kept in a water-jacketed CO2 incubator for about 30 hours to assure that the cells are healthy and attached to the glass bottom. Then the cells were removed from a strip shaped area in the middle of dish and the culture sample was again left in the incubator for 30 min to stabilize. To keep cell

culture in an appropriate condition during the time-lapse measurement, the petri dish was kept in a tabletop incubator (Okolab UNO) with temperature, humidity, and CO2 level control. To avoid any long-term thermal effects, the objective temperature is also controlled using an objective heater (Okolab H–301–T), stabilized by the tabletop incubator controller.

We would like to emphasize that, having the cells alive throughout an experiment does not necessarily mean that the cells activity was not influenced by exposure to the light. For instance, Figure 16 shows the activity of CHO cells during a 12-hour measurement period over which cells are illuminated for about 2 seconds every two minutes with an intensity of approximately 1nw/μm2. Obviously, the cells are alive throughout the measurements, however, their motion is biased toward the illuminated area marked with the green square. This abnormality can happen, for instance, due to an increase in the local temperature that leads to a variation in the metabolism of the cells [105]. Furthermore, chemical production, e.g. reactive oxygen species [117], could also lead to unusual cell activities. To limit the role of such complications, while maintaining good signal-to-noise ratios, the bucket photodetector was replaced with a photomultiplier tube (PMT) that operates in much lower conditions. Furthermore, to avoid unwanted fluctuations in the detection system, the DMD was operated at 2.5kHz with a 75% duty cycle. The fill factor of each illumination pattern was also set at 1% to enhance even more the fluctuations of the scattered intensity. Measurements were repeated at one-minute intervals. We have also captured the image of the target over a large area using a weak short flash of incoherent light in transmission geometry.

We have applied cSOS to the culture of CHO cells in a geometry similar to the one shown in Figure 15 and the corresponding variance spectrum recorded over 20 hours of the measurement is presented in Figure 17. To follow the process of cells filling the gap, we have initially set the illuminated region at a vacant area in the middle of the gap. As clearly seen, after about an hour

the spectrum undergoes a significant change. Moreover, after this time, the spectrum starts to develop a local maximum around $l \approx 10\mu m$ which is equal to the averaged width of the cells. During the healing process, the cells change their shape and move towards the gap. This activity results in noticeable variations in the variance spectrum as can be seen at the beginning of the recording shown in Figure 17. At the end of the process though, the cells are densely packed and their shapes cannot change significantly, which translates into a rather constant shape of the spectrum as seen in in the last 1-2 hours of the measurement. In the following, we will examine different processes occurring during the measurement period.

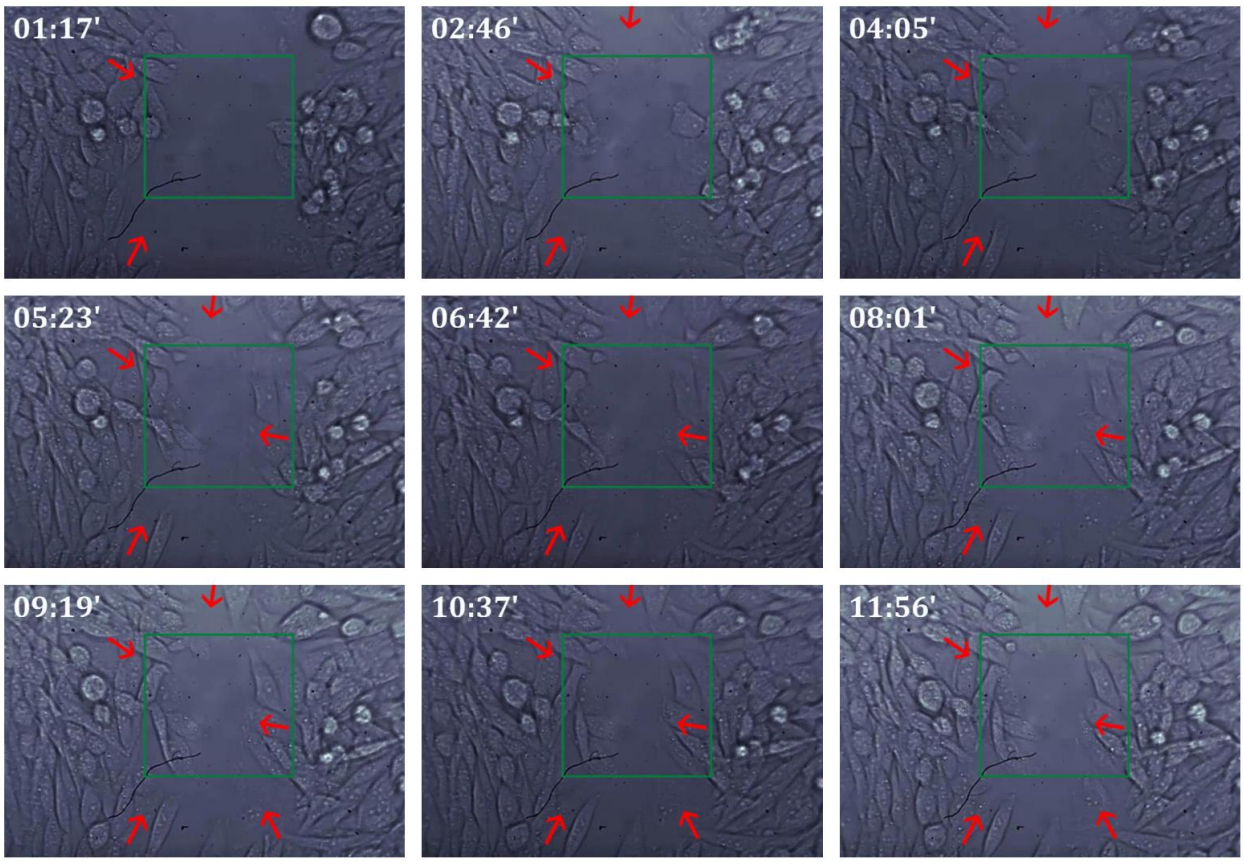


Figure 16 Time-lapse recording of CHO cells culture activities during a 12-hour measurement period over which cells are illuminated for about 2 seconds every two minutes with an intensity of approximately 1nw/µm2. Green rectangle indicates illuminated area and red arrows shows directional motion of some of the cells toward the illuminated area.

Any perturbation in the measurement enhances the variations of the integrated intensity. When such additional noise contributions are statistically stationary, the effect is a simple decrease of the

variance spectrum contrast. However, a straightforward normalization procedure can be used to suppress this noise contribution [33].

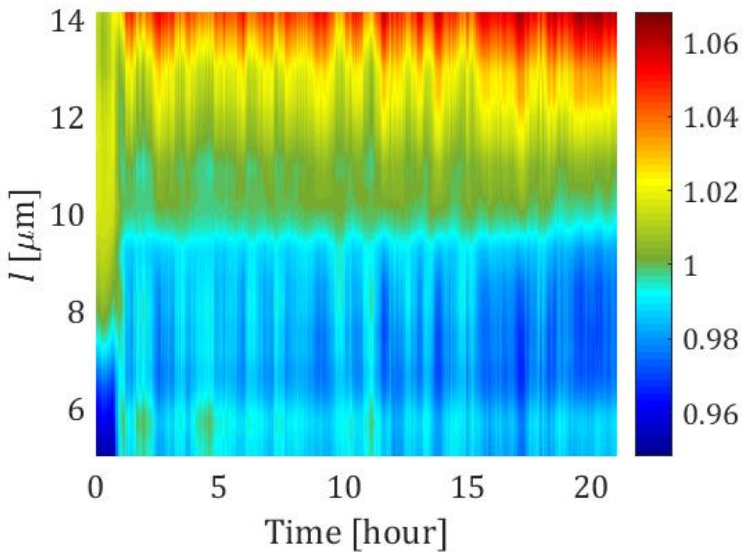


Figure 17 Experimental demonstration of cSOS in the wound healing experiment over a period of 21 hours. Change in the variance after about an hour and the relatively flat spectrum in last two hours are signatures of start and the end of the healing process.

In the following, we examine three typical examples in which the variance spectrum provides information about cell migration and ongoing biological processes without the need to actually imaging it.

Figure 18 shows a portion of the illuminated area over which cells start migrating in the first 2 hours of the measurement along with the corresponding normalized recovered variance spectrum $\sigma_i^2(l)$. The initially monotonic spectrum indicates the absence of the cells in the illuminated area. However, as the first cell moves into the illuminated area, the spectrum starts to manifest strong fluctuations at $l \approx 10\mu m$, which corresponds to the averaged width of the cells. As cell continues its motion, the entire cell enters the illuminated region and its average length determines a shift in the spectrum toward larger correlation lengths. Beside a shift in the peak

position, a non-monotonic behavior of the spectrum is apparent, especially when second and third cell come into the probed area.

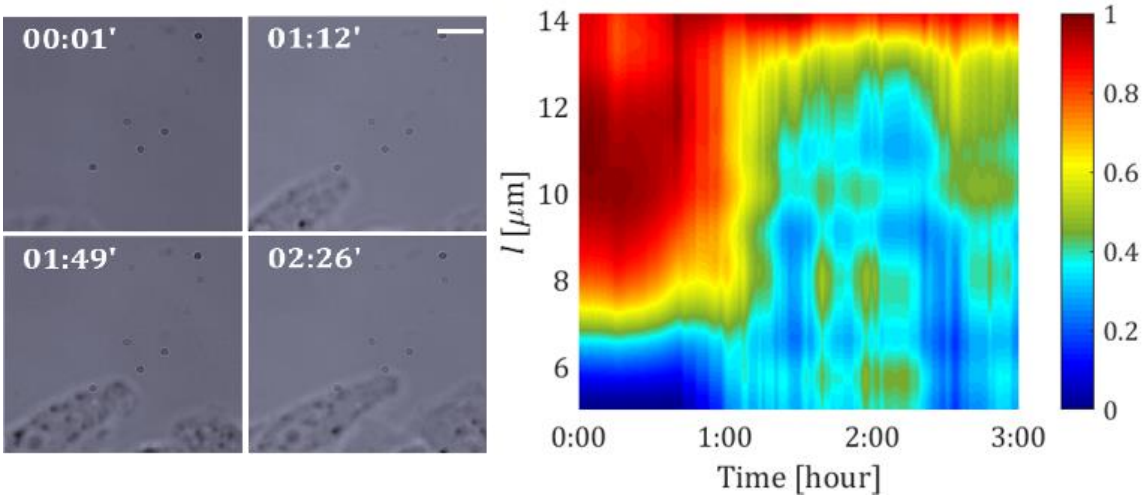


Figure 18 Beginning of the wound healing process. Left panel shows the illumination area at different time instances. For better clarity, the illuminated area is only partially shown; the rest is vacant for the first 3 hours. The scale bar is 10μm. Right panel illustrates the normalized recovered variance spectrum in the first 3 hours of the experiment. A shift in the spectrum is apparent as cells start migrating into the illuminated area.

Changes in the variance spectrum provide information about the objects and their dynamics, e.g. characteristic time of an event. For instance, as demonstrated in Figure 19, the duration of a cell division process can be determined using the temporal evolution of the variance spectrum. In this example, the change in the shape of the parent cell and the daughter cells introduces a small length scale of 8-10 μm that characterizes the division process. The emergence followed by the suppression of this small length scale is clearly identified in the spectrum and a characteristic time of 20 min typical for a division process can be easily identified.

As mentioned earlier, another parameter reflected in the variance spectrum is the time point that indicate end of the healing process. In wound healing geometry, this parameter shows the time in which cells motility decreases significantly, such that the culture looks almost stationary. In this condition, variance spectrum supposed to be flat in time as it is illustrated in Figure 20. As it is apparent, in last hour of the measurement, variation over the time decreases significantly, which

is signature of the end of the process. This is also apparent from the snapshot captured during this time.

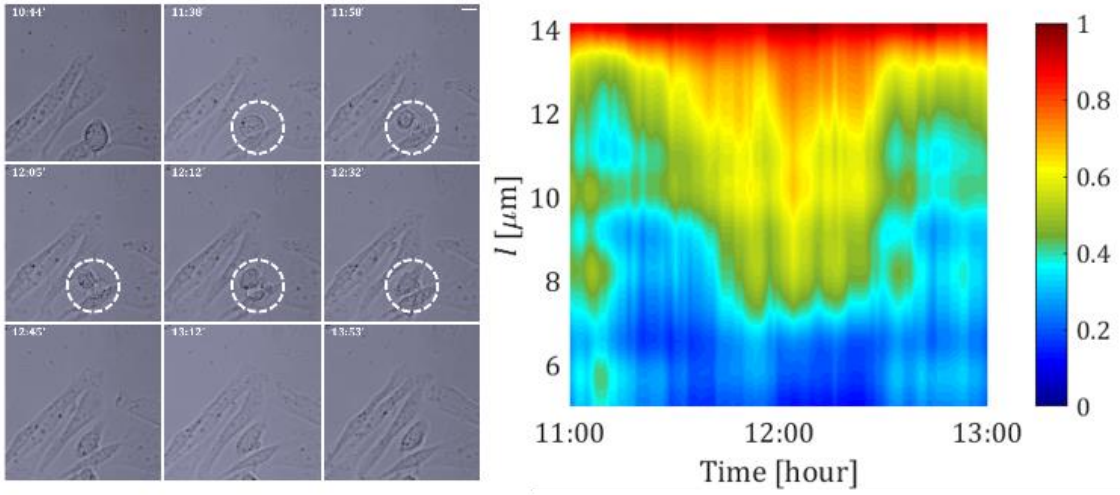


Figure 19 Change in the variance spectrum as result of cell division. Before the division, the parent cell changes its shape into a round structure characterized by a smaller length scale ($8-10\mu m$) with a slightly higher scattering coefficient due to higher density. Consequently, the fluctuations associated with this length scale are enhanced during the division process. After division, the daughter cells elongate and the spectrum changes again. The duration of this change reveals the characteristic time of the division, which is about 20 min. Scale bar is 10μm.

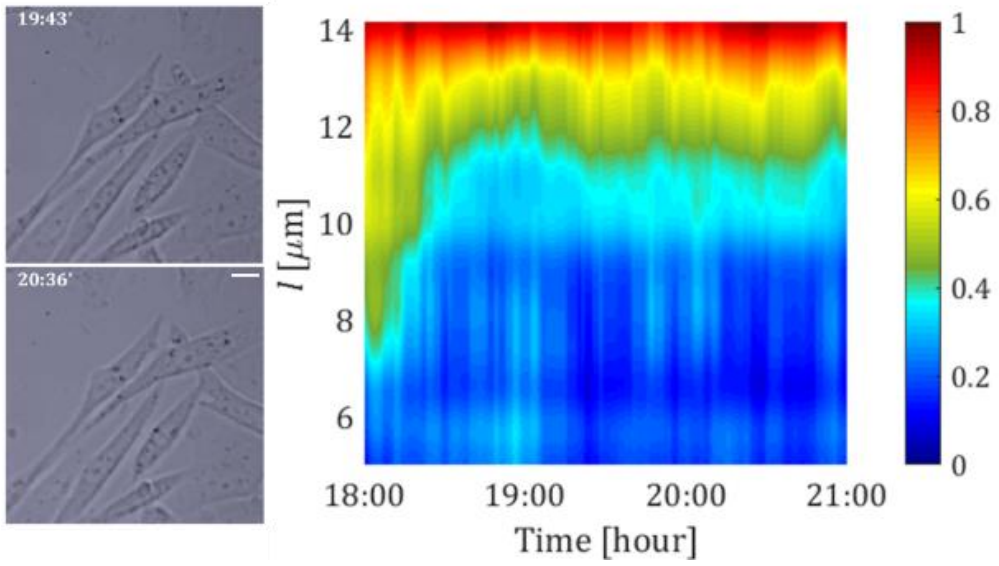


Figure 20 Variance spectrum in last 3 hours of the time-lapse measurement. Steady variance spectrum indicates the stationarity of the targeted potential or, equivalently, an indication of the ending of the wound healing process. Scale bar is 10 μm.

Presented demonstrations in Figure 18-20 are potential examples of applying cSOS for characterizing a biological sample both in time and in space without imaging it. Nevertheless, this method can be running over a long time without causing any collateral damages.

## Discussion

### Information Recovery Algorithm

In cSOS, for the same compression ration ratio $\rho = M/R$, the measurement transformation matrix $A(l, S)$ in Eq. (16) can be constructed in different ways. In our demonstrations, we have set the parameters $M = 4$ and $R = 2$ which determined a two-fold reduction in the exposure time. A compression ratio of two may not be impressive for a single measurement but, in time-lapse studies, this factor can improve significantly the experimental conditions. However, depending on the specific target properties, this compression ratio can be significantly enhanced [118].

Furthermore, the parameter M can also affect the nature of the integrated intensity fluctuations. According to Eq. (15), the ensemble averaged autocorrelation function of the illumination patterns can be effectively represented as linear combination of $M(M + 1)/2$ different autocorrelation functions. In these conditions, although increasing M may increase contribution of the off resonance length scales and make the peaks looks shallower, the effective decrease in the fill factor of the secondary patterns enhances the resonance fluctuations. Depending on the specific problem, these two processes can either enhance or suppress the visibility of meaningful fluctuations. However, because the information is embedded only in the location of the peak(s), the visibility can be further enhanced by post processing as it is discussed in Appendix C.

The other degree of freedom is $R$, i.e. the number of times each length scale appears in the length scale sets. In other words, $R$ indicates the number of times each physical length scale has contributed in the measured variances. Increasing $R$ makes the measurement more robust to

unwanted fluctuations. Although the number of the realizations in each ensemble is fixed, having $R > 1$ effectively increases the number of the realizations associated with each length scale at the cost of increasing the measurement time.

In last section, to demonstrate a general case, we kept $M$ and $R$ fixed for all the length scale sets although it is not required. In practice, one can vary these parameters across the sets to enhance certain characteristics of the measurement. For example, one can use larger $R$ for specific part of the spectrum that is more sensitive to the perturbation sources to reject the noise more efficiently.

In our demonstrations, we have assigned M length scales to each set $S$ randomly. Nevertheless, this association does not have to be completely random. This property could be used to address certain attributes of the measurement. For instance, using binary circular features, the actual fill factor may fluctuate from one ensemble to another, which determines unwanted fluctuations across the ensembles. These fluctuations can mask the meaningful variation of the ideally measured variances, especially if the target is weakly scattering. In cSOS though, one can tailor the association of the length scales to each set, to suppress the unwanted variations of the actual fill factor. Furthermore, the idea of sparse sampling of the smooth spectrum can be approached using different sampling functions. Here we have exploited the idea of the random dots sampling [28] that leads to random assignment of the length scales. However, this problem can be approached using different library based or orthogonal sampling function as well [119].

Besides the degrees of freedom in generating the illumination patterns, cSOS involves an additional, but very simple, computational processing step. This step however makes it possible to exploit prior knowledge about the realistic objects through applying physical constraints, e.g. smoothness and boundedness of the spectrum.

**Biological Systems Monitoring**

The main advantage of using cSOS for characterizing biological targets stems from its ability to perform in low light level and in various geometries. In usual white light microscopes, the level of the illumination intensity is in the order of 1-10 nW/μm$^2$ [98]. Considering the typical acquisition time of 50 msec, the energy density used for illumination is approximately 50-500 pJ/μm$^2$. In cSOS experiments presented here on the other hand, we utilized 3000 illumination patterns each lasting 0.3 msec, which resulted in 900 msec total illumination time. Moreover, for given fill factor of the illumination patterns of 1%, each point was illuminated, on average, for only for 9 msec. During the operation, the illumination intensity was set at about 1.3 pW/μm$^2$, which means that the corresponding energy density during cSOS operation was approximately 1.2 pJ/μm$^2$. This represents a reduction of almost two orders of magnitude from the levels used in traditional light microscopes. Consequently, even though in short-term measurements one could safely use imaging methods, in time-lapse studies this improvement offers the possibility to experiment in unprecedented conditions. Moreover, the energy density limits can be easily pushed even further by increasing spatial light modulator refresh rate or using low noise detectors.

## Conclusion

Phototoxicity is a major impediment in live cell microscopies. Reducing the optical irradiance to a minimum is a major goal for most optical techniques. What is worse is that having biological targets alive and motile after an experiment does not necessarily mean that the optical technique was “noninvasive”! In Figure 16, we have shown how the directional motility of normal cells can be easily altered in a common optical microscope. To avoid this problem by reducing the levels of exposure to light, we have proposed and demonstrated compressive Stochastic Optical

Sensing. We have compared its performance with conventional SOS and then we have exploited cSOS in a time-lapse measurement under low light illumination.

We have also shown that this method can operate efficiently not only in the case of sparse targets but also in conditions of dense packing such as the case of cell cultures. The cSOS approach is flexible and can be adapted to the task. The method relies on the random sampling of the variance spectrum followed by computational reconstruction developed under realistic physical constraints. We have also discussed effect of the different degrees of freedom in adjusting the illumination structures. The robustness, simplicity, and versatility makes this technique appealing for a range of sensing scenarios, especially in biomedical applications. Furthermore, requiring only tag-free targets and using the entire scattered light measured under low energy density illumination, makes this method a good candidate for low-contrast biological targets characterization over extended periods of time and without interfering with the natural biological processes.

# CHAPTER THREE: EXPLOITING FLUCTUATIONS OF LIGHT FOR DYNAMIC SENSING

## Optical Tracking of Dynamic Variations

In the last chapter, we have seen two imaging and sensing scenarios in which adding more randomness by tailoring the optical field helped to enhance the efficiency of entire procedure. However, manipulating the optical probe field structure is not always possible. For example, having a strong source of perturbation, either dynamic or static one, can make it impossible to impose specific spatial structure to the probe field [108].

The aforementioned condition can be observed in various practical cases. For example, imaging an object through the scattering media is a situation where controlling the spatial distribution of the light is impossible due to the multiple random scattering events [120-122]. In this case, using coherent light with or without feedbacks, one has to manipulate the available randomness, e.g. the statistical variation of the speckle field, for imaging purposes. A scattering lens [12, 123] is another example with which provided random interaction can be harnessed to enhanced resolution in an imaging scenarios.

Of course, using randomness is not limited to the imaging problems. For example, following a moving object behind a scattering obscurant is another interesting problem in which different stochastic events are involved. This problem is of interest, especially when the dynamic of the moving object is fast such that imaging methods cannot follow it. In this chapter, we will show that in this condition, one can achieve the task through exploiting the available probe, i.e. stochastic radiation, and its intrinsic statistical properties of its dynamic fluctuations [108, 109, 124].

## Tracking Hidden Objects Using Stochastic Probing

### Introduction

Aside from imaging, tracking the position of a scattering object is of paramount importance for biomedical [125, 126] and remote sensing applications [127-129]. Tracking scattering objects is commonly accomplished by RADAR and LADAR technologies that rely on directional probe beams that can be scanned spatially or angularly [127, 129]. Although very powerful and widely-spread, these approaches are less effective in perturbed environments or when operating on low-visibility targets obscured by other scattering media [130-134].

Of course, one way to track a target in the presence of an obscurant is to image it repeatedly over the time. While remarkable advances have been made in defeating imaging obscurants, this approach requires complex optical instruments and excessive data processing, which may be impractical for tracking fast moving objects [12, 120-122, 135].

However, to track an object, one does not necessarily need to "see" it! Capturing successive images of a target for further processing is not critical for tracking. For instance, the movement of an object hidden from the direct line of sight can be followed using a pulsed beam and time-gating the light scattered from the target, even though the light reaches the detector only through indirect paths [134]. Of course, this method will also fail when the environmental scattering increases or the object is completely surrounded by scattering obscurants.

Here we present a conceptually different approach for tracking an object in conditions where neither controlling the directionality of the beam nor scanning its direction are possible. We address the situation where the target is completely surrounded by heavily scattering media which completely conceals it. Conceptually, the target is placed inside a scattering enclosure that renders direct imaging impossible, as shown schematically in Figure 21. In this scenario, a primary source

of temporally coherent light is directed onto one of the scattering walls, which creates an effective secondary source for the radiation inside the scattering enclosure. The light scattered from the target is further randomized when passing through the scattering walls, and is then collected outside the box by an integrating detector.

The tracking problem illustrated in Figure 21 is solved by taking advantage of fundamental properties of partially coherent light. We will prove that the temporal and the spatial characteristics of field created inside the scattering box can be used to encode the full 3D trajectory of an object, which is effectively invisible from the outside. Even though the object is completely surrounded by multiple scattering media, its motion can be tracked in real time through a statistical analysis of integrated light. We will show that, when the dynamics of the diffused light inside the enclosure can be controlled at will, the variance $\sigma_i^2$ and the decorrelation time $\tau_i$ of the integrated intensity provide the sufficient information about the motion of the target. Moreover, we will demonstrate both analytically and experimentally that $\sigma_i^2$ and $\tau_i$ depend linearly and independently on the target displacement along the axial and transversal directions, respectively.

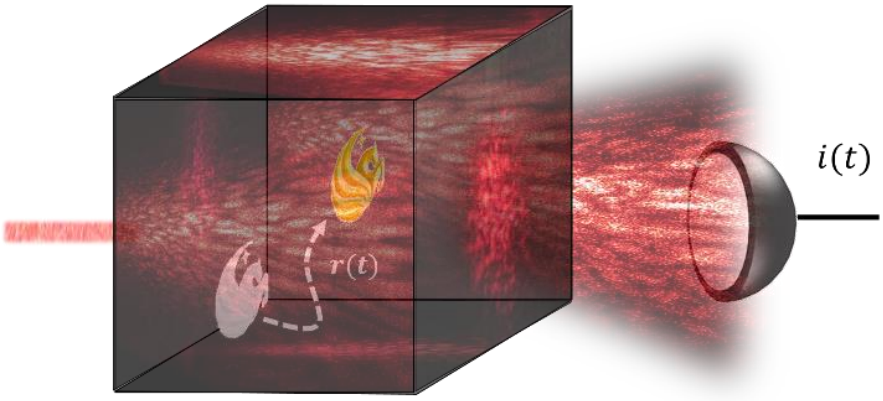


Figure 21 Tracking a hidden target enclosed in a "scattering box" that impedes direct imaging. A coherent source of radiation generates a spatially and temporally varying field which illuminates the target. Fluctuations of integrated intensity are detected outside the enclosure and are used to track the target position.

## Encoding Motion in Speckle Statistics

Coherent scattering generates optical fields that can vary both in time and space [136, 137]. In this section we will show that the trajectory $\boldsymbol{r}(t)$ of a scattering object can be recovered using the spatial and temporal statistics of a partially coherent field $\mathcal{E}(\boldsymbol{r},t)$ that illuminates the object. Let us consider the fluctuating scattered field $\mathcal{E}_s(\boldsymbol{r},t)$ that results from the coherent interaction between an illumination field $\mathcal{E}(\boldsymbol{r},t)$ and a generic, spatially locally homogenous, scattering potential $\mathcal{P}(\boldsymbol{r},t) = k^2(n^2(\boldsymbol{r})-1)/4\pi$, where $n(\boldsymbol{r})$ and $k$ are the refractive index distribution and the wavenumber at wavelength $\lambda$.. This scattering potential is characterized by its degree of spatial correlation $\gamma(\delta\boldsymbol{r})$ and its average strength $T(\boldsymbol{r},t) = \langle\mathcal{P}^*(\boldsymbol{r},t)\mathcal{P}(\boldsymbol{r},t)\rangle_\beta$ where $\langle\dots\rangle_\beta$ represents the average taken over different realizations of the scattering potential [65]. The scattered field, considered to be statistically stationary at least in the wide sense, is fully characterized by its cross-correlation function $C(\boldsymbol{r}_1,\boldsymbol{r}_2,t,\tau) = \langle\mathcal{E}_s^*(\boldsymbol{r}_1,t)\mathcal{E}_s(\boldsymbol{r}_2,t+\tau)\rangle_\alpha$, where $\langle\dots\rangle_\alpha$ denotes the average taken over different realizations of the interaction [138-140]. In practice, one usually measures the scattered field intensity $I_s(\boldsymbol{r},t) = C(\boldsymbol{r},\boldsymbol{r},t,0)$, which, within the accuracy of the first Born approximation, is given by [65]

$$I_s(\boldsymbol{r},t) = \left\langle\iint \mathcal{P}^*(\boldsymbol{r}',t)\mathcal{P}(\boldsymbol{r}'',t)\mathcal{E}^*(\boldsymbol{r}',t)\mathcal{E}(\boldsymbol{r}'',t)\mathcal{G}^*(\boldsymbol{r},\boldsymbol{r}')\mathcal{G}(\boldsymbol{r},\boldsymbol{r}'')d\boldsymbol{r}'d\boldsymbol{r}''\right\rangle_\alpha \qquad (18)$$

where $\mathcal{G}(\boldsymbol{r},\boldsymbol{r}')$ is the Green's function associated with the scattering problem. For reasons such as experimental simplicity, high signal level, etc., it is sometimes advantageous to detect the scattered intensity $i(\mathrm{t}) = \int_A I_s(\boldsymbol{r},t)d\boldsymbol{r}$ integrated over areas $A$ larger than the correlation length of the scattered field. It follows from Eq. (18) that the intensity integrated over the entire volume of interaction varies as

$$i(\mathrm{t}) = Mr^{-2}\int_V T(\boldsymbol{r}',t)I(\boldsymbol{r}',t)d\boldsymbol{r}' \qquad (19)$$

where the illumination field intensity is $I(\boldsymbol{r},t)=\langle\mathcal{E}^{*}(\boldsymbol{r},t)\mathcal{E}(\boldsymbol{r},t)\rangle_{\eta}$ where $\langle\ldots\rangle_{\eta}$ denotes the average taken over different realization of the illumination field. The Eq. (19) describes the intensity outcome of the coherent process of interaction and depends on both the degree of spatial correlation $\gamma(\boldsymbol{r})$ of the scattering potential and the degree of spatial coherence $\mu(\boldsymbol{r})$ of the illumination field. This dependence can be generically included in the pre-factor $\mathrm{M}\propto\iint\gamma(\delta\boldsymbol{r})\mu(\delta\boldsymbol{r})e^{i\boldsymbol{k}.\delta\boldsymbol{r}}d\delta\boldsymbol{r}d\boldsymbol{k}$ where $\delta\boldsymbol{r}=\boldsymbol{r}'-\boldsymbol{r}''$, evaluated over the extent of the target and the supported angular domain by detector over which the scattered intensity is integrated. A detailed derivation of Eq. (19) is presented in the Appendix D. Of course, in practice, one cannot effectively collect the entire scattered intensity. It is worth noting however that, in the scenario of interest here, further scrambling of the scattered field $\mathcal{E}_{s}(\boldsymbol{r},t)$ happens because of the propagation through the second diffusive layer. This directional homogenization together with the large-area integration makes the detected intensity to be well approximated by Eq. (19).

As apparent from Eq. (19), the integrated intensity $i(\mathrm{t})$ can vary by changing either the realization of the illumination intensity or the realization of the scattering potential. For rigid objects, the latter one is equivalent to changing the center of mass of the potential distribution, which can also be interpreted as the evolution of the object along a given trajectory. Consequently, it can be envisioned that if the statistical properties of the illumination intensity can be controlled, one can use the temporal fluctuations of the measured intensity to acquire information about the target motion. In other words, in a scattering experiment, information about the scattering potential can be retrieved by controlling the stochastic properties of the illumination field [33, 62, 63, 141, 142]. In the following, we will demonstrate that although the integrated intensity $i(t)$ in Eq. (19) cannot provide spatially resolved information, its temporal fluctuations relate directly to the motion of the

scattering target. We will show that the extent of the temporal correlations and the normalized variance of the time-varying signal $i(\mathrm{t})$ can be used to track the position of the scattering target.

Let us start by examining the possibility to follow the transversal motion. Of course, when different realizations of the illuminating field are completely uncorrelated, the transversal motion of the target will have no effect on the statistics of the integrated intensity detected outside the "box". However, if a certain degree of correlation exists between different illumination patterns, the target is exposed to more or less similar fields depending on its transversal motion between successive realizations of the illumination field. Consequently, it is expected that the dynamics of $i(t)$ will depend on the transversal velocity $\boldsymbol{v}_{T,\parallel}$ of the scattering object. One can then exploit the decorrelation time $\tau_i$ of the temporal autocorrelation function $C_i(\tau) = \langle i(t)i(t+\tau)\rangle_t$ to characterize this transversal velocity component.

A certain degree of spatial correlation between successive speckle realizations can be created, for instance, by translating the illumination field inside of the box along the transversal direction $+\boldsymbol{\rho}$. It follows that when the target moves along $+\boldsymbol{\rho}$ or $-\boldsymbol{\rho}$, the integrated signal $i(t)$ will decorrelate in time slower or faster. If the translation of the illumination speckle field can be imposed along any two non-parallel transversal vectors $\boldsymbol{\rho}_1$ and $\boldsymbol{\rho}_2$, the dynamic signal $i(t)$ can provide information about the 2D transversal motion of the target.

Of course, without feedback from inside the scattering "box" one cannot deterministically modify the illumination speckle. One can, however, take advantage of the so-called memory effect to effectively translate a speckle pattern over short distances [143, 144]. In spite of the multiple scattering, when the primary source of illumination is tilted outside the box, the speckles inside follow over a small angular range $\Delta\theta \propto 1/L$, where $L$ is thickness of the wall, as it is illustrated in Figure 22(a). When the target moves, the memory effect corresponding to the scattered intensity

from the target is affected: its angular range increases or decreases if the target moves along the same or in opposite direction. As a result, the fluctuations of the scattered intensity decorrelate at different rates depending on the target displacement.

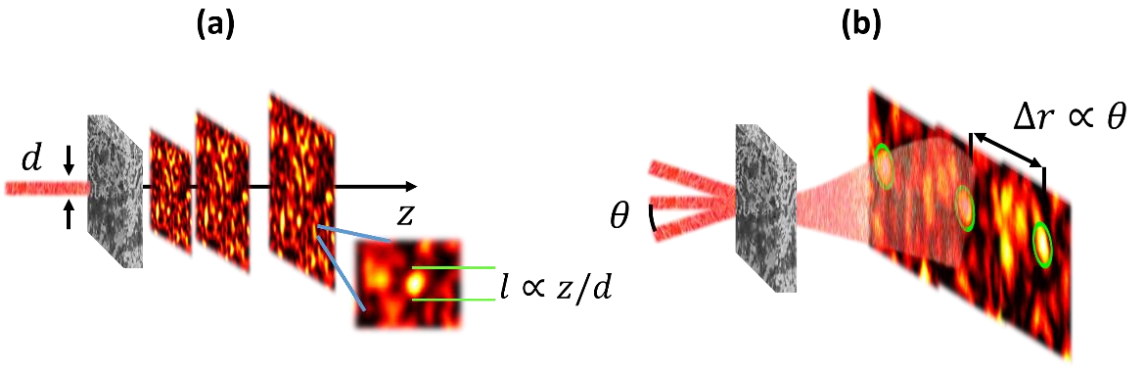


Figure 22 Schematic illustration of using (a) the memory effect associated with the light propagating through the scattering wall and, (b) the increase of the illumination speckle size used to encode the transversal and axial motion of the target, respectively.

Let us analyze this process in a more quantitative manner. When, during the measurement time $t_M$, the speckles are translated with constant velocity $\boldsymbol{v}_I$ along a given transversal direction while target moves with the velocity $\boldsymbol{v}_T$, the integrated intensity in Eq. (19) varies in time as $i(t) \propto \int T(\boldsymbol{r} - \boldsymbol{v}_T.t)I(\boldsymbol{r} - \boldsymbol{v}_I.t)d\boldsymbol{r}$. The corresponding autocorrelation function of these intensity fluctuations becomes

$$C_i(\tau) = t_M^{-1}\int_0^{t_M} C_I(\Delta\boldsymbol{r}(t) - \tau\,\Delta\boldsymbol{v})C_T\big(\Delta\boldsymbol{r}(t)\big)dt, \tag{20}$$

where $\Delta\boldsymbol{v} = \boldsymbol{v}_I - \boldsymbol{v}_T$ and $\Delta\boldsymbol{r}(t) = \Delta\boldsymbol{v}\cdot t$. In Eq. (20), $C_I = I(\boldsymbol{r}) * I(-\boldsymbol{r})$ and $C_T = T(\boldsymbol{r}) * T(-\boldsymbol{r})$ represent the spatial autocorrelation functions of the illumination speckle field and the targeted scattering potential, respectively, and $*$ denotes convolution operator. It has been shown in [143-145] that as a speckle field decorrelates in time due to the memory effect, the corresponding intensity autocorrelation function varies as $C_I(\Delta\boldsymbol{r}(t) - \tau\,\Delta\boldsymbol{v}) \approx (\xi/\sinh(\xi))^2 C_I\big(\Delta\boldsymbol{r}(t)\big)$ where $\xi \propto |\Delta\boldsymbol{v}|\tau$. It follows from Eq. (20) that the autocorrelation function of the measured intensity decays in time as

$$C_i\,(\tau) \propto (\xi\,/\,(\sinh(\xi)))^2 \int_0^{t_M} C_I\big(\Delta\mathbf{r}(t)\big) C_T\big(\Delta\mathbf{r}(t)\big)dt. \quad (21)$$

As can be seen, the decorrelation time depends on the difference $\Delta\boldsymbol{v}$ between the transversal velocity of the speckle field and the target velocity. In addition, when the characteristic time $\tau_{sp}$ of the speckle dynamics is smaller than the time scale $\tau_t$ associated with the target motion, $\tau_{sp} < \tau_t$, the target velocity along each axis can be approximated to be constant over a short measurement time (similar to "frozen model" in [65]) . Consequently, it can be shown that the integrated intensity $i(t)$ decorrelates after a specific delay time

$$\tau_i \propto |\boldsymbol{v}_I - \boldsymbol{v}_T|^{-1} \approx v_I^{-1}\left(1 + \frac{v_{T,\parallel}}{v_I}\right), \quad (22)$$

where $v = |\boldsymbol{v}|$. Thus, if the speckle velocity is kept constant along a given direction, the decorrelation time of the integrated intensity will depend linearly on the component of the target velocity oriented along the same direction of motion. Equivalently, during the short measurement time, the decorrelation time $\tau_i$ of the detected intensity will depend linearly on the transversal motion of the target. Detailed derivation of Eqs. (20-22) is presented in the Appendix D.

Having established the means to encode the transversal position of the target, we will now discuss the possibility to track its axial movement. As is well known, although the speckle field is statistically homogeneous in the transversal plane, its transversal correlation length, i.e. the extent of $C_I(\Delta\boldsymbol{r})$, increases with the distance from the secondary source, i.e. the wall through which the radiation enters the "box" [138, 139]. This increase in speckle size provides adequate means for encoding the axial position of the target, because it affects the level of fluctuations of the detected intensity. From Eq. (19), if follows that the variance

$$\sigma_i^2 = C_i(0) \propto \int_0^{t_M} C_I\big(\Delta\mathbf{r}(t)\big) C_T(\Delta\mathbf{r}(t))dt, \quad (23)$$

of the integrated intensity fluctuations $i(t)$ is determined by the characteristic length scales associated with both the target and the speckle size that illuminates it [33, 88, 110, 141]. According to the Cauchy–Schwarz inequality, the variance $\sigma_i^2$ attains its maximum when the correlation length of the illumination intensity is of the order of the characteristic length of the targeted scattering potential. In practice, the correlation length of $C_I$, i.e. the speckle size in the illumination field, increases in propagation and can, therefore, be used to gate the axial position of the target. On the other hand, as illustrated in Figure 22(b), the correlation length of $C_I$ is also inversely proportional with the size of the secondary source, $d$, which can be used to change the speckle size at a specific longitudinal position *z*. Varying $d$ leads to a stochastic resonance in the variance spectrum $\sigma_i^2(d)$, which can be measured in a fraction of second [33]. The position of this resonance, effectively encodes the axial location of the target. This property will be demonstrated in the next section.

In summary, the target motion can be encoded in the fluctuations of detected intensity as long as the spatio-temporal properties of an ensemble of realizations of the illumination field can be controlled at will. This ensemble can be created in different ways. For instance, a practically simple and convenient procedure is to simultaneously adjust the size, the tilt, and the position of the illumination beam across the input face of the "scattering enclosure". This process leads to fluctuations of the detected intensity $i(\mathrm{t})$ which are characterized by three independent parameters: the variance $\sigma_i^2$ of the integrated intensity and the decorrelation time $\tau_{i,x}$ and $\tau_{i,y}$ associated with speckle translation along x and y axes. As we have shown here, these measurable quantities encode changes in X, Y, and Z coordinates of the target in a linear fashion.

**Statistical Properties of Integrated Intensity: Experimental Validations**

We will now demonstrate experimentally that the decorrelation time $\tau_i$ depends linearly on the component of the target velocity parallel to the direction of the speckle motion. For this purpose, we place a scattering target near the center of a box made of 5mm thick Plexiglass covered with scattering layers of synthetic acrylics having a thickness of about $650\mu m$ and scattering mean free path of $70\mu m$. The overall size of the diffusive enclosure was 20cm×20cm×20cm. Speckle fields are generated by illuminating from the outside with an approximately 0.1mW HeNe laser beam with wavelength $\lambda = 632\ nm$ that can be tilted and translated laterally to create different realizations of the random field inside the box. The beam can also be mildly focused by an adjustable lens to control the size of the secondary source $d$ of diffuse radiation. In this arrangement, the ballistic light that passes thorough the box is attenuated more than eight orders of magnitude. Figure 23(a) illustrates the light scattered at the front and back walls of the scattering box. A large portion of the scattered field containing more than 1000 speckles is collected by a lens and detected with a photomultiplier tube. We note that this collection system can be placed anywhere outside the scattering box. The details of the experimental setup including the mechanical displacement of the target, the dynamic field generation, the detection of the scattered light, and the signal processing are all included in the in Appendix D.

The target is a Pegasus sign printed on a transparency sheet as shown in the inset of Figure 23. First, we will demonstrate the linear relation between target transversal motion and the decorrelation time included in Eq. (22). Following the procedure described in the preceding section, a focusing lens was used to fix the size of the secondary source at $d = 500\mu m$ and then a controlled translation ($\pm 1mm$) and a tilt ($\pm 5^{\circ}$) of the illumination beam was introduced by

adjusting the position and the inclination of the lens. Consequently, a transversal shift of the speckle field was created inside the scattering enclosure. The target was displaced with constant velocity along the same axis but in opposite direction while the integrated intensity was recorded for 1 sec. The amplitude of the corresponding autocorrelation function $|C_i(\tau)|$ as defined in Eq. (20) is plotted in Figure 23(b) for different values of the time delay $\tau$ and for different transversal displacement $\Delta x$ of the target. For clarity, we have plotted $|C_i(\tau)|$ over a limited range of time delays over which first zero crossing is observed. As can be seen, the dark band corresponding to $C(\tau) = 0$ clearly demonstrates the linear dependence between the decorrelation time $\tau_i$ and the target displacement $\Delta x$ as indicated in Eq. (22). Because, in this example, the target and the speckle field moved in opposite directions, the decorrelation time decreases when the target speed increases.

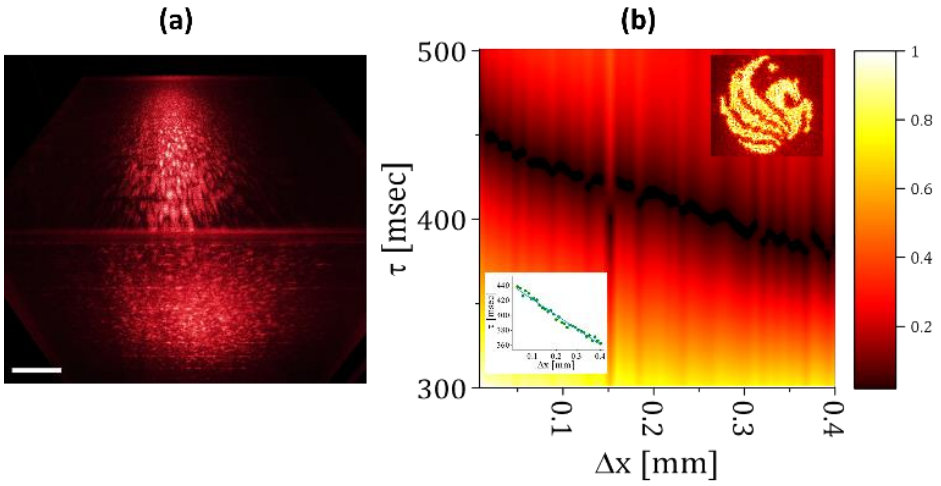


Figure 23 (a) Image of a laser beam with beam waist of $d \approx 520\mu m$ scattered at the front and back walls of the box. The scale bar is 2.5 cm. (b) Amplitude of the autocorrelation function $|C_i(\tau)|$ of the recorded intensity corresponding to different target transversal displacements $\Delta x$. The decorrelation time (black band) depends linearly on the target transversal motion as expected from Eq. (22). the lower left inset denotes linear relation between the decorrelation time and the target transversal motion. The upper right inset shows the approximately 5mm×5mm size object under uniform illumination.

In the next step, we validate the non-monotonic variation of the integrated intensity variance $\sigma_i^2$ as a function of speckle size, which is suggested in Eq. (23). When the target's axial location is fixed, the size of the speckles that illuminates it changes only by varying the size of secondary

light source $d$. In these conditions, one can examine, as function of the $d$, the stochastic resonance that occurs in the variance spectrum $\sigma_i^2(d)$ of the integrated intensity. The different realizations of the speckle field corresponding to a specific value of $d$ are generated by tilting and translating the primary beam across the front face of the scattering as described earlier.

Figure 24 illustrates this phenomenon of stochastic resonance when the secondary source size, $d$, was changed by varying the size of the illumination beam from $450\mu m$ to $600\mu m$. The maximum in the variance spectrum is evident. Depending on the target structure, scanning over a larger range may result in multiple resonances but, for our present purpose, a coarse scan over a short range is sufficient.

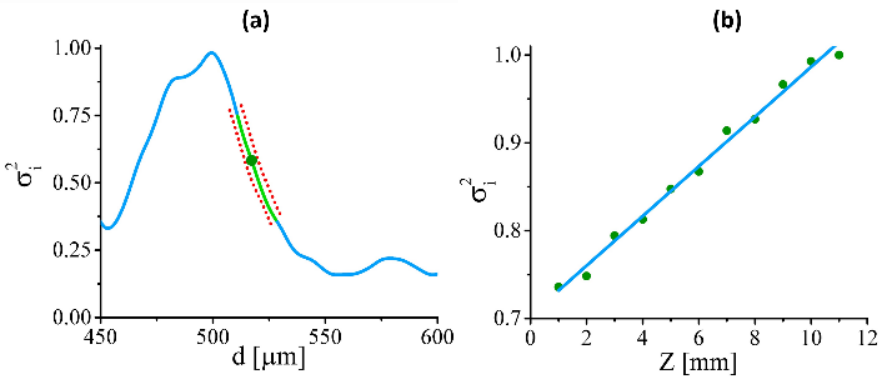


Figure 24 (a) Integrated intensity variance spectrum for varying secondary source size d, the dotted red curve indicates the shift in the variance spectrum as a function of axial motion of the target for ±2 mm. The green dot shows the optimum secondary source size $d_0 \approx 520\mu m$. (b) Linear dependency of the integrated intensity variance as a function of the target axial displacement for $d = d_0$. For clarity, all measured variances are normalized by the value of the maximum variance.

The variance spectrum such as the one in Figure 24(a) can now be used to identify an optimal size $d_0$ of the secondary source such that, locally, the spectrum changes linearly as function of speckle size. For instance, in the example illustrated in Figure 24(a), this is value is $d_0 = 520\mu m$ as indicated by the green dot. In practice, there could be additional considerations for identifying $d_0$ such as (i) the overall range over which the linearity approximation is valid and (ii) the value of the local gradient that defines the sensitivity to changes in the speckle size.

Having identified and fixed an optimum size of the secondary source $d_0$, any further changes in the size of the interacting speckle can only be due to changes in the axial location of the target. Consequently, the linear variation of $\sigma_i^2$ with the average speckle size can be used to track the axial location of the scattering target. To demonstrate this experimentally, the size $d_0$ of the beam was kept constant and the target axial location Z was varied. The measured variance of the integrated intensity is shown in Figure 24(b) where the linear dependence between the location of the target and the position of the stochastic resonance is evident.

**3D Trajectory Recovery**

In the following, we present a proof-of-concept demonstration of tracking the 3D trajectory of an object completely surrounded by a "scattering box" as illustrated in Figure 21. The variance and the decorrelation time of the recorded signal are evaluated to reconstruct the target trajectory inside the box. The procedure is as follows. In the first step, the optimum size $d_0$ of the secondary source is identified and kept fixed as it discussed in last section and illustrated in Figure 24. Once the optimal range is found, the illumination beam is tilted and translated along the X and Y axis while the decorrelation times $\tau_{i,x}$ and $\tau_{i,y}$ are measured successively to determine the displacements along the X and Y directions according to Eq. (22) as it is demonstrated in Figure 23. At the same time, the variance of the fluctuations of the integrated intensity $\sigma_i^2$ is recorded to provide the information about the motion along the Z direction. In this way, the entire 3D target trajectory can be recovered in real time. The motion of the target is approximated by a discrete, piecewise continuous trajectory in which each step is associated with one measurement. The duration of each measurement was 1 sec.

Any increase or decrease in any of the measured parameters corresponds to movement along the corresponding direction. If the target moves with constant speed, the trajectory can easily be

evaluated based on known time intervals between measurements, and the fact that the three measurable quantities $(\tau_{i,x}, \tau_{i,y}, \sigma_i^2)$ depend linearly on the target incremental displacements $(\Delta x, \Delta y, \Delta z)$ between successive measurements. Consequently, the motion along each direction can be represented as

$$\rho = a_\rho \xi + b_\rho \tag{24}$$

where $\rho \in \{\Delta x, \Delta y, \Delta z\}$ indicates the incremental motion along each axis and $\xi \in \{\tau_{i,x}, \tau_{i,y}, \sigma_z^2\}$ represents the measured parameters associated with that axis. The constants $a_\rho$ and $b_\rho$ are defined by the linear relations established in Eqs. (12-23) for each axis, independently of time and target motion. Note that these constants are not actually needed if only the relative incremental motion

$$\Delta\rho_m/\Delta\rho_1 = \Delta\xi_m/\Delta\xi_1 \tag{25}$$

is of interest. In Eq. (25), $m$ is the index of the piecewise continuous step of the motion and $m = 1$ represents the first motion step. Equations (24) and (25) are discussed in detail in the Appendix D. According to Eq. (25), a scaled trajectory can be easily recovered without any *a priori* calibration. A typical example of such recovery is illustrated in Figure 25.

To obtain the absolute trajectory of the target, two pieces of information are required. First, one would need to know the location of the target at the beginning of the tracking procedure. This would permit placing the 3D trajectory at the right position in the system of coordinates of the measurement. Second, one needs to know the coefficients $\{a_\rho, b_\rho\}$ in Eq. (24). As these coefficients are constant throughout the tracking procedure, one has to find two unknown constants for each axis. For this purpose, an *a priori* calibration based on Eq. (24) can be used where two sets of $\{\tau_{i,x}, \tau_{i,y}, \sigma_z^2\}$ are measured for two prescribed displacements of the target. A typical result is illustrated in Figure 26 where the target is moved over a 3D trajectory roughly included in

volume of 20 cubic millimeters. The experimental conditions of illumination and detection are the same as in the different example shown in Figure 25.

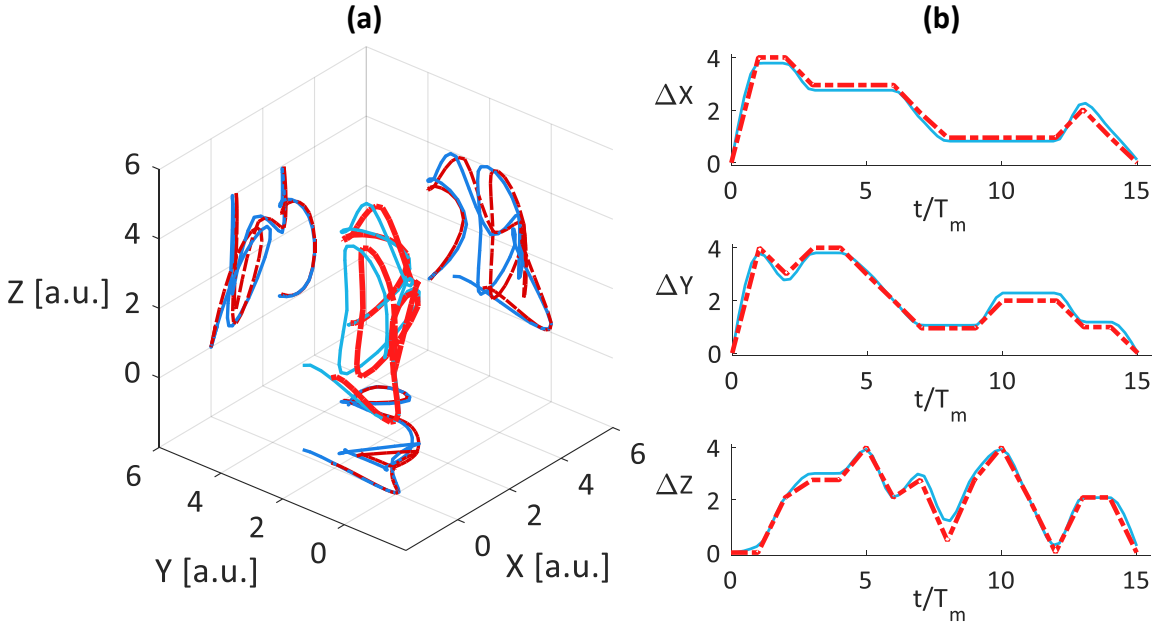


Figure 25 (a) Experimental demonstration of 3D tracking: the blue line represents the imposed target displacement while the red dashed line indicates the reconstructed trajectory. (b) One-dimensional representations of the imposed and recovered trajectories shown in (a), where $T_m$ denotes one measurement duration. The solid blue line denotes the exact trajectory while the dashed red line indicates the reconstructed trajectory.

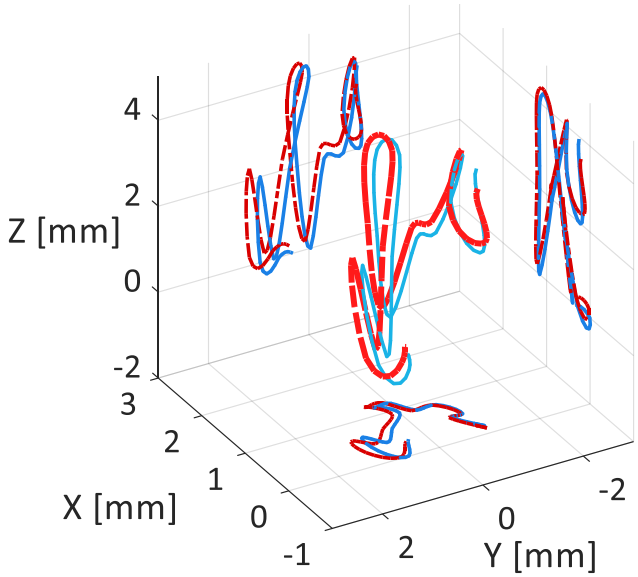


Figure 26 Experimental demonstration of 3D tracking using a priori calibration to extract the constants in Eq. (24). The blue line represents the imposed target displacement, while the red dashed line indicates the reconstructed trajectory.

Although recovering target trajectory with or without *a priori* information follows the same rule, i.e. Eq. (24), there is an important difference between two methods in terms of accuracy.

**Errors in Trajectory Reconstruction**

Let us now discuss the possible errors that can be encountered in this tracking procedure. Of course, due to the limited size of the ensemble of field realizations, one can anticipate deviations from one measurement to another. It is important to realize that while the errors in recovering the incremental motion steps do not depend on the starting point, they may accumulate over time. In practice, the experiment can be affected by possible fluctuations in the laser power, by noisy photon registrations at the detector, by a non-uniform velocity of the moving speckles, etc. As a consequence, the trajectory will be reconstructed with a precision that varies from point to point. The recovery error $\varepsilon$ can be defined as the difference between the exact and the estimated location of the target, relative to the average step size $\langle \Delta r \rangle$. The evolution of this error in recovering a scaled trajectory is illustrated in Figure 27. As is apparent from this figure, the errors in recovering the incremental target motion according to Eq. (25) do not accumulate, which can be advantageous for certain applications.

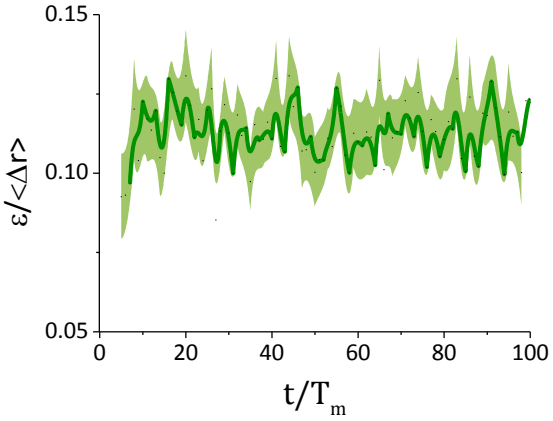


Figure 27 Evolution of the relative error $\varepsilon/\langle \Delta r$ during the tracking procedure. The error in reconstructing the target location is evaluated as $\varepsilon^2(t) = \varepsilon_x^2(t) + \varepsilon_y^2(t) + \varepsilon_z^2(t)$, and $\langle \Delta r \rangle$ denotes the average step size in moving the target. The solid line and the shaded area indicate the average and the standard deviation of the error over one hundred trajectories.

When using *a priori* calibration as described before, increasing the range of available data will improve the precision of evaluating the coefficients in Eq. (24). However, as opposed to the reconstruction of the scaled trajectory, in this case the average error depends on both constants in Eq. (24). As a result, the average reconstruction error accumulates along the trajectory, even though error in measuring the statistical parameters $\{\tau_{i,x}, \tau_{i,y}, \sigma_i^2\}$ may either increase or decrease from one step to another. This evolution is illustrated in Figure 28 for one hundred target trajectories developed over the same volume as in Figure 26. Of course, because of this error accumulation, which is specific to any sequential measurement without continuous feedback or reference, one may need, at some point, to go through a recalibration process. However, if knowledge about a scaled trajectory suffices, then the tracking precision is constant along the entire trajectory as is the case in Figure 27.

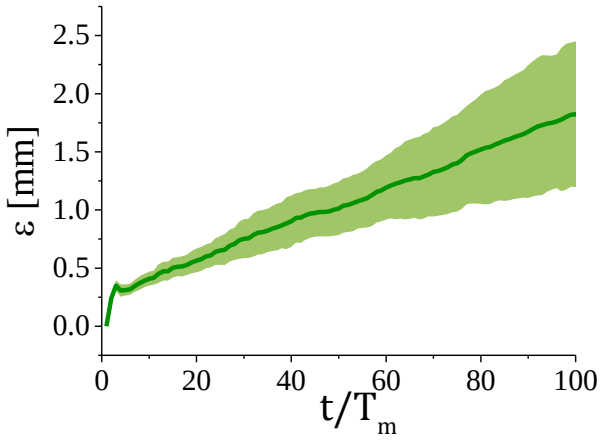


Figure 28 Error evolution in recovering an absolute trajectory. The time variable is normalized by the measurement time $T_m$. The error in reconstructing the target location is evaluated as $\varepsilon^2(t) = \varepsilon_x^2(t) + \varepsilon_y^2(t) + \varepsilon_z^2(t)$. Solid line and the shaded area show the average and the standard deviation of errors over one hundred trajectories, respectively.

## Further discussion

Although the present experiments involved a static scattering enclosure, this is not an absolute restriction. The tracking method works as long as the characteristic time of the controlled variation of the speckle field, $\tau_{sp}$, the characteristic time of the target dynamics $\tau_t$, and the

characteristic time associated with changes in the properties of the scattering wall, $\tau_w$, satisfy $\tau_{sp} < \tau_t < \tau_w$. Practically, the scattering enclosure can change as long as its dynamics are slower than that of the target. In this context, we also note that the speckle field generated inside the enclosure is quite sensitive to changes in the primary beam size, structure, and the angle of incidence, which permits manipulating the speckles' dynamics over large dynamic ranges.

Besides precision, the repeatability is another important characteristic of a measurement. Of course, the repeatability is primarily affected by dynamic perturbations while fluctuations originating in statistically independent sources of noise have a lesser effect.

We would like to emphasize that the tracking task can be achieved based on intensity measurements performed on any side of the scattering box. Even though, on average, the integrated intensity could differ on different sides of the box, our statistical approach is capable of extracting the same dynamic information. In this case, magnitude of the fluctuations may increase or decrease depending on angular distribution of the light scattering from the object as also discussed in the context of Eq. (19).

In deriving Eqs. (18-23), we considered that the evolution of the scattering potential is described by a single velocity vector. However, the same concept can be applied when the scattering potential is approximated by a collection of discrete objects with independent velocity vectors. In other words, the proposed tracking method can be generalized for tracking more than one object. To do so, one can use the independent component analysis [146, 147] of the integrated intensity fluctuations to separate independent sources of fluctuations associated with each independent motion. This, of course, will come at the cost of increasing the measurement time and decreasing the level of detectable fluctuations, which, in turn, could affect the tracking errors.

Practically, the magnitude of the intensity fluctuations can be affected in different ways. First, when approximating the potential with a collection of discrete objects, the variation associated with each independent component reduces roughly by a factor of $1/\sqrt{n_o}$ where $n_o$ is number of discrete objects. Second, the fluctuations are strongly affected by the target dimension $D$, the target feature size $l_t$, the size of the field of view $L$, and, of course, by the speckle size $l$. Although the size of target features does not provide sufficient information by itself, the ratio $l_t/l$ is an important factor. Choosing an optimum primary beam size $d_0$ helps keeping this ratio close to unity, which, according to Eq. (23), causes enhanced fluctuations. This is also demonstrated in Figure 24. In addition, the ratio between the target size and the size of the field of view, $D/L$, indicates how efficiently the target motion can modify the integrated intensity. As this factor grows, the contribution of the target motion to the dynamics of the integrated intensity increases and the accuracy of the tracking procedure improves.

Measurements are always affected by noise. Technically, the finite length of the time series of the recorded intensities introduces deviations from the ideal statistical parameters. Such deviations can, of course, be reduced by increasing the measurement time. Roughly speaking, the variance of the unwanted fluctuations can be decreased by a factor of $1/\sqrt{T_m}$, where $T_m$ is the measurement time in each step.

## Conclusions

We have demonstrated the ability to track the motion of a target completely surrounded and obscured by multiple scattering media. The concept of encoding the position of the target using statistical properties of diffused radiation is rather general as there are no restrictions on the scattering properties of the target. The statistical analysis of the recorded signal renders robust information that is free of interferences from the inherent experimental perturbations. Furthermore,

the method requires only measurements of the intensity integrated over large areas, which can be performed at any location outside the scattering enclosure. This feature, together with the experimental simplicity and versatility, is especially appealing for low-signal applications. In addition, because the movement along each direction is extracted independently, the approach is quite efficient in sensing scenarios involving different degrees of freedom.

We have shown that the motion and a relative trajectory of an enclosed target can be detected without any feedback from the inside of the obscured region. However, having access to limited *a priori* knowledge, the procedure can also provide quantitative measurements of the trajectory.

Finally, in our experiments we addressed the intriguing situation of detecting and tracking motion inside an obscuring box. However, the concept of using statistical properties of radiation to encode the position of scattering objects can be applied to other obscurant geometries, not necessarily flat, and also to different other detection scenarios. Moreover, as this method follows the motion of the target's center of mass, rotation and tilt of the object will not affect the tracking accuracy. These characteristics should be of interest for a range of applications including biomedical and remote sensing. Even though we presented optical experiments, this tracking procedure can also be implemented in other domains such as acoustics and microwaves.

# CHAPTER FOUR: REDUCING INTENSITY FLUCTUATIONS IN COHERENT IMAGING

## Coherent Noise

In the last two chapters we have approached optical sensing and imaging scenarios through exploiting imposed or naturally available optical fluctuations. Although harnessed fluctuations can be a very powerful optical probe, unwanted optical field variations can be quite bothersome in some cases. In general, one can call unwanted optical fluctuations as "noise" that can come in different flavors. Basically, the optical noise can be decomposed into the noise sources that are coherent and incoherent with the signal. The latter one cover noises that are generated by incoherent light sources and the perturbations that are imposed through coherent interaction under certain circumstances. In this case, the measured intensity will simply be the addition of the "signal" field and the "noisy" field intensities. However, when the noise is coherent with the signal, the interaction between signal and noise will contribute to the total intensity as well.

As an example, stray light in white light microscopy is a typical noise generated by an incoherent light source. Furthermore, one could also mention the speckle noise generated in OCT imaging, through reflection of low coherence beam of light from two layers of a tissue, separated by more than half of the light source coherence length, as another example of incoherent noise.

Coherent noise appears when the other scattering object in the neighborhood of the object of the interest are within coherence length of the light source. For instance in some cases in which light source with very long coherence length, for better control on spatial/angular distribution of the probe light, are needed to probe the remote objects [148], physically far distance objects can contribute in generating coherent noises. As an another example, sensing or imaging an object behind or in between scattering media, e.g. a flying object behind clouds, usually come with coherent noise.

As opposed to the incoherent noise, coherent perturbation interacts with the signal field, consequently, it can change the content of the detected field intensity which can be a serious issue. However, as we will show in the rest of this chapter, one can take advantage of the intrinsic properties of the spatially partially coherent fields to decreases coherent noises [149-151].

## Coherent Noise Reduction

### Introduction

Measurements are always affected by noise. When the noise is incoherent, it can be easily filtered out. However, acquiring information with coherent optical systems is more challenging because in this case the coherent noise not only can mask the information but it can also change the signal content [14, 15, 152]. This is a critical problem for "active sensing" where highly coherent sources are usually used to ensure the necessary directionality. In a generic scenario, a coherent probe beam interacts remotely with an object and the scattered field is analyzed to recover information about the targeted scattering potential [16, 17, 33, 153, 154]. An important consequence of this process is the unavoidable coherent noise, which is sometimes called the speckle artifact [152].

This coherent perturbation manifests differently depending on the characteristic length scale of the underlying process generating the artifact. For instance, when there are only mild perturbations over scales larger than the ones of interest, the problem can be addressed using approaches specific to adaptive optics. Canceling these disturbances may require feedback and multiple measurements with increasing complexity [16, 154], [13].

The coherent noise however can be even more severe [14, 15, 152]. The occurrence of stochastic interference, i.e. speckle noise, is a more complicated phenomenon involving multiple scattering of the coherent radiation [152]. The conventional approach to mitigate speckle noise is to make it

incoherent by averaging over different speckle realizations [152]. It was shown that spatial compounding reduces the speckle contrast but only by sacrificing the spatial response of the optical system [15, 155]. Alternatively, an effective averaging can be implemented through temporal frequency compounding, which, however, has its own shortcomings [15, 156]. Of course, averaging can be performed not only by recording different realizations of the scattered field but also by controlling the properties of the light source. A random laser, for instance, [157, 158] uses different spatial radiation modes to reduce speckle artifacts contrast at the cost of increasing the emission bandwidth and sacrificing the temporal coherence [157, 158]. All these conventional approaches for reducing the speckle contrast require multiple measurements comprising independent realizations of the coherent noise, which are produced by variations in the scattering system or by modifications in the characteristics of the light source. Although these methods are effective in reducing the speckle contrast, none of them operates efficiently in regimes of low signal to noise ratio (SNR).

Here we propose a new method for separating an optical signal immersed in a stochastic coherent noise. Our approach exploits an interferometric spatial heterodyne detection to separate the spectral components of the signal and the noise followed by a computational reconstruction of the targeted signal. As opposed to the temporal heterodyne detection, we will show that this method requires only single-shot measurements and it operates in very low SNR conditions.

## Heterodyne detection and analysis

Let us consider two mutually coherent fields that may have different spatial coherence properties [159]. We denote the field embedding the desired information (the signal) by $\mathcal{E}_1(\boldsymbol{\rho}, t)$ and the unwanted speckle noise by $\mathcal{E}_2(\boldsymbol{\rho}, t)$. Of course, their superposition will lead to strong spatial

modulation of the intensity. Without loss of generality, we will consider that the fields do not vary in time during a single-shot measurement.

As these two fields are considered to be statistically independent and stationary, at least in the wide sense, their superposition $\mathcal{E}_t(\boldsymbol{\rho}) = \mathcal{E}_1(\boldsymbol{\rho}) + \mathcal{E}_2(\boldsymbol{\rho})$ can be fully characterized through its cross-correlation function $\Gamma_t(\boldsymbol{\rho}_1, \boldsymbol{\rho}_2) = \langle \mathcal{E}_t^*(\boldsymbol{\rho}_1)\mathcal{E}_t(\boldsymbol{\rho}_2)\rangle$ where $\langle \cdots \rangle$ denotes the average taken over the field realizations. The spatial coherence properties of each field is governed by the corresponding complex degree of spatial coherence defined as $\mu_i(\boldsymbol{\rho}_2 - \boldsymbol{\rho}_1) = \Gamma_i(\boldsymbol{\rho}_1, \boldsymbol{\rho}_2)/\sqrt{\Gamma_i(\boldsymbol{\rho}_1, \boldsymbol{\rho}_1)\Gamma_i(\boldsymbol{\rho}_2, \boldsymbol{\rho}_2)}$ with $i = 1,2$. We consider the practical case in which the extent of $\mu_1(\Delta\boldsymbol{\rho})$ and $\mu_2(\Delta\boldsymbol{\rho})$, i.e. the spatial correlation lengths $l_1$ and $l_2$, are such that $l_1 \gg l_2$. In other words, the desired information $\mathrm{I}_1(\boldsymbol{\rho}) = \Gamma_1(\boldsymbol{\rho}, \boldsymbol{\rho})$ varies spatially much slower than the noise. The classical solution to this problem is filtering in the Fourier domain using a low pass filter that reduces the noise power [14]. However, in low SNR situations, this filtering procedure is not sufficient as we will show later.

Our method relies on the dissimilar statistical nature of the phase distributions in the two fields $\mathcal{E}_1$ and $\mathcal{E}_2$. We will take advantage of this difference without having to actually measure the phase distribution. Instead, we will exploit the information included in the spatial intensity variations created by superposing the total field $\mathcal{E}_t(\boldsymbol{\rho})$ with its shifted replica $\mathcal{E}_t(\boldsymbol{\rho} - \boldsymbol{\delta})$. The cross-correlation of this superposition leads to a spatial distribution of intensity

$$\mathrm{I}_s(\boldsymbol{\rho}) = \left\langle \left(\mathcal{E}_t(\boldsymbol{\rho}) + \mathcal{E}_t(\boldsymbol{\rho} - \boldsymbol{\delta})\right)^* \left(\mathcal{E}_t(\boldsymbol{\rho}) + \mathcal{E}_t(\boldsymbol{\rho} - \boldsymbol{\delta})\right)\right\rangle = \Gamma_t(\boldsymbol{\rho}, \boldsymbol{\rho}) + \Gamma_t(\boldsymbol{\rho} - \boldsymbol{\delta}, \boldsymbol{\rho} - \boldsymbol{\delta}) + 2\mathcal{R}e\{\Gamma_t(\boldsymbol{\rho}, \boldsymbol{\rho} - \boldsymbol{\delta})\}, \quad (26)$$

where $\mathcal{R}e\{\cdot\}$ denotes the real part. As can be seen, the first two terms represent the intensities at locations $\boldsymbol{\rho}$ and $\boldsymbol{\rho} - \boldsymbol{\delta}$ while the third one carries the mutual information about the field at these two separate locations. The mutual term in Eq. (26) can be expressed as

$$\mathcal{R}e\{\Gamma_t(\boldsymbol{\rho},\boldsymbol{\rho}-\boldsymbol{\delta})\} = \mathcal{R}e\{\Gamma_2(\boldsymbol{\rho},\boldsymbol{\rho}-\boldsymbol{\delta}) + \Gamma_1(\boldsymbol{\rho},\boldsymbol{\rho}-\boldsymbol{\delta})\} + \mathcal{R}e\{\Gamma_{12}(\boldsymbol{\rho},\boldsymbol{\rho}-\boldsymbol{\delta}) + \Gamma_{21}(\boldsymbol{\rho},\boldsymbol{\rho}-\boldsymbol{\delta})\} \quad (27)$$

When $|\boldsymbol{\delta}| \ll l_2 \ll l_1$, all the terms in right hand side of Eq. (27) are nonzero. However, as $|\boldsymbol{\delta}|$ gets larger such that $l_2 < |\boldsymbol{\delta}| \ll l_1$, the phase variation in $\mathcal{E}_2^*(\boldsymbol{\rho})\mathcal{E}_2(\boldsymbol{\rho}-\boldsymbol{\delta})$ increases and the first term $\Gamma_2(\boldsymbol{\rho},\boldsymbol{\rho}-\boldsymbol{\delta})$ vanishes. The local phase variation does not affect significantly the second term which can be approximated as

$$\mathcal{R}e\{\Gamma_1(\boldsymbol{\rho},\boldsymbol{\rho}-\boldsymbol{\delta})\} \approx I(\boldsymbol{\rho})\mu_1(\boldsymbol{\delta})\cos(\boldsymbol{k}_0(\boldsymbol{\delta}).\boldsymbol{\rho}), \quad (28)$$

where $\boldsymbol{k}_0(\boldsymbol{\delta})$ represents the spatial frequency associated with the intensity variation. Combining Eqs. (26-28), the spatial distribution of the detected intensity becomes

$$I_s(\boldsymbol{\rho}) \approx I_t(\boldsymbol{\rho}) + I_t(\boldsymbol{\rho}-\boldsymbol{\delta}) + 2\mathcal{R}\{\Gamma_{12}(\boldsymbol{\rho},\boldsymbol{\rho}-\boldsymbol{\delta}) + \Gamma_{21}(\boldsymbol{\rho},\boldsymbol{\rho}-\boldsymbol{\delta})\} + I_1(\boldsymbol{\rho})\mu_1(\boldsymbol{\delta})\cos(\boldsymbol{k}_0(\boldsymbol{\delta}).\boldsymbol{\rho}). \quad (29)$$

The first and the second term in Eq. (29) are not spatially modulation due to the absence of geometrical shift in $I_t(\boldsymbol{\rho}) = \Gamma_1(\boldsymbol{\rho},\boldsymbol{\rho})$ and $I_t(\boldsymbol{\rho}-\boldsymbol{\delta})$. Furthermore, the statistical independence of $\mathcal{E}_1$ and $\mathcal{E}_2$ and random phase variation of $\mathcal{E}_2$, results in random phase distribution in $\Gamma_{12}(\boldsymbol{\rho},\boldsymbol{\rho}-\boldsymbol{\delta})$ and $\Gamma_{21}(\boldsymbol{\rho},\boldsymbol{\rho}-\boldsymbol{\delta})$ that eliminates overall intensity modulation in the third term [159]. However, the well-defined spatial variation imposed to the last term changes the spectral content of the intensity distribution as schematically depicted in Figure 29.

The spectral representation of $I_t(\boldsymbol{\rho}) = \langle\mathcal{E}_t^*(\boldsymbol{\rho})\mathcal{E}_t(\boldsymbol{\rho})\rangle$ has two components originating from the desired intensity distribution and speckle noise, respectively. However, as it is suggested in Figure 29(b), superposing the total filed with a controllably shifted version of itself results in translating the intensity information by $\pm\boldsymbol{k}_0$ towards higher frequencies. This information can then be filtered using a band pass filter with central frequencies of $\pm\boldsymbol{k}_0$ to obtain the final intensity

$$I_f(\boldsymbol{\rho}) = \mathcal{D}\{I_s(\boldsymbol{\rho}) * f_{bp}(\boldsymbol{\rho};\pm\boldsymbol{k}_0,\Delta\boldsymbol{k})\}, \quad (30)$$

where $*$ denotes convolution and $f_{bp}(\boldsymbol{\rho}; \pm\boldsymbol{k}_0, \Delta\boldsymbol{k})$ is a band pass filter of bandwidth of $\Delta\mathbf{k}$. The operator $\mathcal{D}$ stands for demodulation with which central frequency of the information shifts back to zero. As a result, $I_f(\boldsymbol{\rho})$ will be desired intensity distribution.

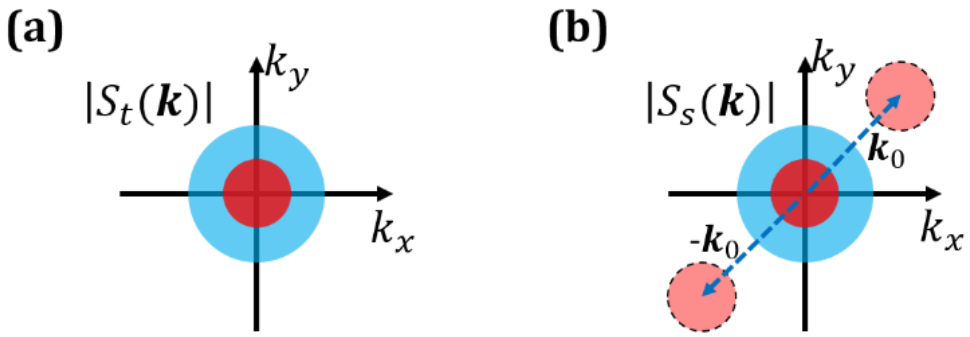


Figure 29 Spatial frequency representation of signal and noise intensities (a) the total field and (b) the spatially heterodyned field described by Eq. (29). Blue denotes the speckle noise while the red represents the frequency content of the signal. The red shaded areas in (b) represent the two signal replicas shifted towards higher spatial frequencies.

Coherent noise reduction demonstrations

A numerical proof of concept demonstration of the signal separation from the coherent noise is presented Figure 30. The efficacy is examined in the context of different levels of $SNR = \int I_1(\boldsymbol{r})d\boldsymbol{r} / \int I_2(\boldsymbol{r})d\boldsymbol{r}$. The performance is also compared with the results obtained by spatial low-pass filtering applied directly to the image corrupted by coherent noise.

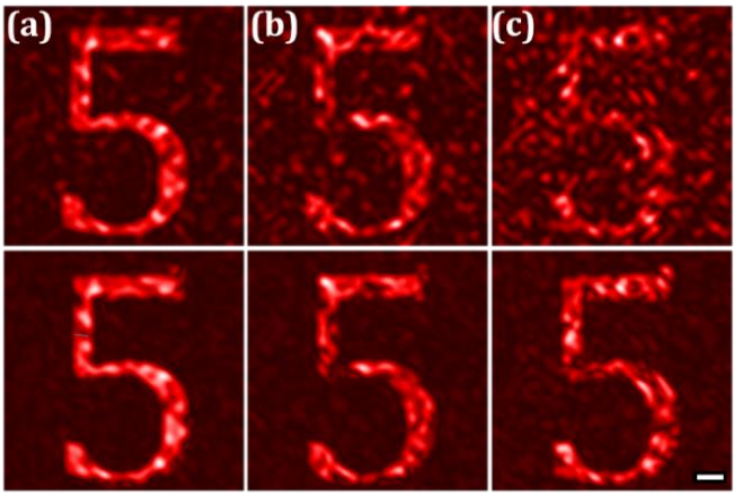


Figure 30 Numerical demonstration of reducing the speckle noise for a scene with 0.75 intensity contrast and for (a) SNR=2.5, (b) SNR=1, and (c) SNR=0.5. First row illustrates the results of direct spatial filtering and second row those obtained using the proposed heterodyne detection. The scale bar is 50 pixels.

As seen in Figure 30, when the SNR is high the spatial filtering suppresses efficiently the speckle artifacts. In low SNR regime however, this approach is not sufficient because the filter also passes strong speckle contributions. The spatial heterodyning on the other hand, provides a good speckle reduction even at very low SNR, as clearly seen in Figure 30(c). Nevertheless, in both methods, a certain amount of spatial filtering is unavoidable, which reduces the effective numerical aperture of the system and, therefore, affects in certain degree the final resolution. In this simulation, the intensity distributions are calculated over a normalized area of 640×640 pixels, with a supporting range -160<$k_x$,$k_y$<160 of normalized spatial frequencies. The bandwidth of the spatial filter was set to match the -5dB level of the signal bandwidth.

We note that, in addition to the level of noise power, the intrinsic intensity distribution contrast is a critical factor for the desired intensity reconstruction. Using the same numerical procedure as before, we conducted a systematic comparison between the direct spatial filtering and the proposed spatial heterodyning method, over a large parameter space of both SNR and target contrast. We assessed quantitatively the performance by measuring the similarity of the computed intensity distribution and the ideal one using Pearson correlation coefficient:

$$r = \frac{\int \tilde{I}_i(\boldsymbol{\rho})\tilde{I}_c(\boldsymbol{\rho})d\boldsymbol{\rho}}{\left(\int \tilde{I}_i^2(\boldsymbol{\rho})d\boldsymbol{\rho}\right)^{1/2}\left(\int \tilde{I}_c^2(\boldsymbol{\rho})d\boldsymbol{\rho}\right)^{1/2}}, \tag{31}$$

where $\tilde{I}(\boldsymbol{\rho}) = I(\boldsymbol{\rho}) - \int I(\boldsymbol{\rho}')d\boldsymbol{\rho}'$ represents the spatial intensity fluctuations, and $I_i(\boldsymbol{\rho})$ and $I_c(\boldsymbol{\rho})$ are the ideal and the computed intensity distribution, respectively. As it is shown in Figure 31, the spatial heterodyning approach makes the recovery process more robust in conditions of high power noise and low target contrast. This is consistent with the results presented in Figure 30.

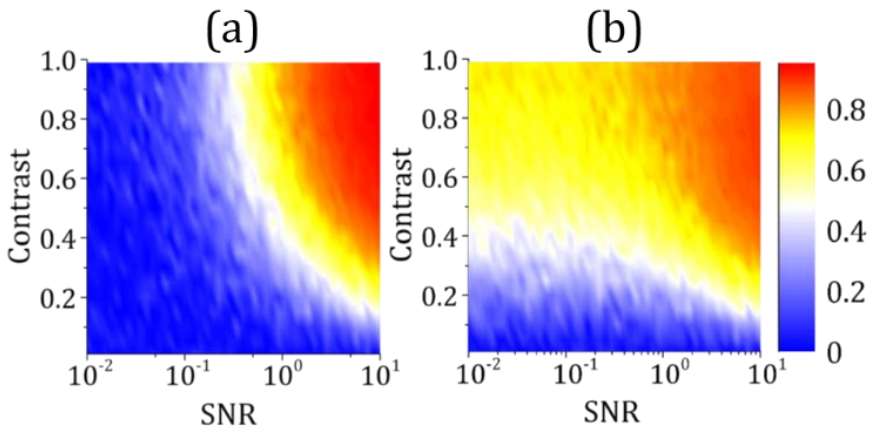


Figure 31 Pearson correlation coefficient between the ideal intensity distribution and the intensity recovered using (a) spatial filtering and (b) interferometric heterodyne detection.

Basically, for a given SNR, a decrease in the target contrast has a different effect on the high- and low-frequency components of the signal. With respect to the average noise level, the high-frequency components appear weaker making them indistinguishable from the noise. However, as illustrated in Figure 31, the spatial heterodyning keeps these vulnerable spectral frequency components far from the noise distribution, which, in turn, leads to less sensitivity to changes in the contrast.

Technically, the proposed method can be understood as a modification to a classical coherent imaging systems as illustrated in Figure 32. In the high SNR regime, the desired information can, of course, be directly detected. However, this is not the case in low SNR condition, in which the signal is significantly altered and cannot be easily separated from the noise. The proposed noise suppression approach is conceptually depicted in Figure 32(b), It amounts to an optical preprocessing step implemented by spatial heterodyning followed, after detection, by a post-processing step in which a spatial filtering procedure is implemented computationally.

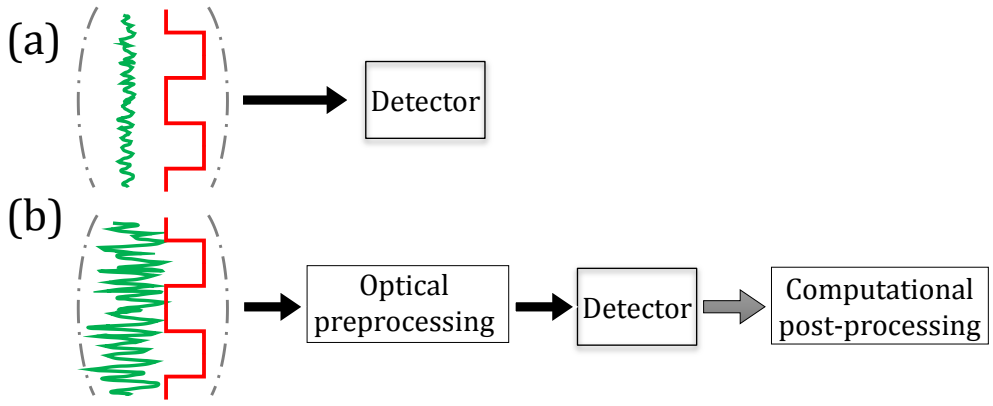


Figure 32 Schematic representation of a coherent imaging system. (a) In high SNR conditions the perturbed signal can be directly isolated. (b) In low SNR conditions, an efficient noise suppression requires spatial heterodyning (optical preprocessing) and filtering and demodulation after detection (computational post-processing).

The main idea behind separating the signal from the coherent noise is to implement the total field cross correlation with corresponding intensity given by Eq. (26). This operation of cross correlation can be implemented by different means. For instance, the separation of temporally narrow- and wide-band fields has been demonstrated by encoding two polarized replicas of the total field into two orthogonal states of the polarization [160]. In this scheme, the cross-correlation is effectively recovered by measuring the degree of polarization.

Here, we use an interferometer to produce two replicas of the input field and to impose a controllable spatial shift. We demonstrated this noise reduction method in an imaging scenario.

The schematic of the optical setup is shown in Figure 33. We have used a frequency double Nd:YAG laser with wavelength $\lambda = 532nm$ as the coherent light source. The intensity signal (red dashed line) is the image of a target T which is relayed onto the CCD camera. The speckle noise field (green dashed line) is generated by passing a part of the coherent light through a diffuser with optical thickness of $10l_s$ where $l_s$ is scattering mean free path. This speckle noise is then overlapped with the signal using a second beam splitter. The part of the setup surrounded by the gray dashed line creates the superposition of the signal and the coherent noise at various SNR levels adjusted by the neutral density filter ND. The Michelson interferometer is consisting of the

beam splitter $BS_3$ and the mirrors $M_3$ and $M_4$ constitutes the pre-processing unit depicted in Figure 33 surrounded by the black dashed line. This interferometer produces two coherent replicas of the total field, one of them being spatially shifted by $\boldsymbol{\delta}(\theta)$ where θ is the tilt angle of the mirror $M_3$. The difference between the propagation paths of the speckle field and the signal is also kept much smaller than the laser coherence length such that these fields can interfere.

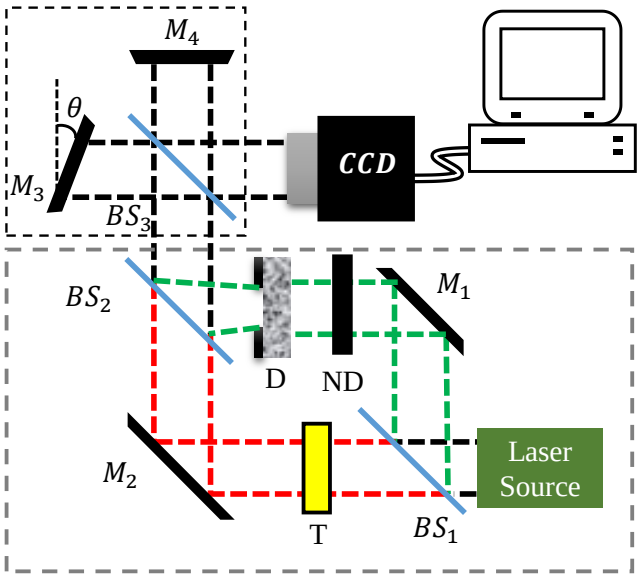


Figure 33 Schematic of the spatial heterodyne detection containing a signal-noise combiner to create a complex input field with adjustable SNR and a Michelson interferometer that implements the cross-correlation between the composite input field and a spatially shifted version of itself.

Technically, since $\mathcal{E}_1$ and $\mathcal{E}_2$ are temporally coherent, having noise generated in the second arm or in the same location as target, is equivalent. However, the geometry in Figure 33 provides control over SNR level for the purpose of demonstration. Moreover, title angle $\theta$ is constant throughout the measurement. In the extreme, having small title angle decrease frequency shift $\boldsymbol{k}_0$ (Figure 29(b)) which may make noise reduction less effective. Very high tilt angle though, may raise computational issue in conversion from spatial to frequency domain and vice versa, due to limited detector pixel size.

Figure 34 presents typical experimental results indicating their Pearson's coefficient of correlation with the noise free image obtained by blocking noise path (the green dashed line in Figure 33) and one of the Michelson interferometer arm. The first row depicts the perturbed intensity at different SNR levels as captured when one of the Michelson interferometer arm was blocked. Clearly, as the SNR decreases, the visibility of the target also decreases. The second row illustrates the result of filtering the coherent noise using a low pass filter in frequency domain. In the low SNR scenario, this filtering process leads in rather inefficient as clearly seen in the second and the third images in the second row.

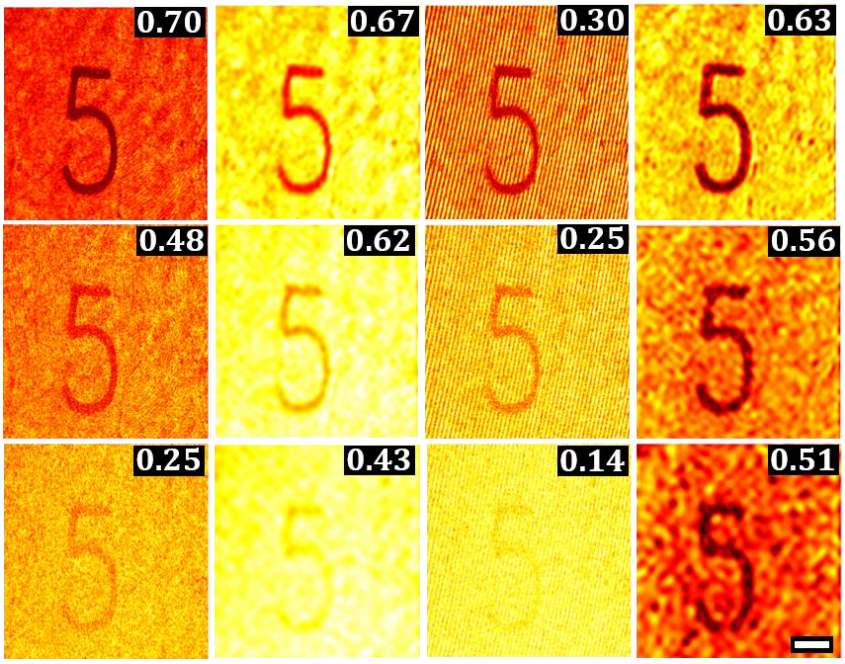


Figure 34 Experimental demonstration of speckle artifact reduction for (a) SNR=2.5, (b) SNR=1, and (c) SNR=0.5. The first row contains the total field intensity, the second one the reconstructed image through low pass spectral filtering, the third row is the detected spatially heterodyned field intensity, and the forth one the corresponding filtered and demodulated version of the intensities shown in the third row. The number in the upper right corner of each image denotes the corresponding Pearson's coefficient as described in the text. The scale bar is 20μm.

The results obtained by spatially heterodyning the coherent superposition of the total field with its shifted replica are illustrated in the third row. Again, the visibility of the modulated intensity reduces when the SNR decreases but it never vanishes as suggested by Eq. (29). However, using Eq. (30), one can always have the information filtered and demodulated numerically as illustrated

in the fourth row of Figure 34. Clearly, this approach makes the best recovery even at the lowest SNR as indicated by the corresponding Pearson correlation coefficient. Besides visibility, the non-uniform spatial distribution of the noise can also leak into the low pass filtered image shown in the second row. However, as this noise property belongs to the non-modulated low frequency intensity, it is filtered out after demodulating the frequency upshifted signal.

Obviously, this method comes with its own side effects. Band pass representation of the total intensity always come with contribution of coherent speckle noises. Consequently, collected speckle field contribution will result in some irregularity in the reconstructed image as it is clear in Figure 34, however, they can be rejected through post processing as if it is needed. Having targets with apodized edges though, would allow tighter band pass filtering and, consequently, would enhance the noise reduction efficiency.

## Conclusion

In conclusion, information immersed in high power coherent noise is not necessarily lost. Here we proposed and demonstrated an information recovery technique that relies on the fundamental properties of partial coherent fields. Using an interferometric heterodyne detection, we have showed that the corrupted information can be easily recovered in real time and without any prior knowledge about the information content. We have demonstrated the efficiency of this method for imaging targets with different contrasts while operating at low SNR levels.

The examples presented here addressed imaging static targets, which required only single-shot measurements. However, since this method does not require altering the conditions of illumination, it can be easily adapted monitoring the motion of dynamic objects in conditions of extremely low SNR.

Finally, even though the concept was demonstrated in the context of optical imaging, similar requirements for coherent denoising may occur in other geometries and in different frequency domains. This approach could be applied in any circumstances where coherent or partially coherent fields are affected by, for instance, scattering perturbations like in coherent remote sensing [161], ultra-sonic imaging [162], etc.

# CHAPTER FIVE: CONCLUSION AND REMARKS

Statistical phenomena are always present in light-matter interaction. Besides, practical setups for investigating these interactions usually impose additional randomness and make this condition even more complicated. Although stochastic variations can be sometimes overlooked, in some other cases they have significant impact either as the "signal" field or as the "noise".

Depending on the nature of the problem, statistical variations should be treated differently. More specifically, having fluctuations as noise, one may need to try suppressing its impact. On the other hand, if fluctuations play an informative role, one can try enhancing them to improve certain attributes of the procedure.

Informative fluctuations appear in optical characterization procedures in two different roles: as probes or as detected fields. When using fluctuations as a probe, one can exploit the available uncertainty in the procedure to investigate an interaction. However, stochastic probing is not limited to using the fluctuations imposed by inherent randomness of the system. For instance, one can add additional randomness to the procedure by using an active stochastic probing field. Regardless of being active or passive probes with either random or deterministic properties, fluctuations of the scattered field always carry information about the interaction. However, it is not always straightforward to extract this information. A possible way of making it viable is to utilize probe fields with specific statistical properties capable of encoding certain attributes of the interaction into the fluctuations of the scattered field. In other words, besides using the right probe, one can structure the probe to make acquisition of information more convenient and more robust to the perturbations.

In this thesis, we were concern with applications of the optical intensity fluctuations in the context of three different aspects of computational optical imaging and sensing. More specifically, we

studied situations where certain statistics are imposed to the light-matter interaction using structured illumination, we explored circumstances where inherent statistical properties of optical fluctuations are exploited in the sensing procedures, and finally, we presented a novel approach for reducing the unwanted intensity fluctuations in coherent imaging.

In chapter two, we developed three computational imaging and sensing methods in which imposing intensity fluctuations actually helps enhancing the overall efficiency. We have studied compressive active correlation imaging in low signal-to-noise ratio (SNR) regimes. In this situation, using structured intensity, e.g. Hadamard patterns, at each measurement, one samples target spatial representation at only one point of the corresponding representation, e.g. Hadamard domain. Consequently, data acquisition is prone to the noise. On other hand, using randomized binary intensity structures, one can sample the targeted structure at multiple points at each measurement. As a result, images can be reconstructed at low SNR levels and with high compression ratios.

The use of stochastic illumination probes is not limited to imaging applications. In the realm of computational sensing, we have introduced Stochastic Optical Sensing (SOS) and demonstrated that spatial information can be inferred using non-stationary stochastic illumination. We have shown that using randomly structured probe field intensity with varying correlation length, in conjunction with a statistical analysis of the integrated scattered light, one can recover characteristic length scales of a scattering potential without actually imaging it. We have examined this approach in highly perturbed and low-light condition for targets with different scattering properties and have also demonstrated that this statistical analysis has a unique capability in rejecting the inherent background noise.

Furthermore, we have discussed the sequential nature of stochastic optical sensing and have shown that the statistical information acquisition can be compressed by exploiting additional statistical encoding. Using common knowledge about realistic objects, i.e. limited spatial bandwidth, we introduced computational compressive Stochastic Optical Sensing (cSOS). Because the measurement parameters can be compressed regardless of the sparsity level of the targeted potential, the measurement time and the exposed energy density can be significantly reduced, which is of specific interest in time-lapse biomedical sensing applications. This method makes it possible to monitor live targets over an extended time while reducing the risk for phototoxicity.

In chapter three, we considered a case where tailoring the random probe by structuring the field intensity is not possible anymore due to the presence of the strong perturbations. In this case, we have shown that using the inherent properties of the randomly multiple scattered field, one can sense and measure certain dynamic information. This condition was demonstrated in the context of tracking an object that is completely obscured by multiple scattering media. We have shown that a statistical analysis of the measure intensity fluctuations anywhere outside of the scattering enclosure provides means for following the motion of the object.

The last topic examined in chapter four is concerned optical intensity fluctuations as a hindering element for imaging procedures. More specifically, we consider the case in which optical noisy fluctuations are coherent with the optical signal that is capable of changing the information content of the signal. We have shown that, by using intrinsic statistical properties of the partially coherent fields, one can reduce the coherent noise significantly through a computational analysis of the detected heterodyned field intensity. This method offers a significant reduction of the coherent noise with only minimal modifications of the imaging system.

In summary, we have shown that the statistical nature of the optical fluctuations can be manipulated and utilized to separate information from the noise. The results presented here demonstrate that stochastic optical fluctuations are not always noise and, furthermore, the information immersed in strong noise is not necessarily lost. As long as the statistical properties of the informative field intensity differ from the random noise fluctuations, one can develop optical imaging or sensing procedures even in highly perturbed conditions.

The methodologies developed in this thesis illustrate different circumstances where certain attribute of computational optical imaging and sensing can be enhanced by exploiting the statistics of the intensity fluctuations. Applications ranging from biomedical imaging to remote sensing could benefit from the sturdy performance of these statistical methods.

# APPENDIX A: CORRELATION IMAGING USING NONLINEAR IMAGE RECONSTRUCTION ALGORITHM

In chapter two, we have discussed linear image reconstruction algorithm in correlation imaging and we have compared different type of illumination structures. In principle, image reconstruction is not limited to the linear approaches. Of course, linear reconstruction is not the optimal solution. Nevertheless, it is an appealing approach when prior knowledge is not available. Having *a priori* information available, one can exploit it in the reconstruction procedure [118]. Furthermore, one can exploit available knowledge in a certain way to recover specific features of the target [83, 85]. For instance, having knowledge about sparsity of an image, one can exploit different variants of the compressive sensing image reconstruction algorithms to enhance quality of the recovered image.

Mathematically, one can present probe field intensity structure at each measurement in the form of a vector $a_j(\boldsymbol{\rho}) \in \mathbb{R}_+^{N\times 1}$, where subscript $j$ denotes measurement index, vector $\boldsymbol{\rho}$ indicate system of coordinates, and $\mathbb{R}_+$ demonstrate nonnegative real number space. In this case, integrated intensity can be modeled by

$$A \cdot R = I \tag{I.1}$$

where $R \in \mathbb{R}_+^{N\times 1}$ denotes targeted object representation and $A$ is measurement matrix, i.e. $A = [\, a_1\, a_2\, \cdots a_M]^T \in \mathbb{R}_+^{(M\times N)}$, where superscript $T$ denotes transpose and $\cdot$ indicates matrix multiplication. In principle, one can recover the image $R$ through inversion of Eq. (I.1), i.e. $R = (A^T A)^{-1} A^T I$. However, in practice inversion is prone to noise, if it is possible. Moreover, inversion does not engage the available prior knowledge in the image reconstruction algorithm. The available information can be integrated into the reconstruction algorithm through minimizing a regularized energy function

$$\epsilon(R) = \|A \cdot R - I\|_2 + \psi(R) \tag{I.2}$$

for $R \geq 0$ where, $\psi(R)$ denotes regularization function. For the binary targets investigated in chapter two, one can use total variant regularization function to reduce noisy variation in the recovered image. To examine this approach, we modeled the image reconstruction problem by

$$\epsilon(R) = \mu\|A \cdot R - I\|_2 + \int \left\|\nabla_{\boldsymbol{\rho}} R\right\|_2 d\boldsymbol{\rho} \tag{I.3}$$

where $\nabla_{\boldsymbol{\rho}} R$ indicate gradient vector of the image $R$ at position $\boldsymbol{\rho}$ and $\mu$ is regularization factor**.** Here we used TVAL3 optimization toolbox [163] to solve Eq. (I.3). Figure 35-36 demonstrate recovered image in simulated noisy condition characterized with SNR=10. We have examined image reconstruction at different compression ratio for different regularization coefficient. Using this approach, noisy background variation in the image can be reduced significantly; however, it comes at the cost of increased computationally complexity. Here to decrease computational load, we have decreased simulated image size to 64×64 pixels.

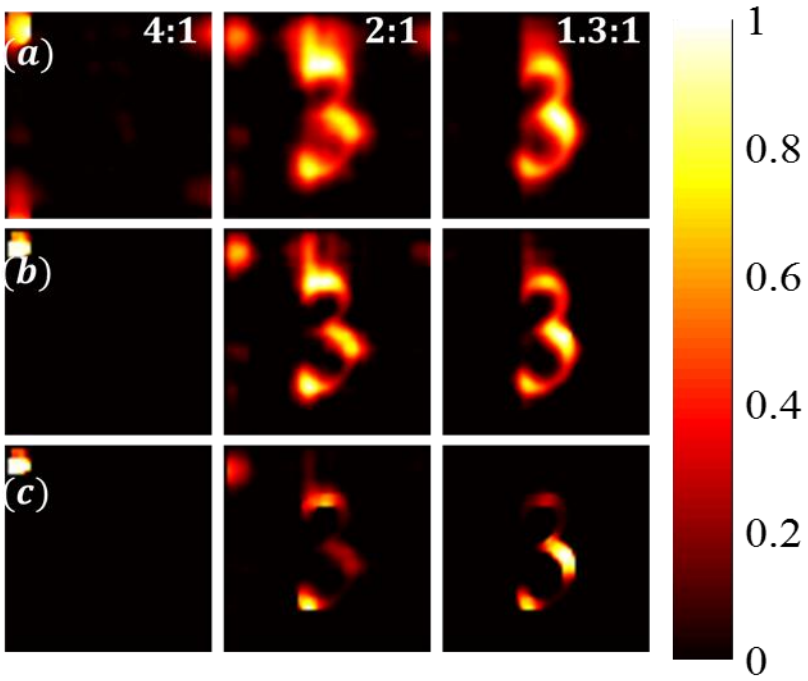


Figure 35 Recovered image using randomly selected Hadamard patterns. Each column shows recovered image for a given compression ratio. Different regularization coefficient is examined to investigate effect of this parameter on the reconstructed image. Here we examined (a) μ=50, (b) μ=150 and (c) μ=250.

As it is clear from Figure 35, at low compression ratio, illumination intensity structure randomly selected from the Hadamard pattern set fails in recovering an image, similar to the results shown in Figure 2. However, as compression ratio decreases image features become clearer. Figure 36 demonstrate recovered image of the same target using random dot illumination with spatial coverage of 5%. Second norm or each measurement row is normalized to model the same illumination power in both cases. As it is apparent, random dot outperform patterned illumination structure.

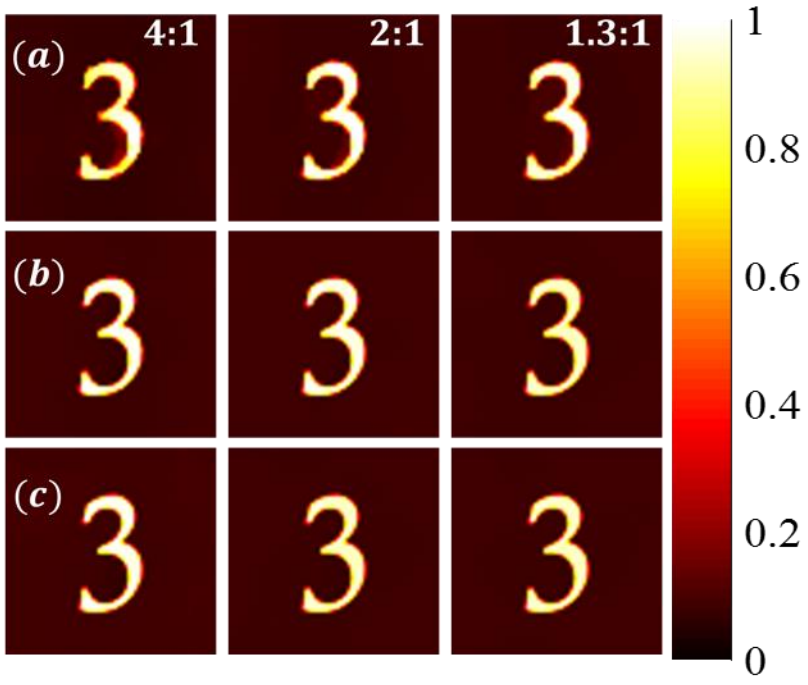


Figure 36 Recovered image using random dot illumination patterns. Each column shows recovered image for a given compression ratio. Different regularization coefficient is examined to investigate effect of this parameter on the reconstructed image. Here we examined (a) μ=50, (b) μ=150 and (c) μ=250.

Of course, using structured patterns, like Hadamard patterns in our case, reconstruction algorithm could be tailored to enhance the image reconstruction speed, especially at high compression ratio. Nevertheless, sensitivity of the recovered image to the regularization factor can limit its applicability in practical cases in which prior knowledge is not available. On the other hand, using random dot illumination, image reconstruction is less sensitive to the regularization factor.

However, using random dot illumination, reconstruction runtime does not change significantly as one increase or decrease compression ratio. It also worth mentioning that somewhat good performance of presented imaging method in high compression ratio depends on properties of the target, as expected. Decreasing contrast of the target or imaging an object with spatial variation of scattering coefficient can decrease quality of the image significantly.

# APPENDIX B: PROOFS AND DETAILS ON STOCHASTIC OPTICAL SENSING

## Propagation and Limited Size of Detector Effect

To simplify the exposure of main concept, the Eq. (5) in the text does not include the effect of propagation towards the detector. In this section we will show that average scattered intensity at axial distance $\zeta$ is equivalent to average scattered intensity right after the target. Consistent with the main text, we consider a targeted scattering potential with complex field scattering coefficient $\mathcal{P}(\boldsymbol{\rho})$ and intensity scattering coefficient of $T(\boldsymbol{\rho}) = |\mathcal{P}(\boldsymbol{\rho})|^2$. The illumination field at the target plane is shown with $\mathcal{E}_S(\boldsymbol{\rho}, 0)$ where the zero denotes hypothetical reference of axial direction on the target plane. . Considering a thin-layer scattering potential in which the transversal coordinate of entering and exiting point of each ray of light is the same, one can represent electric field distribution right after the target by $\mathcal{E}_S(\boldsymbol{\rho}, 0)\mathcal{P}(\boldsymbol{\rho})$. Having this said, under paraxial and quasi-monochromatic approximation, one can express Intensity distribution at detection plane using [140]

$$I(\boldsymbol{\rho}) = \frac{1}{\lambda^2}\iint \mathcal{P}(\boldsymbol{\rho}_1')\mathcal{P}^*(\boldsymbol{\rho}_2')\langle \mathcal{E}_S(\boldsymbol{\rho}_1', 0)\mathcal{E}_S^*(\boldsymbol{\rho}_2', 0)\rangle \mathcal{G}(\boldsymbol{\rho}, \boldsymbol{\rho}_1')\mathcal{G}^*(\boldsymbol{\rho}, \boldsymbol{\rho}_2')d^2\boldsymbol{\rho}_1' d^2\boldsymbol{\rho}_2' \qquad \text{(II.1)}$$

where $\mathcal{G}(\boldsymbol{\rho}, \boldsymbol{\rho}')$ is the scattering problem Green's function, $\langle\cdot\rangle$ indicates average taken over an ensemble, and $J_i(\boldsymbol{\rho}_1', \boldsymbol{\rho}_2') = \langle \mathcal{E}_S(\boldsymbol{\rho}_1', 0)\mathcal{E}_S^*(\boldsymbol{\rho}_2', 0)\rangle$ is illumination field mutual intensity. In the case of free space propagation between the target and the detection system, Eq. (II.1) can be simplified by

$$I(\boldsymbol{\rho}) = \frac{1}{\lambda^2\zeta^2}\iint \mathcal{P}(\boldsymbol{\rho}_1')\mathcal{P}^*(\boldsymbol{\rho}_2')J_i(\boldsymbol{\rho}_1', \boldsymbol{\rho}_2')e^{-j\frac{2\pi}{\lambda}(r_2 - r_1)}d^2\boldsymbol{\rho}_1' d^2\boldsymbol{\rho}_2' \qquad \text{(II.2)}$$

where $r_{1,2}^2 = \zeta^2 + \left|\boldsymbol{\rho}_{1,2}' - \boldsymbol{\rho}\right|^2$. Consequently, using

$$r_2 - r_1 \approx \frac{1}{2\zeta}\left(\boldsymbol{\rho}_2'^{\,2} - \boldsymbol{\rho}_1'^{\,2} - 2\boldsymbol{\rho}\cdot(\boldsymbol{\rho}_2' - \boldsymbol{\rho}_{\mathrm{a}}')\right), \qquad \text{(II.3)}$$

One could simplify Eq. (II.2) and represent it by

$$I(\boldsymbol{\rho}) = \frac{1}{\lambda^2\zeta^2}\iint \mathcal{P}(\boldsymbol{\rho}_1')\mathcal{P}^*(\boldsymbol{\rho}_2')J_i(\boldsymbol{\rho}_1', \boldsymbol{\rho}_2')e^{-j\frac{\pi}{\lambda\zeta}\left(\boldsymbol{\rho}_2'^{\,2} - \boldsymbol{\rho}_1'^{\,2}\right)}e^{-j\frac{2\pi}{\lambda\zeta}\left(\boldsymbol{\rho}\cdot(\boldsymbol{\rho}_2' - \boldsymbol{\rho}_{\mathrm{a}}')\right)}d^2\boldsymbol{\rho}_1' d^2\boldsymbol{\rho}_2'. \qquad \text{(II.4)}$$

Having scattered intensity spatial distribution, one can calculate integrated scattered intensity as

$$i = \int A(\boldsymbol{\rho}) I(\boldsymbol{\rho}) d^2\boldsymbol{\rho}, \tag{II.5}$$

where $A(\boldsymbol{\rho})$ is finite function that models the finite intensity integration area. By substituting Eq. (II.4) in Eq. (II.5), one can reformulate integrated intensity as function of illumination field and targeted potential through

$$i = \frac{1}{\lambda^2\zeta^2} \iint \mathcal{P}(\boldsymbol{\rho}'_1)\mathcal{P}^*(\boldsymbol{\rho}'_2) J_i(\boldsymbol{\rho}'_1, \boldsymbol{\rho}'_2) e^{-j\frac{\pi}{\lambda\zeta}\left(\boldsymbol{\rho}'^{\,2}_2 - \boldsymbol{\rho}'^{\,2}_1\right)} \left( \int A(\boldsymbol{\rho}) e^{-j\frac{2\pi}{\lambda\zeta}\left(\boldsymbol{\rho}\cdot(\boldsymbol{\rho}'_2 - \boldsymbol{\rho}'_{\mathrm{a}})\right)} d^2\boldsymbol{\rho} \right) d^2\boldsymbol{\rho}'_1 d^2\boldsymbol{\rho}'_2. \tag{II.6}$$

The inner integral in Eq. (II.6) is basically Fourier transform of the integration system aperture and can be presented as

$$\mathcal{A}\left(\frac{\boldsymbol{\rho}'_2 - \boldsymbol{\rho}'_{\mathrm{a}}}{\lambda\zeta}\right) = \int A(\boldsymbol{\rho}) e^{-j\frac{2\pi}{\lambda\zeta}\left(\boldsymbol{\rho}\cdot(\boldsymbol{\rho}'_2 - \boldsymbol{\rho}'_{\mathrm{a}})\right)} d^2\boldsymbol{\rho} \tag{II.7}$$

where $\mathcal{A}(\boldsymbol{f})$ is the Fourier transform of the aperture. Consequently, integrated intensity could be simplified to

$$i = \frac{1}{\lambda^2\zeta^2} \iint \mathcal{P}(\boldsymbol{\rho}'_1)\mathcal{P}^*(\boldsymbol{\rho}'_2) J_i(\boldsymbol{\rho}'_1, \boldsymbol{\rho}'_2) e^{-j\frac{\pi}{\lambda\zeta}\left(\boldsymbol{\rho}'^{\,2}_2 - \boldsymbol{\rho}'^{\,2}_1\right)} \mathcal{A}\left(\frac{\boldsymbol{\rho}'_2 - \boldsymbol{\rho}'_{\mathrm{a}}}{\lambda\zeta}\right) d^2\boldsymbol{\rho}'_1 d^2\boldsymbol{\rho}'_2. \tag{II.8}$$

Having a an aperture much larger than the coherence length of the illumination field, $\mathcal{A}\left(\frac{\boldsymbol{\rho}'_2 - \boldsymbol{\rho}'_{\mathrm{a}}}{\lambda\zeta}\right)$ would be much narrower than the $J_i(\boldsymbol{\rho}'_1, \boldsymbol{\rho}'_2)$, consequently, one can approximate Eq. (II.8) by asymptotic case of having infinite aperture which results in

$$i = \frac{1}{\lambda^2\zeta^2} \iint \mathcal{P}(\boldsymbol{\rho}'_1)\mathcal{P}^*(\boldsymbol{\rho}'_2) J_i(\boldsymbol{\rho}'_1, \boldsymbol{\rho}'_2) e^{-j\frac{\pi}{\lambda\zeta}\left(\boldsymbol{\rho}'^{\,2}_2 - \boldsymbol{\rho}'^{\,2}_1\right)} \delta\left(\frac{\boldsymbol{\rho}'_2 - \boldsymbol{\rho}'_{\mathrm{a}}}{\lambda\zeta}\right) d^2\boldsymbol{\rho}'_1 d^2\boldsymbol{\rho}'_2 \tag{II.9}$$

where $\delta(\boldsymbol{\rho})$ denotes Dirac's delta function. Using properties of the delta function, one can further simplify Eq. (II.9) and express integrated intensity as

$$i = \int |\mathcal{P}(\boldsymbol{\rho}')|^2 J_i(\boldsymbol{\rho}', \boldsymbol{\rho}') d^2\boldsymbol{\rho}' = \int T(\boldsymbol{\rho}') I_i(\boldsymbol{\rho}') d\boldsymbol{\rho}' \tag{II.10}$$

Where $I_i(\boldsymbol{\rho}')$ denote illumination field intensity, which is equivalent to the model of the sensing scenario shown in Eq. (5) in the main text. This formulation is based on the assumption of infinite size of integration window. Of course, if the detector size becomes too small the signal itself is lost as is the case with any other sensing approach relying on far-field measurements. However, as we rely on statistics of scattered light, limited detection window is not expected to affect the results significantly.

Here we consider the targets shown in Figure 7(a) and Figure 9(a) in chapter 2, which are a sparse, and a non-sparse target respectively. The SNR is 2dB to mimic a highly noisy condition with unity magnification between target and detector. To consider the effect of propagation we have used well known concept of point spread function (PSF) and 4 different Gaussian PSF with FWHM of ≈0.45Δ, 0.7Δ, 0.95Δ and 1.2Δ. Figure 37 presents the Fano factor spectra for different PSF. Figure 37 shows that the two peaks in the spectra remain distinguishable after propagation, when the detector size is kept constant. The Figure 37(b) illustrates that limited data collection does not affect the Fano factor spectrum even for a non-sparse target.

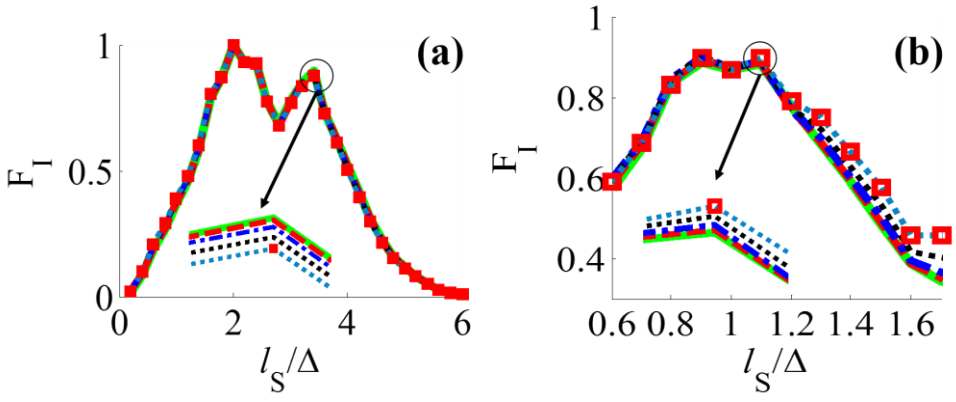


Figure 37 Effect of diffraction on characterizing scattering potential length scale without considering propagation ( –), and with Gaussian Green's function with FWHM of (--)0.45Δ, (-•-)0.7Δ, (••)0.95Δ, and (•□•)1.2Δ for target shown in Figure 7(a) and Figure 9 (a) in the text. Inset shows difference between different conditions around the second peak in the Fano spectrum.

As clearly seen, the propagation does not affect the results significantly. Propagation works as a perturbation out that does not affect statistical properties of the integrated scattered light intensity. This perturbation changes the spatial distribution of the light but preserves the energy and as a result, the statistics of the recorded intensity which characterize the intensities in different measurements (not at different locations) will not change. Of course, in these demonstration the area covered by light is increased by 25-70% for unity magnification and there is some loss of information about the target, which, however, does not affect the statistics.

## Reconstruction of Statistical Point Properties of The Targeted Potential

As it is discussed in the main text, in the case of δ-correlated illumination, one can reconstruct statistical moments of the scattering potential shown in Eq. (6) and (7). These statistical moments describe point properties of the targeted potential. Here in this section, we derive Eq. (6) and (7), from the sensing problem model Eq. (5)

$$i(\xi) = \int \big(I(\boldsymbol{\rho};\xi) + n(\boldsymbol{\rho};\xi)\big)P(\boldsymbol{\rho};\xi)T(\boldsymbol{\rho}) + R(\boldsymbol{\rho};\xi)d\boldsymbol{\rho} = \int \sigma(\boldsymbol{\rho};\xi)T(\boldsymbol{\rho}) + R(\boldsymbol{\rho})d\boldsymbol{\rho}, \qquad \text{(II.11)}$$

where $\sigma(\boldsymbol{\rho};\xi)$ is effective projection of perturbed illumination on the targeted scattering potential. Fluctuations of the intensity over its ensemble average is given by

$$\tilde{\imath}(\xi) = i(\xi) - \langle i(\xi)\rangle_\xi = \int \tilde{\sigma}(\boldsymbol{\rho};\xi)T(\boldsymbol{\rho}) + \tilde{R}(\boldsymbol{\rho})d\boldsymbol{\rho}. \qquad \text{(II.12)}$$

One can define k$^{th}$ order moment of the intensity fluctuations by

$$\widetilde{m}_i^{(k)} = \left\langle \left(\tilde{\imath}(\xi)\right)^k \right\rangle_\xi = \left\langle \left(\int \tilde{\sigma}(\boldsymbol{\rho};\xi)T(\boldsymbol{\rho}) + \tilde{R}(\boldsymbol{\rho})d\boldsymbol{\rho}\right)^k \right\rangle_\xi, \qquad \text{(II.13)}$$

that for the case of $\delta$-correlated illumination can be written as

$$\widetilde{m}_i^{(k)} = \left\langle \left(\tilde{\imath}(\xi)\right)^k \right\rangle_\xi = \left\langle \int \left(\tilde{\sigma}(\boldsymbol{\rho};\xi)T(\boldsymbol{\rho}) + \tilde{R}(\boldsymbol{\rho})\right)^k d\boldsymbol{\rho} \right\rangle_\xi =$$

$$\left\langle \int \sum_{n=0}^{k} \frac{k!}{n!(k-n)!} \tilde{\sigma}^n(\boldsymbol{\rho};\xi)T^n(\boldsymbol{\rho})\tilde{R}^{k-n}(\boldsymbol{\rho})\, d\boldsymbol{\rho} \right\rangle_\xi \qquad \text{(II.14)}$$

Considering each term in the summation in Eq. (II.14)

$$\left\langle \int \frac{k!}{n!(k-n)!} \tilde{\sigma}^n(\boldsymbol{\rho};\xi) T^n(\boldsymbol{\rho}) \tilde{R}^{k-n}(\boldsymbol{\rho}) d\boldsymbol{\rho} \right\rangle_\xi = \begin{cases} 0 & k-\ odd \\ nonzero & k-\ even \end{cases}. \tag{II.15}$$

As a result, one can simplify Eq. (II.14) and rewrite it as

$$\widetilde{m}_i^{(k)} = \sum_{n=0}^{k/2} \frac{k!}{2n!(k-2n)!} \widetilde{m}_\sigma^{(2n)} M_T^{(2n)} \widetilde{m}_R^{(k-2n)}. \tag{II.16}$$

By reformatting this summation, one can evaluate recursively the moments

$$M_T^{(k)} = \frac{\widetilde{m}_i^{(k)}}{\widetilde{m}_\sigma^{(k)}} - \sum_{n=0}^{(k-2)/2} \frac{k!\widetilde{m}_R^{(k-2n)}}{2n!(k-2n)!} \frac{\widetilde{m}_\sigma^{(2n)}}{\widetilde{m}_\sigma^{(k)}}\ M_T^{(2n)} \tag{II.17}$$

defining the spatial distribution of the scattering potential. In the practical case where $k = 2$, one can easily use Eq. (II.17) and (II.11) to calculate Fano factor associated with the targeted scattering potential

$$M_T^{(2)} = \frac{\widetilde{m}_i^{(2)}}{\widetilde{m}_\sigma^{(2)}} - \frac{\widetilde{m}_R^{(2)}}{\widetilde{m}_\sigma^{(2)}} \tag{II.18}$$

$$M_T^{(1)} = \frac{\langle i(\xi)\rangle_\xi - \langle R(\boldsymbol{\rho};\xi)\rangle_\xi}{\langle \sigma(\boldsymbol{\rho};\xi)\rangle_\xi} = \frac{m_i^{(1)} - m_R^{(1)}}{m_\sigma^{(1)}} \tag{II.19}$$

$$F_T = \frac{M_T^{(2)}}{M_T^{(1)}} = F_i \frac{m_\sigma^{(1)} m_i^{(1)}}{\widetilde{m}_\sigma^{(2)}(m_i^{(1)} - m_R^{(1)})} - \frac{\widetilde{m}_R^{(2)} m_\sigma^{(1)}}{\widetilde{m}_\sigma^{(2)}\left(m_i^{(1)} - m_R^{(1)}\right)} \tag{II.20}$$

Eq. (II.17) shows that, in principle, one can reconstruction the probability distribution function of targeted scattering potential by reconstructing all the statistical moments. However, in practice one must consider overall procedural noise for reconstruction of higher order moments of the targeted scattering potential.

In the case that illumination intensity is not δ-correlated, Eq. (II.13) for $k = 2$ can be rewritten

$$\widetilde{m}_i^{(2)} = \iint \langle \tilde{\sigma}(\boldsymbol{\rho};\xi)\tilde{\sigma}(\boldsymbol{\rho}';\xi) T(\boldsymbol{\rho}) T(\boldsymbol{\rho}')\rangle_\xi d\boldsymbol{\rho} d\boldsymbol{\rho}' + \widetilde{m}_R^{(2)} =$$

$$\iint \langle \psi(\boldsymbol{\rho};\xi, l_S)\psi(\boldsymbol{\rho}+\boldsymbol{\rho}';\xi, l_S)\rangle_\xi d\boldsymbol{\rho} d\boldsymbol{\rho}' + \widetilde{m}_R^{(2)}, \tag{II.21}$$

where the function $\psi(\boldsymbol{\rho};\xi,l_s)=\tilde{\sigma}(\boldsymbol{\rho};\xi,l_s)V(\boldsymbol{\rho};l_T)$ denotes the effective intensity fluctuations of the scattered light. Eq. (II.21) shows the nonlinear transformation discussed in the main text in Eq. (8).

## Significance of a Maximum in Fano Spectrum

Without loss of generality, in noiseless conditions, realization $\xi$ of illumination, the recorded intensity is

$$i(\xi)=\int I(\boldsymbol{\rho};\xi,l_S)T(\boldsymbol{\rho};l_T)d\boldsymbol{\rho} \tag{II.22}$$

where $I(\boldsymbol{\rho};\xi,l_S)$ represents the illumination pattern with characteristic length $l_S$ and $T(\boldsymbol{\rho};l_T)$ represents the targeted scattering potential with characteristic length $l_T$. For simplicity, an illumination intensity structure consisting of randomly distributed elementary structures can be represented as

$$I(\boldsymbol{\rho};\xi,l_S)=\sum_{m=1}^{M}\delta(\boldsymbol{\rho}-\boldsymbol{\rho}_m;\xi)*e(\boldsymbol{\rho};l_S)=C_S(\boldsymbol{\rho};\xi)*e(\boldsymbol{\rho};l_S). \tag{II.23}$$

Where $*$ denotes the operation of convolution and $\delta$ denotes delta function. The function $C_S(\boldsymbol{\rho})$ denotes the locations of the $M$ elementary units, each of them represented by $e(\boldsymbol{\rho};l_S)$. To describe a random illumination structure, the locations of the delta functions are modeled by a random variable uniformly distributed to cover uniformly the entire field and suppress any required *a priori* information about the target. It follows that:

$$\tilde{\imath}(\xi)=i(\xi)-\langle i(\xi)\rangle_\xi=i(\xi)-\left\langle\int I(\boldsymbol{\rho};\xi,l_S)T(\boldsymbol{\rho};l_T)d\boldsymbol{\rho}\right\rangle_\xi$$
$$=\int\left(I(\boldsymbol{\rho};\xi,l_S)-\langle I(\boldsymbol{\rho};\xi,l_S)\rangle_\xi\right)T(\boldsymbol{\rho};l_T)d\boldsymbol{\rho}=\int\tilde{T}(\boldsymbol{\rho};\xi,l_S)T(\boldsymbol{\rho};l_T)d\boldsymbol{\rho}, \tag{II.24}$$

where $\tilde{I}(\boldsymbol{\rho};\xi,l_S)$ is the zero mean illumination pattern defined by

$$\tilde{I}(\boldsymbol{\rho};\xi,l_S)=\sum_{m=1}^{M}\delta(\boldsymbol{\rho}-\boldsymbol{\rho}_m;\xi)*\tilde{e}(\boldsymbol{\rho};l_S)=C_S(\boldsymbol{\rho};\xi)*\tilde{e}(\boldsymbol{\rho};l_S), \tag{II.25}$$

The function $\tilde{e}(\boldsymbol{\rho}; l_S)$ represents the variation of the elementary unit of illumination pattern with respect to the average illumination intensity and, therefore, $\int \tilde{e}(\boldsymbol{\rho}; l_S) d\boldsymbol{\rho} = 0$. As a result, the intensity fluctuation becomes

$$\tilde{\imath}(\xi) = \int T(\boldsymbol{\rho}; l_T)\big(C_S(\boldsymbol{\rho}; \xi) * \tilde{e}(\boldsymbol{\rho}; l_S)\big) d\boldsymbol{\rho} = \int C_S(\boldsymbol{\rho}; \xi)\big(T(\boldsymbol{\rho}; l_T) * \tilde{e}(-\boldsymbol{\rho}; l_S)\big) d\boldsymbol{\rho}. \quad \text{(II.26)}$$

In this case, one can calculate integrated intensity variance $\sigma_I^2 = \langle \tilde{I}^2(\xi) \rangle$ as

$$\sigma_i^2 = \iint \langle C_S(\boldsymbol{\rho}; \xi) C_S(\boldsymbol{\rho}'; \xi) \rangle_\xi \big(T(\boldsymbol{\rho}'; l_T) * \tilde{e}(-\boldsymbol{\rho}'; l_S)\big)\big(T(\boldsymbol{\rho}; l_T) * \tilde{e}(-\boldsymbol{\rho}; l_S)\big) d\boldsymbol{\rho}' d\boldsymbol{\rho}. \quad \text{(II.27)}$$

Having elementary units in the illumination distributed randomly over the space, one can conclude that $\langle C_S(\boldsymbol{\rho}; \xi) C_S(\boldsymbol{\rho}'; \xi) \rangle_\xi = \delta(\boldsymbol{\rho} - \boldsymbol{\rho}')$. Moreover, average scattering coefficient of the scattering potential, i.e. $T(\boldsymbol{\rho}; l_T) - \tilde{T}(\boldsymbol{\rho}; l_T) = \int T(\boldsymbol{\rho}; l_T) d\boldsymbol{\rho}$, has zero contribution in Eq. (II.28). Consequently, Eq. (II.22) can be simplified to

$$\begin{aligned} \sigma_i^2 = \langle \tilde{I}^2(\xi) \rangle &= \int \Big(\tilde{T}(\boldsymbol{\rho}; l_T) * \tilde{e}(-\boldsymbol{\rho}; l_S)\Big)\Big(\tilde{T}(\boldsymbol{\rho}; l_T) * \tilde{e}(-\boldsymbol{\rho}; l_S)\Big) d\boldsymbol{\rho} \\ &= \int \Big(\tilde{T}(\boldsymbol{\rho}; l_T) * \tilde{T}(-\boldsymbol{\rho}; l_T)\Big)\big(\tilde{e}(\boldsymbol{\rho}; l_S) * \tilde{e}(-\boldsymbol{\rho}; l_S)\big) d\boldsymbol{\rho} \\ &= \int \Gamma_{\mathrm{I}}(\boldsymbol{\rho}, l_S) \Gamma_T(\boldsymbol{\rho}, l_T) d\boldsymbol{\rho}, \end{aligned} \quad \text{(II.29)}$$

Where $\Gamma_T(\boldsymbol{\rho}, l_S)$ and $\Gamma_I(\boldsymbol{\rho}, l_S)$ denote scattering potential strength and illumination field intensity autocorrelation function. According to the Cauchy-Schwarz inequality, variance attain its maximum if $\Gamma_{\mathrm{T}}(\boldsymbol{\rho}, l_T) = \Gamma_I(\boldsymbol{\rho}, l_S)$. In practical condition though, variance spectrum has a local maximum, when extent of these two function, i.e. the correlation length of the illumination intensity and the targeted potential scattering strength, become comparable.

## Procedure Repeatability

In chapter 2 and the Appendix B, we have shown that a random scattering potential is characterized by statistically analyzing fluctuations of scattered light in response to a random illumination, from the potential. As shown in Eq. (9) in the main text, if perturbations sources are

stationary, acquired parameters describing the information will not change by repeating the experiment. This is the advantage of working with statistical parameters.

Here we considered two different cases. In the first example, we consider the target shown in Figure 7(a) in chapter 2 and in the second case we consider the results shown in Figure 9 in the text. In the first example, the sensing procedure is reliable if the two peaks are still distinguishable and in the second example, the error bar should not decrease the visibility of the changes in the Fano factor spectrum. To make error bars more visible, they are plotted for ±3σ instead of ±σ of variation of the spectrum while repeating the sensing procedure. To consider effect of noise, these examples are demonstrated with SNR≈2dB.

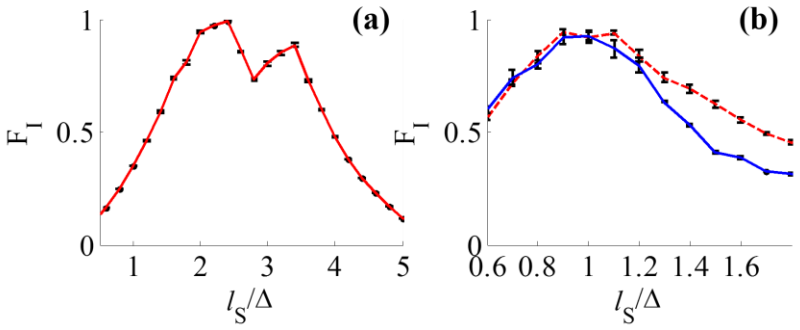


Figure 38 Demonstration of repeatability of the sensing procedure for target shown in Figure 7(a) and Figure 9(b) in the main text. In figure (b) continuous line and dashed line are corresponding to the symmetric and asymmetric case respectively. Error bars show $\pm 3\sigma$ of variation of the spectrum over repetition.

As evident from the Figure 38, the variation in Fano spectrum is very small. Although the error bars are plotted for ±3σ, they are significantly smaller than the variation of the spectrum itself. These examples show that even in highly perturbed condition, working with statistical parameters makes the characterization of a scattering potential more reliable. This is because the sources of perturbation are stationary stochastic processes that are statistically independent from the non-stationary random sampling imposed by the illumination. This property makes them statistically distinguishable.

## Optical Setup

An experimental setup was designed to demonstrate the proposed stochastic sensing technique and the result is shown in Figure 7(d) in the text. Schematic of the setup is shown in Figure 39. For this purpose a polarized CW laser beam (Doubled Nd:Yag, λ=532 nm) is expanded with a home built telescopic beam expander and then polarized to $45^0$ using a half wave plate followed by a polarizer. This beam illuminates a liquid crystal spatial light modulator (SLM) operating in reflection mode with 512×512 pixels, pitch size of 15μm×15μm (Boulder Nonlinear System Model P512-0532). The SLM impose a spatially varying polarization onto a laser beam which is converted to an intensity modulation by a polarizer after spatially filtering reflected light from the SLM in its Fourier plane to remove higher diffraction orders created by the pixilation of the SLM.

Relay optics are used to image the amplitude modulated light onto the back focal plane of a 60x microscope objective (Edmund Optics DIN 60X, NA=0.86). The magnification is adjusted through this relay optics system. Reflected light from the target is collected by a silicon integrator detector (PULNix TM-1040, with peak quantum efficiency of 38%) and generated voltage is recorded using NI PCI-6280 National Instrument data acquisition device. The entire process is controlled by LabVIEW software developed specifically for this purpose. The experimental SNR is calculated by the ratio of power of reflected light from the target to power of background light when the target path is blocked.

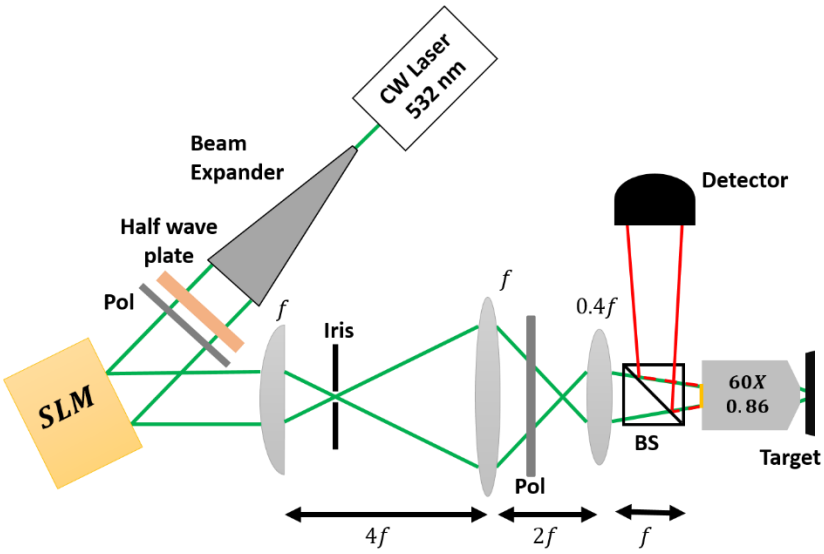


Figure 39 Detailed Schematic of experimental setup. An expanded polarized CW laser λ=532nm is polarized to 45° and then modulated by phase only spatial light modulator (SLM). After the first lens f=125mm, the Iris is blocked higher diffraction order created by the pixilation of the SLM. Phase modulated light is converted to an amplitude modulated light by a polarizer. Reflected beam from the target is directed toward the integrator detector by a beam splitter cube (BS).

## Auto-Correlation Function of Non-Sparse Random Targets in Figure 9

As evident in the results included in Figure 9(c) in the main text, changes in the auto-correlation function of non-sparse targeted potential shown in Figure 9(a) and (b) in the text, could be sensed by increasing tail of Fano factor spectrum due to introducing a new characteristic length. In this section we will compare auto-correlation function of the two targets to see how it has been changed by elongating some of the objects along different directions. Auto-correlation functions for symmetric and asymmetric cases are shown in Figure 40(a) and (b) respectively.

As it is clear from Figure 40(c), auto-correlation function has changed slightly in the side lobes. Sensing this small change can be challenging due to the environmental noise. However, this change is reliably measured as it is shown in Figure 9(c) and Figure 38(b).

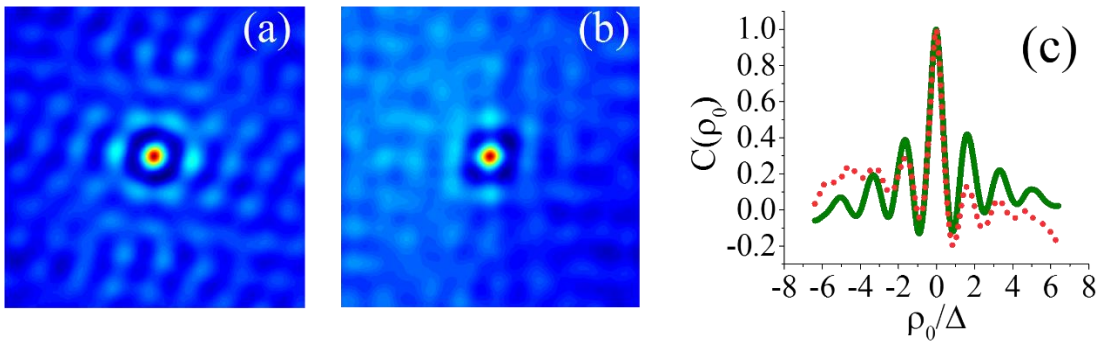


Figure 40 Comparison of correlation function of the non-sparse random shape target in (a) Symmetric and (b) Asymmetric phase. (c) Comparison of average of central portion of the correlation function along vertical axis for (green solid line) symmetric and (red dotted line) asymmetric case.

## High-Speed Experimental Setup

The scattering potential is considered to be stationary in here. As a result, to maintain this valid during the biological sample examination, the experimental setup was modified to work fast enough. Specifically, if one wish to repeat the experiment, the setup has to work much faster than the evolution time constant of the target. The result shown in Figure 10(b) in the text, is the average of 100 measurements on live H9c2 cells. For this experiment, the experimental setup was modified to take advantage of digital micro mirror device (DMD) as a fast intensity light modulator. For this purpose we used a 0.7" XGA VIS, TI DLP Discovery D4100 kit DMD to spatially modulate light generated by a CW laser with $\lambda$=532nm. The total reflection from the target is recorded with a Hamamatsu H6180-01 photomultiplier tube (PMT) connected to a data acquisition counter device PCI 6602 by National Instrument, and the sensing procedure is controlled with a LabVIEW software developed specifically for this purpose. Schematic of this setup is shown in Figure 41.

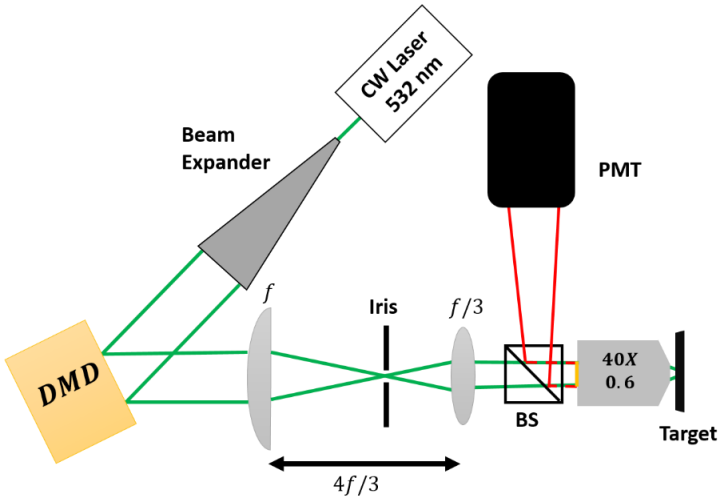


Figure 41 Detailed Schematic of experimental setup. An expanded polarized CW laser λ=532nm intensity modulated by DMD. After the first lens f=100mm, the Iris is blocked higher diffraction order created by the pixilation of the SLM. Reflected beam from the target is directed toward the photomultiplier tube (PMT) a beam splitter cube (BS).

## Biological Sample Preparation

H9c2 cells are cultured in a 35mm glass bottom petri dish by MatTek Corporation with class 0 cover slip in the bottom. Cells are grown in cell aqueous media (DMEH+10%FPS+1x p/s), and then they are left in the incubator over night to have enough time to stick to the cover slip. In the next day, petri dish is used as sample in the setup and structured light, is illuminated from the bottom. Cells are examined after the experiment and they were still healthy and alive.

# APPENDIX C: EXPLOITING AVAILABLE KNOWLEDGE IN COMPRESSIVE STOCHASTIC OPTICAL SENSING

## DERIVATION OF $\boldsymbol{l_{eq}}$ IN EQ. (15)

Using Parseval's theorem one can represent the Eq. (4) in the main text as

$$\sigma_i^2(l) \propto \int C_I(\Delta\boldsymbol{\rho}; l) C_T(\Delta\boldsymbol{\rho}; d) d\boldsymbol{r} = \int \mathcal{F}\{C_I(\Delta\boldsymbol{\rho}; l)\} \mathcal{F}\{C_T(\Delta\boldsymbol{\rho}; d)\}^* d\boldsymbol{\rho}. \quad \text{(III .1)}$$

As it is apparent from Eq. (III.1), integrated intensity variance is equal with the overlap integral of the apodized spatial spectrum of the illumination intensity, i.e. Fourier transform of the auto-correlation function. Consequently, one can define equivalent secondary patterns such that it maintains similar low frequency representation.

To be more specific, we consider two secondary patterns with circular features with corresponding length scale of $l_n$ and $l_m$. Cross correlation function of such intensity patterns can be stated as

$$C(\Delta\boldsymbol{\rho}; l_n, l_m) = circ(r/l_n) * circ\left(-\frac{r}{l_m}\right), \quad \text{(III.2)}$$

where $*$ denotes convolution operator. Equivalently, this cross correlation function can be represented in the frequency domain as

$$\mathcal{F}\{C(\Delta\boldsymbol{\rho}; l_n, l_m)\} = \frac{2J_1(kl_n)}{kl_n}\frac{2J_1(kl_m)}{kl_m}. \quad \text{(III.3)}$$

Where $J_1(x)$ denotes the first order Bessel function and $k = 2\pi/\lambda$ is the wave number for the wavelength $\lambda$. On the other hand, equivalent autocorrelation function $C\left(\Delta\boldsymbol{\rho}; l_{eq}\right)$ can be represented in frequency domain as

$$\mathcal{F}\left\{C\left(\Delta\boldsymbol{r}; l_{eq}\right)\right\} = \left(\frac{2J_1(kl_{eq})}{kl_{eq}}\right)^2. \quad \text{(III.4)}$$

Considering low frequency components only, one can exploit first two terms of the Bessel function Taylor expansion $J_1(x) \approx x(1/2 - x^2/16)$ to achieve

$$\left(1 - \left(kl_{eq}\right)^2/8\right)^2 = (1 - (kl_n)^2/8)(1 - (kl_m)^2/8). \quad \text{(III.5)}$$

In diffraction-limited scenarios in which circular features are much larger than the wavelength, one can conclude that $\min(l_n, l_m) \gg \lambda/2 > \sqrt{2}\lambda/\pi$, Therefore, $\min(l_n, l_m)^2\, k^2/8 \gg 1$. Consequently, one can further simplify Eq. (III.5) and represent it as

$$\left(kl_{eq}\right)^2 = kl_n \cdot kl_m \tag{III.6}$$

or equivalently $l_{eq} = \sqrt{l_n l_m}$, Which is the approximation used in Eq. (15).

## RECONSTRUCTION ALGORITHM

As we discussed earlier in Chapter Two, measured variances $\sigma_i^2(S)$ and the variance spectrum $\sigma_i^2(l)$ of the targeted potential are connected through the linear relation represented by

$$\sigma_i^2(S) = A(S, l)\sigma_i^2(l). \tag{III.7}$$

In principle, Eq. (III.7) has an analytical solution given by $(A^T A)^{-1} A^T \sigma_i^2(S)$. However, since transformation matrix has a random structure, this inversion is not always possible. Moreover, even if it is possible, inversion is usually prone to computational noise. Furthermore, regardless of the specific targeted potential, one can exploit available prior knowledge about generic realistic targeted potentials. To address these issues, one can solve Eq. (III.7) numerically through minimizing the energy function

$$\epsilon(\sigma_i^2(l)) = \|A(S, l)\sigma_i^2(l) - \sigma_i^2(S)\|_2 + \phi(\sigma_i^2(l)), \tag{III.8}$$

in which $\phi(\sigma_i^2(l))$ is non-negative regularization function and $\sigma_i^2(l) \geq 0$. The first term in Eq. (III.8) models the error in satisfying Eq. (III.7), while the second term is modeling prior knowledge.

In our demonstration, we have exploited two physical constraints. (i) Boundedness: according to Eq. (14) in the main text, variance spectrum is bounded within a range. This constraint can be satisfied by limiting $\ell_2$ norm of the spectrum, i.e. $\left\|\sigma_i^2(l)\right\|_2$. (ii) Smoothness: a realistic target has

limited spatial bandwidth, consequently, its variance spectrum supposed to be smooth. This constraint can be satisfied through limiting the norm of the spectrum differentiation, i.e. $\left\|\nabla_l \sigma_i^2(l)\right\|_2$ where $\nabla_l$ denotes differentiation with respect to $l$.

These two constraints can be exploited in recovering the variance spectrum through regularizing energy function by

$$\phi(\sigma_i^2(l)) = \lambda_1 \left\|\sigma_i^2(l)\right\|_2 + \lambda_2 \left\|\nabla_l \sigma_i^2(l)\right\|_2, \tag{III.9}$$

where $\lambda_1$ and $\lambda_2$ are regularization coefficients. Furthermore, since information is embedded only in the location of the local extremums in the variance spectrum, one can enhance visibility of the local peaks through slightly regularizing the energy function by $\ell_1$ norm of the spectrum by

$$\phi(\sigma_i^2(l)) = \lambda_1 \left\|\sigma_i^2(l)\right\|_2 + \lambda_2 \left\|\nabla_l \sigma_i^2(l)\right\|_2 + \lambda_2 \left\|\sigma_i^2(l)\right\|_1. \tag{III.10}$$

Here we used CVX software package implemented in MATLAB [164, 165] to solve Eq. (III.8) with regularization function shown in Eq. (III.10). To demonstrate effect of each term, we conducted a simulation in which $A(S, l)$ is a random transformation matrix shown in Figure 42(a) that transfer a given spectrum, Figure 42(b), into the measured variances that is shown in Figure 42(c).

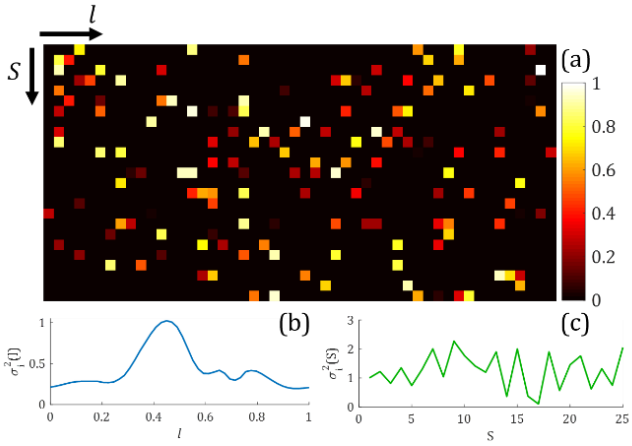


Figure 42 Applying a generic sparse random transformation matrix shown in (a) to a typical spectrum shown in (b) results in (c) measured variance that has random fluctuations.

For this given typical rectangular transformation matrix, analytical solution does not exist because $\det(A^T A) = 0$, where $\det(\cdot)$ denotes matrix determinant. This is a typical condition for a random sparse transformation matrix. To solve this inverse problem, we have minimized the energy function, Eq. (III.7) and we have investigated effect of different regularization terms. Figure 43(a) demonstrated recovered variance spectrum without any regularization. As it is apparent, recovered spectrum is noisy and has large fluctuations that can be suppressed by regularizing $\ell_2$ norm of the spectrum. This will reduce noisy fluctuations as it is shown in Figure 43(b). Nevertheless, the spectrum can be further smoothed using regularization function in Eq. (S3) as it is shown in Figure 43(c). Furthermore, the contrast of maximum of the spectrum can be enhanced using regularization function proposed by Eq. (III.4).

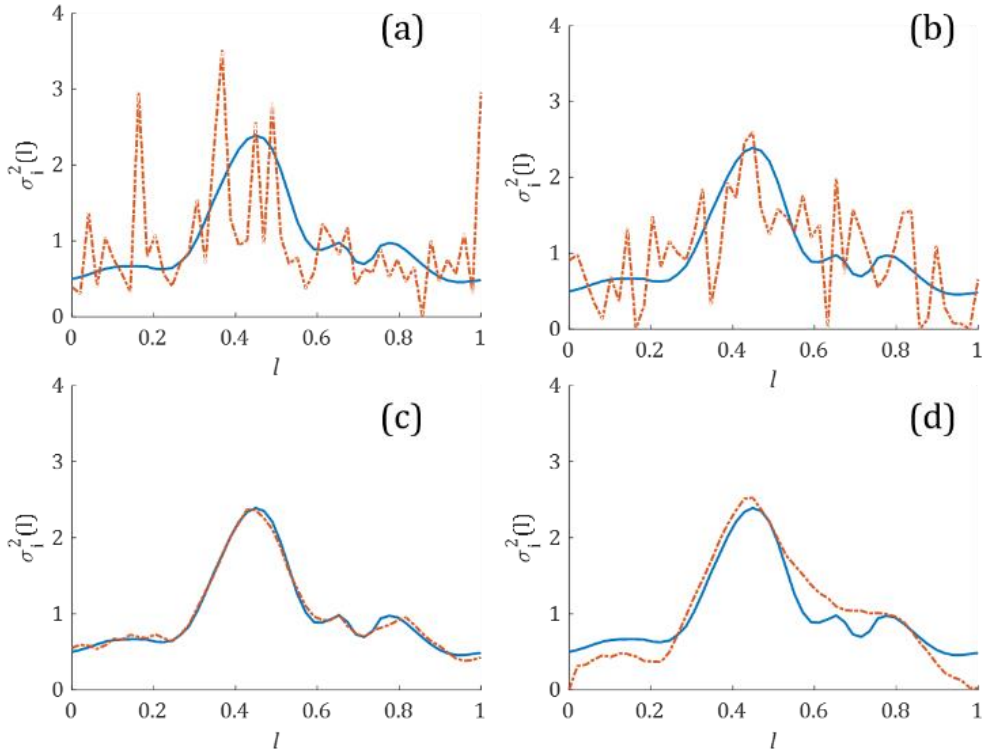


Figure 43 A generic variance spectrum is sampled using random transformation matrix shown in Figure 42 and then recovered through minimizing energy function in Eq. (III.2) (a) without regularization, (b) by regularizing only with $\ell_2$ norm, and using regularization function in (c) Eq. (III.3) and (d) Eq. (III.4). (-) denote the given spectrum and (-·) denotes reconstructed spectrum.

As it is apparent from Figure 43(d), enhanced contrast of the spectrum comes at the cost of small deviation from the ideal spectrum. Consequently, if local extremum in the variance spectrum has high contrast, regularization function introduced in Eq. (III.3) will suffice. This is usual the case when one is after characterizing a highly scattering target in presence of weak perturbation sources. However, when targeted potential is weakly scattering, e.g. biological targets, enhancing contrast of the spectrum would be of paramount importance. Nevertheless, since information is embedded inly in the location of the maximum, small deviation from the spectrum will not affect information acquisition.

In practice where known spectrum is not available for tuning regularization parameters, one can chose the regularization factors $\lambda_i$ such that fast noisy-like variations in the spectrum gets suppressed while slower variation maintain high contrast, as it is suggested by the demonstration shown in Figure 43. In our experimental results shown in Figure 14, regularization factors were $\lambda_1 = 0.2$, $\lambda_2 = 2$ and $\lambda_3 = 0.2$. In time lapse experiment though, these factors are set at $\lambda_1 = 2.5$, $\lambda_2 = 5$ and $\lambda_3 = 0.2$.

## EFFECT OF HIGHER COMPRESSION RATIO

Figure 14 in demonstrate measured variance spectrum for two different types of scattering potentials using conventional and compressive approach for compression ratio of 2. Of course, in principle, compression ratio is not limited by 2, in practice though, properties of the object can effectively impede increasing compression ratio. Figure S3 demonstrates effect of increasing compression ratio to 4 by decreasing number of realizations by a factor of parameter *R*, for the scattering potentials studied in Fig. 4 in the main text.

As it is Apparent from Figure 44, increasing compression ratio results in increasing variation of the spectrum from one measurement to another one. In spite of that, since information is embedded

only in the location of the peak, it can be recovered even at higher compression ratio. It also worth emphasizing that the variance spectrum associated with the weakly scattering potential is more sensitive to the compression ratio as expected. This property is also obvious in Figure 44.

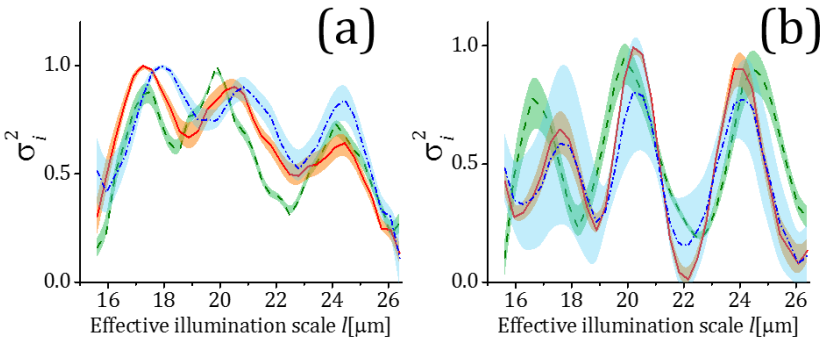


Figure 44 Variance spectrum associated with (a) Target consisting of metallic strips on glass substrate and (b) dense cell culture shown in Fig. Figure 14 (b and d), respectively. The dashed green curves and the green shaded area denoted the mean and the standard deviation of the variance spectrum measured using conventional SOS while the solid red with the orange shaded area and blue dashed dot line and light blue shaded area represent the corresponding ones acquired using cSOS with compression ratio of 2 and 4 respectively.

# APPENDIX D: PROOFS AND DETAILS ON TRACKING HIDDEN OBJECTS USING DYNAMIC FLUCTUATION

## Interaction Formulation

Here we derive Eqs. (11-16) of the main text. We start by considering the diffused light illuminating the target as a time varying spatially partially coherent illumination $\mathcal{E}_I(\boldsymbol{r},t)$, and we calculate the integrated scattered light intensity $i(t)$. Then, we derive the relationships between (i) the variance $\sigma_i^2$ of the fluctuations of integrated intensity and axial location z, and (ii) the decorrelation time $\tau_i$ of the intensity fluctuations and the target velocity transversal component $v_{T,\parallel}$.

The physical problem is characterized by three time scales describing the dynamics of the illumination speckle field $\tau_{sp}$, target $\tau_t$, and the scattering wall $\tau_w$. We consider that these characteristic times satisfy $\tau_{sp} < \tau_t < \tau_w$. In this case, the scattering obscurant can be dynamic but its effect on the intensity fluctuations is negligible. Moreover, we consider the target motion to be independent of the speckle modifications introduced by the incident beam's tilt or translation.

Let the target be described by its scattering potential $\mathcal{P}(\boldsymbol{r})$, and assume that the scattering is weak such that the first-order Born approximation can be used to derive the scattered field at the location $\boldsymbol{r}_d$ in the detection plane. Thus, the scattered field can be written as

$$\mathcal{E}_s(\boldsymbol{r}_d,t) = \int \mathcal{P}(\boldsymbol{r}',t)\mathcal{E}_I(\boldsymbol{r}',t)\frac{e^{ik|r_d-r'|}}{|r_d-r'|}dr' \qquad \text{(IV.1)}$$

where $k$ is the wave number and the integral extends over the target domain $\boldsymbol{r}' = \boldsymbol{\rho}(x,y) + z\hat{z}$. The targeted scattering potential can be represented generically as $\mathcal{P}(\boldsymbol{r}) = k^2(n^2(\boldsymbol{r}) - 1)/4\pi$ in terms of refractive index distribution and the wavenumber $k = 2\pi/\lambda$ [65, 88, 166].

As long as illumination field $\mathcal{E}_I(\boldsymbol{r},t)$ is statistically stationary, at least in the wide sense, the partially coherent scattered field will also be statistically stationary. Consequently, this field can be fully characterized through its cross-correlation function

$$C(\boldsymbol{r}_1, \boldsymbol{r}_2, t, \tau) = \langle \mathcal{E}_s^*(\boldsymbol{r}_1, t)\mathcal{E}_s^*(\boldsymbol{r}_2, t+\tau)\rangle_\alpha \quad \text{(IV.2)}$$

where $\langle \dots \rangle_\alpha$ denotes the average taken over the scattered field realizations. There are 2 time variables in this equation. The first time scale describes the temporal variation of the ensemble average field. This is the time variable of the average measured intensity and is denoted by $t$ throughout the main text and the Appendix. The second time scale is much smaller than the first one and describes the fluctuations from one field realization $\alpha$ to another.

Using Eq. (IV.2) and considering that the illumination field and the scattering potential are statistically independent, the time varying mutual intensity of the scattered field for $\tau = 0$ can be evaluated as

$$J_s(\boldsymbol{r}_1, \boldsymbol{r}_2, t) = \iint \langle \mathcal{P}^*(\boldsymbol{r}'_1, t)\mathcal{P}(\boldsymbol{r}'_2, t)\rangle_\beta \langle \mathcal{E}_I^*(\boldsymbol{r}'_1, t)\mathcal{E}_I(\boldsymbol{r}'_2, t)\rangle_\eta \frac{e^{ik(|\boldsymbol{r}_2 - \boldsymbol{r}_2{}'| - |\boldsymbol{r}_1 - \boldsymbol{r}_1{}'|)}}{|\boldsymbol{r}_2 - \boldsymbol{r}_2{}'||\boldsymbol{r}_1 - \boldsymbol{r}_1{}'|} d\boldsymbol{r}'_1 d\boldsymbol{r}'_2 \quad \text{(IV.3)}$$

where $\langle \dots \rangle_\beta$ and $\langle \dots \rangle_\eta$ denote averages taken over the realizations of the scattering potential and the illumination field, respectively.

The diffused illumination light can be considered to be a quasi-homogeneous field with its cross-correlation function of the form

$$C_I(\boldsymbol{r}'_1, \boldsymbol{r}'_2, t) = \langle \mathcal{E}_I^*(\boldsymbol{r}'_1, t)\mathcal{E}_I(\boldsymbol{r}'_2, t)\rangle_\eta = I(\bar{\boldsymbol{r}}, t)\mu(\Delta\boldsymbol{r}, d, z) \quad \text{(IV.4)}$$

where $\bar{\boldsymbol{r}} = (\boldsymbol{r}'_1 + \boldsymbol{r}'_2)/2$, $\Delta\boldsymbol{r} = \boldsymbol{r}'_2 - \boldsymbol{r}'_1$. $I(\bar{\boldsymbol{r}}, t)$ represents the intensity distribution, and $\mu(\Delta\boldsymbol{r}, \mathrm{d}, z)$ denotes the degree of spatial coherence of the illumination field, which depends on the size of the secondary source $d$ that generates the illumination of the target. The targeted potential can also be thought as a quasi-homogeneous distribution for which cross-correlation can be well approximated [65, 166, 167] by

$$C_{\mathcal{P}}(\boldsymbol{r}'_1, \boldsymbol{r}'_2, t) = \langle \mathcal{P}^*(\boldsymbol{r}'_1, t)\mathcal{P}(\boldsymbol{r}'_2, t)\rangle_\beta = T(\bar{\boldsymbol{r}}, t)\gamma(\Delta\boldsymbol{r}, z) \quad \text{(IV.5)}$$

where T($\bar{\boldsymbol{r}}, t$) denotes the scattering strength at location $\bar{\boldsymbol{r}}$ at time $t$, and $\gamma(\Delta \boldsymbol{r}, z)$ is the degree of spatial correlation of the targeted potential.

By substituting Eq. (IV.4) and (IV.5) in Eq. (IV.3), and using an asymptotic approximation

$$\frac{e^{ik|r\boldsymbol{u}-\boldsymbol{r}'|}}{|r\boldsymbol{u}-\boldsymbol{r}'|} = \frac{e^{ikr}}{r} e^{-i\boldsymbol{k}.\boldsymbol{r}'} \tag{IV.6}$$

of the Green's function at distance $r$ in the direction $\boldsymbol{k}$**,** the time varying intensity of the scattered light at a distance $r_d$ along the direction $\boldsymbol{k}$ can be written as

$$I_S(\boldsymbol{k}, t; r_d) \approx \frac{1}{r_d^2} \iint T(\bar{\boldsymbol{r}}, t) I(\bar{\boldsymbol{r}}, t) \mu(\Delta \boldsymbol{r}, d, z) \gamma(\Delta \boldsymbol{r}, z)\, e^{i\boldsymbol{k}\cdot(\boldsymbol{r}_2'-\boldsymbol{r}_1')} d\boldsymbol{r}_1' d\boldsymbol{r}_2'. \tag{IV.7}$$

For quasi-homogenous distributions of both the illumination and the scattering potential, the functions T and I vary much slower than γ and μ and one can approximate the scattered intensity as

$$I_S(\boldsymbol{k}, t; r_d) \approx \left(\frac{1}{r_d^2} \int T(\bar{\boldsymbol{r}}', t) I(\bar{\boldsymbol{r}}', t) d\boldsymbol{r}'\right) \left(\int \gamma(\Delta \boldsymbol{r}', z) \mu_i(\Delta \boldsymbol{r}', d, z) e^{i\boldsymbol{k}.\Delta \boldsymbol{r}'}\, d\Delta \boldsymbol{r}'\right) \tag{IV.8}$$

where the first and the second integral extend over the average and difference of any two position vectors in the interaction domain.

At a distance $r_d$ from the target, the scattered intensity can be integrated over the angular domain of the detector, $\boldsymbol{0} < \boldsymbol{k} < \boldsymbol{k}_{max}$, resulting in

$$i(t; r_d) = \int_0^{\boldsymbol{k}_{max}} I_s(\boldsymbol{k}, t; r_d) d\boldsymbol{k} = M(d, z) {r_d}^{-2} \int T(\boldsymbol{r}', t) I(\boldsymbol{r}', t) d\boldsymbol{r}'. \tag{IV.9}$$

The function $\mathrm{M}(\mathrm{d}, z) = \int_0^{\boldsymbol{k}_{max}} d\boldsymbol{k} \int \gamma(\Delta \boldsymbol{r}', z) \mu(\Delta \boldsymbol{r}', \mathrm{d}, z) e^{i\boldsymbol{k}.\Delta \boldsymbol{r}'} d\Delta \boldsymbol{r}'$, in which the outer integral is evaluated over the integration area of the scattered intensity while the inner integral is over the volume of interaction, should ideally tend to unity as the angular domain of integration expands to 4π.

As evident by Eq. (IV.9), the temporal variation of measured $i(t)$, is due to the dynamics of both the illumination field and target. In our tracking method, this means that the integrated intensity

depends on both the dynamic illumination intensity and the variation of the scattering strength, i.e. motion, of the target. Thus, one can control the variations of one of these sources to determine the temporal behavior of the other.

An important observation is in order here. The extent $\boldsymbol{k}_{max}$ of the angular domain of integration does not affect the temporal variations of the integrated intensity; the function M only affects the magnitude of $i(t)$. This angular domain of integration can be arbitrarily large, covering many different speckles. This also means that the presence of an additional scattering wall between the target and detector will not affect the temporal variations of the integrated intensity. This is the reason why, in our approach, the target can completely be surrounded by scattering media.

As discussed in the main text, one way to control the temporal variations of the illumination field is by exploiting the so-called memory effect which is an intrinsic property of the scattering wall. More specifically, tilting the primary illumination beam results in a transversal displacement of the speckle field that illuminates the target before the decorrelation occurs, after a time $\tau_I$. In this way a controlled dynamic is imposed to the illumination.

We will now evaluate the temporal auto-correlation of the integrated intensity $i(t)$, and show how it relates to the target dynamic. For times $t < \tau_I$, the integrated intensity varies like

$$i(t) = \int T(\boldsymbol{r} - \boldsymbol{v}_T \cdot t) I(\boldsymbol{r} - \boldsymbol{v}_I \cdot t) d\boldsymbol{r} = \int T(\boldsymbol{r}) I(\boldsymbol{r} - \Delta\boldsymbol{r}(t))\, d\boldsymbol{r} \qquad \text{(IV.10)}$$

where the integral extends over the interaction domain, $\boldsymbol{v}_I$ and $\boldsymbol{v}_T$ are the velocities of speckles illumination and the target, respectively, and $\Delta\boldsymbol{r}(t) = (\boldsymbol{v}_I - \boldsymbol{v}_T)t$. We note that the integrated intensity variation represents the convolution of the illumination intensity with the targeted potential scattering strength

$$i(t) = I(r,t) * T(r,t) \qquad \text{(IV.11)}$$

To characterize the dynamics of the integrated intensity, we use the temporal autocorrelation function $C_i(\tau)$ of the intensity variations which is defined as

$$C_i(\tau) = \langle i(t)i(t-\tau)\rangle_t = t_M^{-1}\int_0^{t_M}\big(I(r,t) * T(r,t)\big)(I(r,t-\tau) * T(r,t-\tau))dt \quad \text{(IV.12)}$$

where $t_M$ is the measurement time. Because the velocity is constant over the short duration of the measurement, $\Delta\boldsymbol{r}(t-\tau)$ is given by

$$\Delta\boldsymbol{r}(t-\tau) = (\boldsymbol{v}_I - \boldsymbol{v}_T)(t-\tau) = \Delta\boldsymbol{r}(t) - \Delta\boldsymbol{r}(\tau) \quad \text{(IV.13)}$$

and by using standard properties of convolution operator, autocorrelation function in Eq. (IV.12) becomes

$$C_i(\tau) = t_M^{-1}\int_0^{t_M} C_I(\Delta\boldsymbol{r}(t) - \tau\,\Delta\boldsymbol{v})C_T\big(\Delta\boldsymbol{r}(t)\big)dt. \quad \text{(IV.14)}$$

In Eq. (IV.14), $C_I$ and $C_T$ represent the spatial autocorrelations of the illumination intensity and the target scattering strength respectively, and $\Delta\boldsymbol{v} = \boldsymbol{v}_I - \boldsymbol{v}_T$. The illumination intensity decorrelates in time according to the memory effect and, for diffusive light, it has been shown [143-145] that

$$C_I(\Delta\boldsymbol{r}(t) - \tau\,\Delta\boldsymbol{v}) \approx (x/sinh(x))^2 C_I\big(\Delta\boldsymbol{r}(t)\big) \quad \text{(IV.15)}$$

where $x \propto |\Delta\boldsymbol{v}|\tau$. In our case, the time delay $\tau$ is induced by a change in illumination angle.

Substituting Eq. (IV.15) into Eq. (IV.14), the temporal autocorrelation of the integrated intensity can be written as

$$C_i(\tau) = t_M^{-1}(x/sinh(x))^2\int_0^{t_M} C_I\big(\Delta\boldsymbol{r}(t)\big)C_T\big(\Delta\boldsymbol{r}(t)\big)dt. \quad \text{(IV.16)}$$

The information about both axial and transversal motion of the target is included in the autocorrelation function $C_i(\tau)$ and can be quantified using two parameters: (i) the variance $\sigma_i^2 = C_i(0)$ and (ii) the decorrelation time $\tau_i$, defined according to a specific criterion, e.g. $C_i(\tau_i) = 0.5C_i(0)$.

According to Eq. (IV.16), the integrated intensity decorrelates after a specific delay time $\tau_i \propto 1/|\boldsymbol{v}_I - \boldsymbol{v}_T|$. By decomposing the target velocity $\boldsymbol{v}_T = \boldsymbol{v}_{T,\perp} + \boldsymbol{v}_{T,\parallel}$ into the perpendicular and parallel components to the speckles motion, this decorrelation time can be written as

$$\tau_i \propto |\boldsymbol{v}_I - \boldsymbol{v}_T|^{-1} = \frac{1}{v_I}\left[\sqrt{1 - 2v_{T,\parallel}/v_I + (v_T/v_I)^2}\right]^{-1/2} \quad \text{(IV.17)}$$

where $v = |\boldsymbol{v}|$. When the illumination dynamic is faster than the target motion, Eq. (IV.17) can be simplified using a Taylor expansion to become

$$\tau_i \propto \frac{1}{v_I}\left(1 + \frac{v_{T,\parallel}}{v_I}\right). \quad \text{(IV.18)}$$

Thus, the velocity of speckle motion is kept constant, the decorrelation time of the integrated intensity linearly depends on the component of target velocity oriented along the same direction of motion.

It should be noted that, although the motion along each axis is accelerated (due to change in speed and direction), due to the aforementioned condition on characteristic times $\tau_{sp} < \tau_t$, it can be approximated by the first two term of its Taylor expansion in each step. This is equivalent with having a constant speed along each axis over the short time of one measurement.

Having established the procedure to follow the target transversal motion, we now return to Eq. (IV.16) to extract the second piece of information related to the transversal motion. From Eq. (IV.16), the variance of the integrated intensity is

$$\sigma_i^2 = C_i(0) = t_M^{-1}\int_0^{t_M} C_I\big(\Delta\boldsymbol{r}(t)\big)C_T\big(\Delta\boldsymbol{r}(t)\big)dt. \quad \text{(IV.19)}$$

We note that according to the Cauchy-Schwarz inequality, the variance of recorded intensity increases when the two spatial autocorrelation functions become comparable. In other words, when the average size of the spackles $l$, or equivalently width of the $C_I$, matches the characteristic length scale of the target features, the intensity fluctuations are enhanced. This condition forms the basis

for Stochastic Optical Sensing [33, 110], where statistical similarity is detected as a resonance in the spectrum of this variance as function of the spatial correlation length of illumination intensity. Here, the same concept is used for assessing the target motion along the axial direction. In the next section, we show that for given experimental conditions, more specifically for a given size of the secondary source $d$, the variance $\sigma_i^2$ linearly depends on the axial motion of the target.

## Experimental Setup Details

In our demonstration, the target has feature size in the order of hundreds of microns and an overall size of 5mm×5mm. It is illuminated by a speckle field, in an area of roughly 5cm×5cm, while the field of view for detection roughly expands to 10cm×10cm. The schematic of the optical setup is shown in Figure 45. The primary light source is a HeNe laser with λ=632nm, with a beam width of 1mm which passes thorough a neutral density filter (ND) to adjust the level of light intensity. This beam impinges on a lens (LS, f=17mm, NA=0.25) that can be translated over a 1 mm range to control the beam's direction, location, and size $d$ on the scattering box. The box is made of 6mm thick Plexiglas that is covered completely with synthetic acrylics with thickness of $w \approx 650\mu m$ and scattering mean free path of $l_s \approx 70\mu m$. The target is located in the center of a 20cm×20cm×20cm scattering box and is displaced over a volume of 20mm$^3$. In this arrangement, the ballistic light that passes thorough the box is attenuated more than 8 orders of magnitude. A portion of the scattered light from the back wall of the scattering box is collected by a 5cm diameter lens $L_D$ with focal length $f = 15cm$ located 3cm behind the box. This scattered light is then detected by a Hamamatsu H6180-01 photomultiplier tube (PMT). Data collected by the PMT is recorded on the computer thorough National Instrument PCI-6602 data acquisition card operating in pulse counting mode.

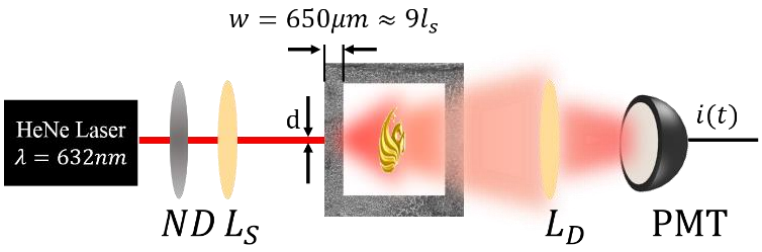


Figure 45 Schematic representation of the optical setup, (ND) neutral density filter, ($L_S$) lens associated with the secondary source to adjust direction, location and size d of the beam on the scattering wall, ($L_D$) lens associated with the detection system, and (PMT) photomultiplier tube.

Both the target and the first lens are moved using linear actuators Newport CMA-12PP, which are controlled by a Newport ESP 300 motion controller. The entire process of accessing the actuators, the data recording and processing are controlled by LabVIEW software. Due to the maximum speed afforded for target translation along each axis, the measurement integration time is chosen to be 1 second. The intensity is recorded in real time and the data is processed in MATLAB. Overall, the computation associated with each step is performed in less than 50msec.

## Algorithm for Trajectory Recovery

The algorithm used to recover the trajectory relies on the established linear dependency between measured parameters and target motion. If the target moves between successive measurements with constant but not necessarily the same velocity, at any given measurement step $j$, three independent linear relationships can be established between the target displacement and the measurable quantities $\sigma_i^2$ and $\tau_i$:

$$\Delta x^{(j)} = A_x \tau_{i,x}^{(j)} + B_x \quad \text{(IV.20)}$$

$$\Delta y^{(j)} = A_y \tau_{i,y}^{(j)} + B_y \quad \text{(IV.21)}$$

$$\Delta z^{(j)} = A_z \sigma_i^{2\,(j)} + B_z \quad \text{(IV.22)}$$

The constants $A_\zeta$ and $B_\zeta$, $\zeta \in \{x, y, z\}$, can be evaluated using four calibration measurements for which the target location and velocity are known. In other words, measurements for at least 2

different axial location $(z_1, z_2)$ with at least two different transverse velocities along each axis are needed. As each measurement is capable of providing two pieces of information, these 6 states can be mixed into four measurements.

When *a priori* information is available, the constants $A$ and $B$ can be evaluated through a linear regression as it is discussed in the main text in section 3.

In general, when there is no feedback from the target, i.e. information about its motion, the trajectory can be recovered only subject to the initial position. Practically, this means that the trajectory must be recovered without any information about the constants $A$ and $B$ in Eq. (IV.20-IV.22). We proceed as follows. Starting from Eq. (IV.20- IV.23) and denoting the incremental motion step $j$ as as $\rho^{(j)} \in \{\Delta x^{(j)}, \Delta y^{(j)}, \Delta z^{(j)}\}$ associated with the measured value $\xi^{(j)} \in \{\tau_{i,x}^{(j)}, \tau_{i,y}^{(j)}, {\sigma_i^2}^{(j)}\}$, We can further evaluate the difference $\Delta\rho^{(j)} = \rho^{(j)} - \rho^{(j-1)}$ between two such successive steps. Using Eq. (IV.20), one can see that this difference is independent of the constant $b_\rho$:

$$\Delta\rho^{(j)} = a_\rho\left(\xi^{(j)} - \xi^{(j-1)}\right) = a_\rho \Delta\xi^{(j)}. \tag{IV.23}$$

The remaining constant $a_\rho$ can also be eliminated by evaluating the ratio

$$\Delta\rho^{(j)}/\Delta\rho^{(l)} = \Delta\xi^{(j)}/\Delta\xi^{(l)}, \tag{IV.24}$$

where $j = l$ is the trivial case. However, for $j \neq l$ the trajectory can be evaluated recursively starting from known values $\xi^{(l)}$and $\Delta\rho^{(l)}$

$$\rho^{(j)} = \rho^{(j-1)} + \Delta\rho^{(l)}\,\Delta\xi^{(j)}/\Delta\xi^{(l)}. \tag{IV.25}$$

The practical choice is to start from $l = 2$ and consider the initial step to be $\rho^{(1)} = 0$. Lastly, to recover the trajectory, one has to calculate cumulative displacement

$$x^{(j)} = \sum_{n=1}^{j} \rho^{(n)} \tag{IV.26}$$

In the absence of any feedback or calibration, one can recover a scaled trajectory for which each successive displacement step is normalized with respect to the first one. For instance, when presenting the experimental result in Figure 25 of the main text, we consider $\rho^{(2)}$ to be unity. In other words, in real time, one recovers a scaled trajectory comprising the vector motion and the relative speed measured at each step.

Because Eq. (IV.20- IV.22) are independent, the same procedure can be applied for each axis to recover the full 3D time evolving trajectory. Eqs. (IV.26) and (IV.27) show that reconstructing each step relies only on information collected during the preceding step, which allows for real-time calculations.

# PUBLICATIONS AND PRESENTATIONS

## Refereed Journal Papers

J6. M. I. Akhlaghi and A. Dogariu, "Computational compressive stochastic optical sensing," under revision in Optica

J5. M. I. Akhlaghi and A. Dogariu, "Single-shot coherent noise suppression by spatial interferometric heterodyning," Optics Letters **42**, 2378 (2017)

J4. M. I. Akhlaghi and A. Dogariu, "Tracking hidden objects using stochastic probing," Optica **4**, 447 (2017)

J3. M. I. Akhlaghi and A. Dogariu, "Non-imaging statistical method for characterizing scattering media", SPIE Newsroom July 2016

J2. M. I. Akhlaghi and A. Dogariu, "Stochastic optical sensing," Optica **3**, 58 (2016)

J1. M. I. Akhlaghi and A. Dogariu, "Compressive correlation imaging with random illumination," Optics Letters **40**, 4464 (2015)

## Conference Proceedings

C11. M. I. Akhlaghi, L. Cilenti , A. Zervos, and A. Dogariu, "Dynamic Biological Systems Characterization Using non-Stationary Stochastic Optical Probe,", IPC, TuE2.4 (2017)

C10. S. Cui, Milad I. Akhlaghi, and A. Dogariu, "Quantitative Phase Imaging Through Encoding Phase into the State of Polarization," IPC, WH3.4 (2017)

C9. M. I. Akhlaghi and A. Dogariu, "Coherent Noise Suppression using Interferometric Cross-Correlation," COSI, CTu1B.3 (2017)

C8. M. I. Akhlaghi and A. Dogariu, "Compressive Stochastic Characterization of Scattering Media," COSI, CM4B.3 (2017)

C7. M. I. Akhlaghi and A. Dogariu, "Coherent Noise Reduction Using Heterodyne Detection," CLEO, SF2M.3 (2017)

C6. M. I. Akhlaghi and A. Dogariu, "Tracking objects surrounded by scattering media," CLEO, SF2M.1 (2016)

C5. M. I. Akhlaghi and A. Dogariu, "Sensing through obscurants - using fluctuations in stochastic coherent scattering," CLEO, AM4K.3 (2015)

C4. M. I. Akhlaghi, T. Kohlgraf-Owens, and A. Dogariu, "Active illumination low-light computational correlation microscopy," FiO/LS, LM2H.2 (2015)

C3. M.I. Akhlaghi and A. Dogariu, "Stochastic characterization of optical scattering potentials," FiO, FTh4D.5 (2015)

C2. M.I. Akhlaghi and A. Dogariu, "Computational optical density-density correlation sensing," CLEO, STh3O.7 (2015)

C1. M.I. Akhlaghi, T. Kohlgraf-Owens, and A. Dogariu, “Low-light reflective correlation imaging,” CLEO, STu2K.1 (2015)

# REFERENCES


1 W. T. Hill III, and C. H. Lee, *Light-matter interaction* (John Wiley & Sons, 2008).

2 F. Wooten, *Optical properties of solids* (Academic press, 2013).

3 J. C. Leader, "Intensity fluctuations resulting from partially coherent light propagating through atmospheric turbulence," JOSA **69**, 73-84 (1979).

4 Y. M. Blanter, and M. Büttiker, "Shot noise in mesoscopic conductors," Phys. Rep. **336**, 1-166 (2000).

5 M. Sonnleitner, J. Jeffers, and S. M. Barnett, "Image retrodiction at low light levels," Optica **2**, 950-957 (2015).

6 S. B. Dubin, J. H. Lunacek, and G. B. Benedek, "Observation of the spectrum of light scattered by solutions of biological macromolecules," PNAS **57**, 1164-1171 (1967).

7 D. Magde, E. Elson, and W. W. Webb, "Thermodynamic fluctuations in a reacting system—measurement by fluorescence correlation spectroscopy," Phys. Rev. Lett. **29**, 705 (1972).

8 R. Benzi, A. Sutera, and A. Vulpiani, "The mechanism of stochastic resonance," Journal of Physics A: mathematical and general **14**, L453 (1981).

9 T. Pittman, Y. Shih, D. Strekalov, and A. Sergienko, "Optical imaging by means of two-photon quantum entanglement," Phys. Rev. A **52**, R3429 (1995).

10 A. F. Abouraddy, P. R. Stone, A. V. Sergienko, B. E. Saleh, and M. C. Teich, "Entangled-photon imaging of a pure phase object," Phys. Rev. Lett. **93**, 213903 (2004).

11 A. K. Dunn, H. Bolay, M. A. Moskowitz, and D. A. Boas, "Dynamic imaging of cerebral blood flow using laser speckle," J. Cereb. Blood Flow Metab. **21**, 195-201 (2001).

12 A. P. Mosk, A. Lagendijk, G. Lerosey, and M. Fink, "Controlling waves in space and time for imaging and focusing in complex media," Nature Photonics **6**, 283-292 (2012).

13 M. Aubailly, and M. A. Vorontsovbc, "Digital adaptive optics and imaging through deep turbulence," in *Proc. of SPIE Vol*(2013), pp. 86100Y-86101.

14 C. Thomas, "Coherent optical noise suppression," Appl. Opt. **7**, 517-522 (1968).

15 J. M. Schmitt, S. Xiang, and K. M. Yung, "Speckle in optical coherence tomography," Journal of biomedical optics **4**, 95-105 (1999).

16 V. V. Dudorov, M. A. Vorontsov, and V. V. Kolosov, "Speckle-field propagation in "frozen" turbulence: brightness function approach," JOSA A **23**, 1924-1936 (2006).

17 M. Laurenzis, F. Christnacher, and D. Monnin, "Long-range three-dimensional active imaging with superresolution depth mapping," Opt. Lett. **32**, 3146-3148 (2007).

18 P. Li, S. Ni, L. Zhang, S. Zeng, and Q. Luo, "Imaging cerebral blood flow through the intact rat skull with temporal laser speckle imaging," Opt. Lett. **31**, 1824-1826 (2006).

19 T. Dertinger, R. Colyer, G. Iyer, S. Weiss, and J. Enderlein, "Fast, background-free, 3D super-resolution optical fluctuation imaging (SOFI)," PNAS **106**, 22287-22292 (2009).

20 T. Dertinger, R. Colyer, R. Vogel, J. Enderlein, and S. Weiss, "Achieving increased resolution and more pixels with Superresolution Optical Fluctuation Imaging (SOFI)," Opt. Express **18**, 18875-18885 (2010).

21 E. L. Elson, and D. Magde, "Fluorescence correlation spectroscopy. I. Conceptual basis and theory," Biopolymers **13**, 1-27 (1974).

22 D. Magde, E. L. Elson, and W. W. Webb, "Fluorescence correlation spectroscopy. II. An experimental realization," Biopolymers **13**, 29-61 (1974).

23 D. E. Koppel, "Statistical accuracy in fluorescence correlation spectroscopy," Phys. Rev. A **10**, 1938 (1974).

24 R. Benzi, G. Parisi, A. Sutera, and A. Vulpiani, "Stochastic resonance in climatic change," Tellus **34**, 10-15 (1982).

25 E. Simonotto, M. Riani, C. Seife, M. Roberts, J. Twitty, and F. Moss, "Visual perception of stochastic resonance," Phys. Rev. Lett. **78**, 1186 (1997).

26 B. McNamara, K. Wiesenfeld, and R. Roy, "Observation of stochastic resonance in a ring laser," Phys. Rev. Lett. **60**, 2626 (1988).

27 B. M. Jost, and B. E. Saleh, "Signal-to-noise ratio improvement by stochastic resonance in a unidirectional photorefractive ring resonator," Opt. Lett. **21**, 287-289 (1996).

28 M. I. Akhlaghi, and A. Dogariu, "Compressive correlation imaging with random illumination," Opt. Lett. **40**, 4464-4467 (2015).

29 M. A. Bouzan, T. Kohlgraf-Owens, and A. Dogariu, "Low-light reflective correlation imaging," in *CLEO: Science and Innovations*(Optical Society of America2015), p. STu2K. 1.

30 M. A. Bouzan, T. Kohlgraf-Owens, and A. Dogariu, "Active Illumination Low-light Computational Correlation Microscopy," in *Laser Science*(Optical Society of America2015), p. LM2H. 2.

31 M. A. Bouzan, and A. Dogariu, "Stochastic Characterization of Optical Scattering Potentials," in *Frontiers in Optics*(Optical Society of America2015), p. FTh4D. 5.

32 M. A. Bouzan, and A. Dogariu, "Computational optical density-density correlation sensing," in *CLEO: Science and Innovations*(Optical Society of America2015), p. STh3O. 7.

33 M. I. Akhlaghi, and A. Dogariu, "Stochastic optical sensing," Optica **3**, 58-63 (2016).

34 M. I. Akhlaghi, and A. Dogariu, "Non-imaging statistical method for characterizing scattering media," SPIE Newsroom (2016).

35 M. I. Akhlaghi, L. Cilenti , A. S. Zervos, and A. Dogariu, "Dynamic Biological Systems Characterization Using non-Stationary Stochastic Optical Probe," in *IEEE Photonics conference*(2017), p. TuE2.4.

36 M. A. Bouzan, and A. Dogariu, "Compressive Stochastic Characterization of Scattering Media," in *Computational Optical Sensing and Imaging*(Optical Society of America2017), p. CM4B. 3.

37 M. I. Akhlaghi, and A. Dogariu, "Computational Compressive Stochastic Optical Sensing," Optica, under revision (2017).

38 M. G. Gustafsson, "Surpassing the lateral resolution limit by a factor of two using structured illumination microscopy," J. Microsc. **198**, 82-87 (2000).

39 M. Gustafsson, D. Agard, and J. Sedat, "I5M: 3D widefield light microscopy with better than 100nm axial resolution," J. Microsc. **195**, 10-16 (1999).

40 M. G. Gustafsson, "Nonlinear structured-illumination microscopy: wide-field fluorescence imaging with theoretically unlimited resolution," Proc. Natl. Acad. Sci. U. S. A. **102**, 13081-13086 (2005).

41 F. Ferri, D. Magatti, A. Gatti, M. Bache, E. Brambilla, and L. A. Lugiato, "High-resolution ghost image and ghost diffraction experiments with thermal light," Phys. Rev. Lett. **94**, 183602 (2005).

42 O. Katz, Y. Bromberg, and Y. Silberberg, "Compressive ghost imaging," Appl. Phys. Lett. **95**, 131110 (2009).

43 T. Wilson, R. Juškaitis, M. Neil, and M. Kozubek, "Confocal microscopy by aperture correlation," Opt. Lett. **21**, 1879-1881 (1996).

44 S.-H. Jiang, and J. G. Walker, "Speckle-illuminated fluorescence confocal microscopy, using a digital micro-mirror device," Measurement Science and Technology **20**, 065501 (2009).

45 C. Ventalon, and J. Mertz, "Quasi-confocal fluorescence sectioning with dynamic speckle illumination," Opt. Lett. **30**, 3350-3352 (2005).

46 C. Ventalon, and J. Mertz, "Dynamic speckle illumination microscopy with translated versus randomized speckle patterns," Opt. Express **14**, 7198-7209 (2006).

47 J. H. Shapiro, "Computational ghost imaging," Phys. Rev. A **78**, 061802 (2008).

48 P. Ye, J. L. Paredes, G. R. Arce, Y. Wu, C. Chen, and D. W. Prather, "Compressive confocal microscopy," in *Acoustics, Speech and Signal Processing, 2009. ICASSP 2009. IEEE International Conference on*(IEEE2009), pp. 429-432.

49 V. Studer, J. Bobin, M. Chahid, H. S. Mousavi, E. Candes, and M. Dahan, "Compressive fluorescence microscopy for biological and hyperspectral imaging," PNAS **109**, E1679-E1687 (2012).

50 W.-K. Yu, M.-F. Li, X.-R. Yao, X.-F. Liu, L.-A. Wu, and G.-J. Zhai, "Adaptive compressive ghost imaging based on wavelet trees and sparse representation," Opt. Express **22**, 7133-7144 (2014).

51 N. Radwell, K. J. Mitchell, G. M. Gibson, M. P. Edgar, R. Bowman, and M. J. Padgett, "Single-pixel infrared and visible microscope," Optica **1**, 285-289 (2014).

52 B. I. Erkmen, and J. H. Shapiro, "Signal-to-noise ratio of Gaussian-state ghost imaging," Phys. Rev. A **79**, 023833 (2009).

53 M. N. O'Sullivan, K. W. C. Chan, and R. W. Boyd, "Comparison of the signal-to-noise characteristics of quantum versus thermal ghost imaging," Phys. Rev. A **82**, 053803 (2010).

54 N. D. Hardy, and J. H. Shapiro, "Ghost imaging in reflection: resolution, contrast, and signal-to-noise ratio," in *SPIE Optical Engineering+ Applications*(International Society for Optics and Photonics2010), pp. 78150L-78150L-78113.

55 B. I. Erkmen, "Computational ghost imaging for remote sensing," JOSA A **29**, 782-789 (2012).

56 D. Takhar, J. N. Laska, M. B. Wakin, M. F. Duarte, D. Baron, S. Sarvotham, K. F. Kelly, and R. G. Baraniuk, "A new compressive imaging camera architecture using optical-domain compression," in *Electronic Imaging 2006*(International Society for Optics and Photonics2006), pp. 606509-606509-606510.

57 Y. Li, A. C. Sankaranarayanan, L. Xu, R. Baraniuk, and K. F. Kelly, "Realization of hybrid compressive imaging strategies," JOSA A **31**, 1716-1720 (2014).

58 M. A. Herman, T. Weston, L. McMackin, Y. Li, J. Chen, and K. F. Kelly, "Recent results in single-pixel compressive imaging using selective measurement strategies," in *SPIE Sensing*

*Technology+ Applications*(International Society for Optics and Photonics2015), pp. 94840A-94840A-94818.

59 Y. Li, C. Hegde, A. C. Sankaranarayanan, R. Baraniuk, and K. F. Kelly, "Compressive image acquisition and classification via secant projections," Journal of Optics **17**, 065701 (2015).

60 B. J. Berne, and R. Pecora, *Dynamic light scattering: with applications to chemistry, biology, and physics* (Courier Corporation, 2000).

61 S. Sukhov, D. Haefner, and A. Dogariu, "Stochastic sensing of relative anisotropic polarizabilities," Phys. Rev. A **77**, 043820 (2008).

62 D. Haefner, S. Sukhov, and A. Dogariu, "Stochastic scattering polarimetry," Phys. Rev. Lett. **100**, 043901 (2008).

63 H. Bayley, and P. S. Cremer, "Stochastic sensors inspired by biology," Nature **413**, 226-230 (2001).

64 L. Gammaitoni, P. Hänggi, P. Jung, and F. Marchesoni, "Stochastic resonance," Rev. Mod. Phys. **70**, 223 (1998).

65 E. Wolf, "Coherence effects in scattering," in *Introduction to the Theory of Coherence and Polarization of Light*(Cambridge University Press, 2007).

66 J. H. Shapiro, and R. W. Boyd, "The physics of ghost imaging," Quantum Information Processing **11**, 949-993 (2012).

67 J. M. Mendel, "Tutorial on higher-order statistics (spectra) in signal processing and system theory: Theoretical results and some applications," Proc. IEEE **79**, 278-305 (1991).

68 D. H. Lenschow, V. Wulfmeyer, and C. Senff, "Measuring second-through fourth-order moments in noisy data," Journal of Atmospheric and Oceanic Technology **17**, 1330-1347 (2000).

69 A. Behrendt, V. Wulfmeyer, E. Hammann, S. Muppa, and S. Pal, "Profiles of second-to fourth-order moments of turbulent temperature fluctuations in the convective boundary layer: first measurements with rotational Raman lidar," Atmospheric Chemistry and Physics **15**, 5485-5500 (2015).

70 W. Padgett, and C. P. Tsokos, "Existence of a solution of a stochastic integral equation in turbulence theory," Journal of Mathematical Physics **12**, 210-212 (1971).

71 K. Balachandran, K. Sumathy, and H. Kuo, "Existence of solutions of general nonlinear stochastic Volterra Fredholm integral equations," Stochastic Analysis and Applications **23**, 827-851 (2005).

72 A. Dogariu, and E. Wolf, "Spectral changes produced by static scattering on a system of particles," Opt. Lett. **23**, 1340-1342 (1998).

73 E. Jakeman, and P. Pusey, "Significance of K distributions in scattering experiments," Phys. Rev. Lett. **40**, 546 (1978).

74 R. Barakat, "Direct derivation of intensity and phase statistics of speckle produced by a weak scatterer from the random sinusoid model," JOSA **71**, 86-90 (1981).

75 E. Jakeman, and R. Tough, "Non-Gaussian models for the statistics of scattered waves," Adv. Phys. **37**, 471-529 (1988).

76 K. Kanazawa, T. Sagawa, and H. Hayakawa, "Stochastic energetics for non-Gaussian processes," Phys. Rev. Lett. **108**, 210601 (2012).

77 N. Brenner, and Y. Shokef, "Nonequilibrium statistical mechanics of dividing cell populations," Phys. Rev. Lett. **99**, 138102 (2007).

78 M. Parrinello, and A. Rahman, "Crystal structure and pair potentials: A molecular-dynamics study," Phys. Rev. Lett. **45**, 1196 (1980).

79 A. S. Keys, A. R. Abate, S. C. Glotzer, and D. J. Durian, "Measurement of growing dynamical length scales and prediction of the jamming transition in a granular material," Nature physics **3**, 260-264 (2007).

80 D. H. Lenschow, and B. B. Stankov, "Length scales in the convective boundary layer," Journal of the Atmospheric Sciences **43**, 1198-1209 (1986).

81 C. Tong, J. C. Wyngaard, S. Khanna, and J. G. Brasseur, "Resolvable-and subgrid-scale measurement in the atmospheric surface layer: Technique and issues," Journal of the atmospheric sciences **55**, 3114-3126 (1998).

82 S. Alexander, G. E. Koehl, M. Hirschberg, E. K. Geissler, and P. Friedl, "Dynamic imaging of cancer growth and invasion: a modified skin-fold chamber model," Histochem. Cell Biol. **130**, 1147-1154 (2008).

83 J. Shi, and J. Malik, "Normalized cuts and image segmentation," IEEE Transactions on pattern analysis and machine intelligence **22**, 888-905 (2000).

84 M. Król, K. M. Pawłowski, K. Szyszko, H. Maciejewski, I. Dolka, E. Manuali, M. Jank, and T. Motyl, "The gene expression profiles of canine mammary cancer cells grown with carcinoma-associated fibroblasts (CAFs) as a co-culture in vitro," BMC Vet. Res. **8**, 35 (2012).

85 D. Shahnazian, F. Mokhtari, and G.-A. Hossein-Zadeh, "A method based on the granger causality and graph kernels for discriminating resting state from attentional task," in *Biomedical Engineering (ICoBE), 2012 International Conference on*(IEEE2012), pp. 83-88.

86 F. Mokhtari, and G.-A. Hossein-Zadeh, "Decoding brain states using backward edge elimination and graph kernels in fMRI connectivity networks," J. Neurosci. Methods **212**, 259-268 (2013).

87 F. Mokhtari, S. K. Bakhtiari, G.-A. Hossein-Zadeh, and H. Soltanian-Zadeh, "Discriminating between brain rest and attention states using fMRI connectivity graphs and subtree SVM," in *Medical Imaging: Image Processing*(2012), p. 83144C.

88 E. Baleine, and A. Dogariu, "Variable coherence tomography," Opt. Lett. **29**, 1233-1235 (2004).

89 P. A. Negulescu, T. B. Krasieva, A. Khan, H. H. Kerschbaum, and M. D. Cahalan, "Polarity of T cell shape, motility, and sensitivity to antigen," Immunity **4**, 421-430 (1996).

90 D. J. Stephens, and V. J. Allan, "Light microscopy techniques for live cell imaging," Science **300**, 82-86 (2003).

91 H. Zhang, and K.-K. Liu, "Optical tweezers for single cells," Journal of The Royal Society Interface **5**, 671-690 (2008).

92 J. A. Levitt, D. R. Matthews, S. M. Ameer-Beg, and K. Suhling, "Fluorescence lifetime and polarization-resolved imaging in cell biology," Curr. Opin. Biotechnol. **20**, 28-36 (2009).

93 S. B. Powles, "Photoinhibition of photosynthesis induced by visible light," Annual Review of Plant Physiology **35**, 15-44 (1984).

94 M. R. Hamblin, and T. N. Demidova, "Mechanisms of low level light therapy," in *Biomedical Optics 2006*(International Society for Optics and Photonics2006), pp. 614001-614001-614012.

95 J. Zhang, D. Xing, and X. Gao, "Low-power laser irradiation activates Src tyrosine kinase through reactive oxygen species-mediated signaling pathway," J. Cell. Physiol. **217**, 518-528 (2008).

96 Y.-Y. Huang, A. C.-H. Chen, S. K. Sharma, Q. Wu, and M. R. Hamblin, "Comparison of cellular responses induced by low level light in different cell types," in *BiOS*(International Society for Optics and Photonics2010), pp. 75520A-75520A-75510.

97 S. Wäldchen, J. Lehmann, T. Klein, S. van de Linde, and M. Sauer, "Light-induced cell damage in live-cell super-resolution microscopy," Sci. Rep. **5**, 15348 (2015).

98 D. H. Sliney, and B. C. Armstrong, "Radiometric evaluation of surgical microscope lights for hazards analyses," Appl. Opt. **25**, 1882-1889 (1986).

99 P. J. Shaw, "Comparison of widefield/deconvolution and confocal microscopy for three-dimensional imaging," in *Handbook of biological confocal microscopy*(Springer, 2006), pp. 453-467.

100 K. O. Pomeroy, and M. L. Reed, "The effect of light on embryos and embryo culture," Journal of Reproductive Biotechnology and Fertility **3**, 46-54 (2012).

101 J. C. Daniel, "Cleavage of mammalian ova inhibited by visible light," Nature **201**, 316-317 (1964).

102 K. Korhonen, S. Sjövall, J. Viitanen, E. Ketoja, A. Makarevich, and J. Peippo, "Viability of bovine embryos following exposure to the green filtered or wider bandwidth light during in vitro embryo production," Hum. Reprod. **24**, 308-314 (2009).

103 A. Agarwal, and S. S. Allamaneni, "Oxidants and antioxidants in human fertility," (2004).

104 K. J. Solarczyk, M. Zarębski, and J. W. Dobrucki, "Inducing local DNA damage by visible light to study chromatin repair," DNA repair **11**, 996-1002 (2012).

105 E. W. Gerner, and M. J. Schneider, "Induced thermal resistance in HeLa cells," Nature **256**, 500-502 (1975).

106 J. S. Mumm, and R. Kopan, "Notch signaling: from the outside in," Dev. Biol. **228**, 151-165 (2000).

107 R. Farhadifar, J.-C. Röper, B. Aigouy, S. Eaton, and F. Jülicher, "The influence of cell mechanics, cell-cell interactions, and proliferation on epithelial packing," Curr. Biol. **17**, 2095-2104 (2007).

108 M. A. Bouzan, and A. Dogariu, "Sensing thorough obscurants-using fluctuations in stochastic coherent scattering," in *CLEO: Applications and Technology*(Optical Society of America2016), p. AM4K. 3.

109 M. I. Akhlaghi, and A. Dogariu, "Tracking hidden objects using stochastic probing," Optica **4**, 447-453 (2017).

110 J. Fleischer, "Imaging: Making sensing of incoherence," Nature Photonics **10**, 211-213 (2016).

111 D. L. Donoho, "Compressed sensing," IEEE Trans. Inf Theory **52**, 1289-1306 (2006).

112 M. F. Duarte, M. A. Davenport, D. Takbar, J. N. Laska, T. Sun, K. F. Kelly, and R. G. Baraniuk, "Single-pixel imaging via compressive sampling," IEEE signal processing magazine **25**, 83-91 (2008).

113 D. Mardani, A. F. Abouraddy, and G. K. Atia, "Efficient modal analysis using compressive optical interferometry," Opt. Express **23**, 28449-28458 (2015).

114 D. Mardani, G. Atia, and A. F. Abouraddy, "Compressive interferometry for optical modal analysis in arbitrary degrees of freedom," in *Information Theory and Applications Workshop (ITA), San Diego, CA*(2015).

115 F. Bunyak, K. Palaniappan, S. K. Nath, T. Baskin, and G. Dong, "Quantitative cell motility for in vitro wound healing using level set-based active contour tracking," in *Biomedical Imaging: Nano to Macro, 2006. 3rd IEEE International Symposium on*(IEEE2006), pp. 1040-1043.

116 Y.-H. Sun, B. Reid, J. H. Fontaine, L. A. Miller, D. M. Hyde, A. Mogilner, and M. Zhao, "Airway epithelial wounds in rhesus monkey generate ionic currents that guide cell migration to promote healing," J. Appl. Physiol. **111**, 1031-1041 (2011).

117 R. Lavi, A. Shainberg, H. Friedmann, V. Shneyvays, O. Rickover, M. Eichler, D. Kaplan, and R. Lubart, "Low energy visible light induces reactive oxygen species generation and stimulates an increase of intracellular calcium concentration in cardiac cells," J. Biol. Chem. **278**, 40917-40922 (2003).

118 R. G. Baraniuk, V. Cevher, M. F. Duarte, and C. Hegde, "Model-based compressive sensing," IEEE Trans. Inf Theory **56**, 1982-2001 (2010).

119 A. C. Sankaranarayanan, M. A. Herman, P. Turaga, and K. F. Kelly, "Enhanced Compressive Imaging Using Model-Based Acquisition: Smarter sampling by incorporating domain knowledge," IEEE Signal Processing Magazine **33**, 81-94 (2016).

120 I. Vellekoop, and A. Mosk, "Universal optimal transmission of light through disordered materials," Phys. Rev. Lett. **101**, 120601 (2008).

121 J. Bertolotti, E. G. van Putten, C. Blum, A. Lagendijk, W. L. Vos, and A. P. Mosk, "Non-invasive imaging through opaque scattering layers," Nature **491**, 232-234 (2012).

122 O. Katz, E. Small, and Y. Silberberg, "Looking around corners and through thin turbid layers in real time with scattered incoherent light," Nature Photonics **6**, 549-553 (2012).

123 E. Van Putten, D. Akbulut, J. Bertolotti, W. Vos, A. Lagendijk, and A. Mosk, "Scattering lens resolves sub-100 nm structures with visible light," Phys. Rev. Lett. **106**, 193905 (2011).

124 M. A. Bouzan, and A. Dogariu, "Tracking objects surrounded by scattering media," in *CLEO: Science and Innovations*(Optical Society of America2017), p. SF2M. 1.

125 I. Roy, T. Y. Ohulchanskyy, D. J. Bharali, H. E. Pudavar, R. A. Mistretta, N. Kaur, and P. N. Prasad, "Optical tracking of organically modified silica nanoparticles as DNA carriers: a nonviral, nanomedicine approach for gene delivery," Proc. Natl. Acad. Sci. U. S. A. **102**, 279-284 (2005).

126 S. T. Acton, and N. Ray, "Biomedical image analysis: tracking," Synthesis Lectures on Image, Video, and Multimedia Processing **2**, 1-152 (2006).

127 F. Daum, and R. Fitzgerald, "Decoupled Kalman filters for phased array radar tracking," IEEE Transactions on Automatic Control **28**, 269-283 (1983).

128 S. R. Cloude, and E. Pottier, "A review of target decomposition theorems in radar polarimetry," IEEE Transactions on Geoscience and Remote Sensing **34**, 498-518 (1996).

129 U. Wandinger, "Introduction to lidar," in *Lidar*(Springer, 2005), pp. 1-18.

130 A. Velten, T. Willwacher, O. Gupta, A. Veeraraghavan, M. G. Bawendi, and R. Raskar, "Recovering three-dimensional shape around a corner using ultrafast time-of-flight imaging," Nat. Commun. **3**, 745 (2012).

131 L. Gao, J. Liang, C. Li, and L. V. Wang, "Single-shot compressed ultrafast photography at one hundred billion frames per second," Nature **516**, 74-77 (2014).

132 M. Buttafava, J. Zeman, A. Tosi, K. Eliceiri, and A. Velten, "Non-line-of-sight imaging using a time-gated single photon avalanche diode," Opt. Express **23**, 20997-21011 (2015).

133 G. Gariepy, N. Krstajić, R. Henderson, C. Li, R. R. Thomson, G. S. Buller, B. Heshmat, R. Raskar, J. Leach, and D. Faccio, "Single-photon sensitive light-in-fight imaging," Nat. Commun. **6**, 6021 (2015).

134 G. Gariepy, F. Tonolini, R. Henderson, J. Leach, and D. Faccio, "Detection and tracking of moving objects hidden from view," Nat Photon **10**, 23-26 (2016).

135 O. Katz, P. Heidmann, M. Fink, and S. Gigan, "Non-invasive single-shot imaging through scattering layers and around corners via speckle correlations," Nature Photonics **8**, 784-790 (2014).

136 J. W. Goodman, "Statistical properties of laser speckle patterns," in *Laser speckle and related phenomena*(Springer, 1975), pp. 9-75.

137 A. Ishimaru, *Wave propagation and scattering in random media* (Academic press New York, 1978).

138 A. T. Friberg, and R. J. Sudol, "The spatial coherence properties of Gaussian Schell-model beams," Journal of Modern Optics **30**, 1075-1097 (1983).

139 F. Gori, M. Santarsiero, and A. Sona, "The change of width for a partially coherent beam on paraxial propagation," Opt. Commun. **82**, 197-203 (1991).

140 J. W. Goodman, *Statistical optics* (John Wiley & Sons, 2015).

141 E. Baleine, and A. Dogariu, "Variable coherence scattering microscopy," Phys. Rev. Lett. **95**, 193904 (2005).

142 T. W. Kohlgraf-Owens, and A. Dogariu, "Transmission matrices of random media: means for spectral polarimetric measurements," Opt. Lett. **35**, 2236-2238 (2010).

143 S. Feng, C. Kane, P. A. Lee, and A. D. Stone, "Correlations and fluctuations of coherent wave transmission through disordered media," Phys. Rev. Lett. **61**, 834 (1988).

144 I. Freund, M. Rosenbluh, and S. Feng, "Memory effects in propagation of optical waves through disordered media," Phys. Rev. Lett. **61**, 2328 (1988).

145 R. Berkovits, M. Kaveh, and S. Feng, "Memory effect of waves in disordered systems: a real-space approach," Physical Review B **40**, 737 (1989).

146 P. Comon, C. Jutten, and J. Herault, "Blind separation of sources, Part II: Problems statement," Signal processing **24**, 11-20 (1991).

147 C. Jutten, and J. Herault, "Blind separation of sources, part I: An adaptive algorithm based on neuromimetic architecture," Signal processing **24**, 1-10 (1991).

148 M. Harris, G. Pearson, J. Vaughan, D. Letalick, and C. Karlsson, "The role of laser coherence length in continuous-wave coherent laser radar," journal of modern optics **45**, 1567-1581 (1998).

149 M. I. Akhlaghi, and A. Dogariu, "Single-shot coherent noise suppression by spatial interferometric heterodyning," Opt. Lett. **42**, 2378-2381 (2017).

150 M. A. Bouzan, and A. Dogariu, "Coherent Noise Suppression using Interferometric Cross-Correlation," in *Computational Optical Sensing and Imaging*(Optical Society of America2017), p. CTu1B. 3.

151 M. A. Bouzan, and A. Dogariu, "Coherent Noise Reduction Using Heterodyne Detection," in *CLEO: Science and Innovations*(Optical Society of America2017), p. SF2M. 3.

152 J. W. Goodman, "Some fundamental properties of speckle," JOSA **66**, 1145-1150 (1976).

153 J. Miao, D. Sayre, and H. Chapman, "Phase retrieval from the magnitude of the Fourier transforms of nonperiodic objects," JOSA A **15**, 1662-1669 (1998).

154 M. A. Vorontsov, and V. Kolosov, "Target-in-the-loop beam control: basic considerations for analysis and wave-front sensing," JOSA A **22**, 126-141 (2005).

155 S. An, A. Lapchuk, V. Yurlov, J. Song, H. Park, J. Jang, W. Shin, S. Karpoltsev, and S. K. Yun, "Speckle suppression in laser display using several partially coherent beams," Opt. Express **17**, 92-103 (2009).

156 H. Wang, and A. M. Rollins, "Speckle reduction in optical coherence tomography using angular compounding by B-scan Doppler-shift encoding," Journal of biomedical optics **14**, 030512-030512-030513 (2009).

157 H. Cao, Y. Zhao, S. Ho, E. Seelig, Q. H. Wang, and R. P. Chang, "Random laser action in semiconductor powder," Phys. Rev. Lett. **82**, 2278 (1999).

158 B. Redding, M. A. Choma, and H. Cao, "Speckle-free laser imaging using random laser illumination," Nature photonics **6**, 355-359 (2012).

159 A. Dogariu, and E. Wolf, "Coherence theory of pairs of correlated wave fields," Journal of Modern Optics **50**, 1791-1796 (2003).

160 I. Berezhnyy, and A. Dogariu, "Polarimetric description of superposing random electromagnetic fields with different spectral composition," JOSA A **21**, 218-222 (2004).

161 J. A. Richards, and J. Richards, *Remote sensing digital image analysis* (Springer, 1999).

162 K. Z. Abd-Elmoniem, A.-B. Youssef, and Y. M. Kadah, "Real-time speckle reduction and coherence enhancement in ultrasound imaging via nonlinear anisotropic diffusion," IEEE Trans. Biomed. Eng. **49**, 997-1014 (2002).

163 C. Li, W. Yin, and Y. Zhang, "User's guide for TVAL3: TV minimization by augmented lagrangian and alternating direction algorithms," CAAM report **20**, 46-47 (2009).

164 V. Blondel, S. P. Boyd, and H. Kimura, *Recent advances in learning and control* (Springer, 2008).

165 M. Grant, and S. Boyd, "CVX: Matlab software for disciplined convex programming, version 2.1., March 2014," URL http://cvxr.com/cvx (2011).

166 T. D. Visser, D. G. Fischer, and E. Wolf, "Scattering of light from quasi-homogeneous sources by quasi-homogeneous media," JOSA A **23**, 1631-1638 (2006).

167 W. H. Carter, and E. Wolf, "Scattering from quasi-homogeneous media," Opt. Commun. **67**, 85-90 (1988).